# Construction and testing of the scintillating fibre trackers for MICE

Aron Fish

Blackett Laboratory
Imperial College London

A thesis submitted for the degree of
Doctor of Philosophy
in the Department of Physics
at Imperial College London

September 2009

# Abstract

The discovery of neutrino mass through experimental evidence of neutrino oscillations at the end of the last century has provided the first proof that the Standard Model of particle physics is incomplete. To be able to extend the Standard Model to incorporate massive neutrinos first requires many theoretical uncertainties surrounding the particle and its interactions to be understood. Therefore, a dedicated experimental programme is needed over the coming decades to provide precision measurements of the neutrino oscillation parameters and also a possible measurement of CP violation in the lepton sector, which could have astrophysical consequences.

An intense source of neutrinos is required to achieve these precision measurements and the leading contender proposed to provide this neutrino beam, is the Neutrino Factory. Before a Neutrino Factory facility can be realised, a number of technological challenges need to be evaluated and understood first. One of which, is reduce the large phase space volume (emittance) of the initial muon beam, which is eventually stored and through decay provides the neutrino beam. Ionisation cooling is the chosen method to achieve this and the Muon Ionisation Cooling Experiment (MICE) at Rutherford Laboratory in the UK, is required to demonstrate ionisation cooling and its feasibility for a Neutrino Factory.

To demonstrate ionisation cooling, a section of a cooling channel will be constructed and single-particle measurements of emittance of a muon beam before and after the cooling channel from particle spectrometers will be compared. To measure emittance accurately requires precision measurements of the momenta and spatial coordinates at the spectrometers by tracking devices in a uniform magnetic field. The focus of this thesis is based around the construction and testing of the MICE tracker(s), including a study of its simulated performance and also construction and testing of a prototype.

# Acknowledgements

I would like to thank...

My supervisor Ken Long for all his help, advice and support throughtout.

A special thank you to my 2nd 'unofficial' supervisor Malcolm Ellis for his endless help, encouragement and support and putting up with all my computing/programming questions.

All members of the Imperial College HEP group involved in MICE, for all their help and advice.

Everyone from RAL, Fermilab and KEK who has helped and supported me while I was working at those Labs.

My Mum and Dad for all their endless support in everyway possible, this thesis is for you!

Finally all my friends and family, who know who they are, for keeping me sane away from all the work, I would have lost the plot without you.

# Contents

# List of Figures

# List of Tables

# Chapter 1

# Introduction

*The neutrino is "... the most tiny quantity of reality ever imagined by a human being"*

*Frederich Reines*

Neutrinos were first discovered over 50 years ago and are the most numerous matter particles in the Universe. Yet, due to their elusiveness there are still many unresolved issues in understanding them and the role they play in the universe and its creation. For a long time, neutrinos were thought to be massless particles and are considered to be this way in the current Standard Model of particle physics.

Recent experimental results have shown evidence of neutrino oscillations, indicating that in fact neutrinos have a non-zero mass. This result has opened up many new and exciting questions, which may have astrophysical consequences, such as the possibility that the properties of neutrinos may explain the matter anti-matter asymmetry in the Universe. For this reason, neutrino physics is at a very exciting stage and demands a detailed study of the particle and its interactions over the coming decades. Theoretical uncertainties regarding neutrinos need to be resolved and well understood, in order to be able to probe physics beyond the current Standard Model. This requires high precision, next generation neutrino experiments, one of the leading facilities proposed to achieve this, the Neutrino Factory, is seen as an essential component in the future neutrino physics programme.

This chapter will give a brief review of the history of the neutrino, the basics of neutrino oscillations and how they indicate non-zero mass, including some key neutrino experiments from the past, present and future, before eventually describing the role that the proposed Neutrino Factory can play in trying to understand this mysterious particle.

## 1.1 The Neutrino

The first suggestion of the neutrinos existence dates back to 1930. Up until this point in time, there had been confusion ever since the discovery in 1911 about the energy of emitted electrons in nuclear beta decay, as it seemed to follow a continuous spectrum, when other types of radioactivity involving gamma rays and alpha particles showed discrete energy spectra. This led physicists at the time, including Niels Bohr, to question the law of energy conservation. In December 1930, to save the law of energy conservation, a desperate remedy was postulated by Wolfgang Pauli to explain the apparent violation in nuclear beta decays by introducing a new, extremely light, neutral particle, which was emitted along with the electron, he named this particle "neutron". He did this in a now famous letter as he couldn't attend a physics meeting at the time [13]:

*Dear Radioactive Ladies and Gentlemen,*

*As the bearer of these lines, to whom I graciously ask you to listen, will explain to you more exactly, considering the "false" statistics of the N and 6Li nuclei, as well as the continuous beta spectrum, I have hit upon a desperate remedy to save the "exchange theorem" of statistics and the theorem of conservation of energy. Namely, the possibility that there could exist in the nuclei electrically neutral particles, that I wish to call neutrons, which have spin 1/2 and obey the exclusion principle and which further differ from light quanta in that they do not travel with the velocity of light. The mass of the neutrons should be of the same order of magnitude as the electron mass and in any event not larger than 0.01 proton masses. The continuous beta spectrum would then become understandable by the assumption that in beta decay a neutron is emitted in addition to the electron such that the sum of the energies of the neutron and the electron is constant...*

*I agree that my remedy could seem incredible because one should have seen those neutrons very earlier if they really exist. But only the one who dare can win and the difficult situation, due to the continuous structure of the beta spectrum, is lighted by a remark of my honored predecessor, Mr Debye, who told me recently in Bruxelles: "Oh, It's well better not to think to this at all, like new taxes". From now on, every solution to the issue must be discussed. Thus, dear radioactive people, look and judge. Unfortunately, I cannot appear in Tubingen personally since I am indispensable here in Zurich because of a ball on the night of 6/7 December. With my best regards to you, and also to Mr Back.*

*Your humble servant*

*W. Pauli*

Soon after this, James Chadwick discovered another neutral particle, which we know today as the neutron, which was too heavy to be the particle Pauli had proposed. However, in 1933 Enrico Fermi developed his theory of nuclear beta decay, better known as the weak force, which included Pauli's particle, but since the name "neutron" was now taken, Fermi called the particle "neutrino", which in italian means "little neutral one".

Since neutrinos interact very weakly with matter, Pauli questioned whether this particle may ever be detected. The neutrino remained undetected until 1956 when Clyde Cowan and Fredrich Reines first observed the existence of neutrinos from a nuclear reactor, through the detection of inverse beta decay ($\overline{\nu}_{\mathrm{e}} + \mathrm{p} \rightarrow \mathrm{n} + \mathrm{e}^{+}$) [14]. Further experiments during the 60's and 70's went on to suggest evidence for the three generations of neutrinos we know today; $\nu_{\mathrm{e}}, \nu_{\mu}$ and $\nu_{\tau}$. The LEP experiment at CERN confirmed that there are in fact three generations in 1989 [15] and all three have now been discovered experimentally.

## 1.2 Background

The study of Physics over time has shown that the laws of nature originate from symmetries, which in turn create the conserved quantities used to predict physical phenomena. The study of symmetries and how they are broken has been a cornerstone in understanding the properties of particles in nature and how they interact. This played a key role in the development of the Standard Model of particle physics in the 1960s, which describes mathematically the strong, weak and electromagnetic forces and the elementary particles that take part in these interactions.

The laws of nature were considered for a long time to be the same under mirror-reflection i.e. the reversal of spatial axes. This conservation law called 'Parity' was assumed to be a universal law, as it was respected by classical gravitation and electromagnetism. But, in the 1950s, Chen Ning Yang and Tsung-Dao Lee questioned the law of parity conservation in weak interactions, as it was untested [16]. So, Chien-Shiung Wu and collaborators in 1956 examined Yang and Lee's suggestion, by studying beta decay of Cobalt-60, where they discovered not only parity violation, but also that in weak interactions it was maximally violated [17].

Following this discovery, in 1958 Goldhaber, Grodzins and Sunyar [18] studied the "handedness"* of the neutrino. Through examining europium-152 undergoing inverse beta decay, they discovered that neutrinos were always left handed. This important result and the fact that right handed neutrinos have never been detected impled that neutrinos must be massless as special relativity suggests a massive particle would imply the existence of right handed neutrinos as well.

The discovery of parity violation required a new approach to the theory of weak interactions from Fermi's previous point-like, four fermion interaction. In 1958, the V-A (vector minus axial vector or left-handed) theory for weak interactions was proposed, by Richard Feynman and Murray Gell-Mann, which is now an integral part of the current Standard Model. In this new theory of the weak interaction, maximal violation of parity is described by the weak force only acting on left handed particles (and right handed anti-particles).

After the discovery of parity violation, a product symmetry, known as 'CP' was still considered to be conserved, in weak interactions as it is in the strong and electromagnetic interactions. CP symmetry, is conserved under transformation of a particle into its antiparticle. It is the combination of C (charge conjugation) symmetry, which reverses charge and P (parity) symmetry, which swaps left handedness with right handedness. But, in 1964 James Cronin and Val Fitch discovered CP violation in the decays of neutral kaons [19], even though this was the first clear evidence of CP violation, it had previously been proposed indirectly by Murray Gell-Mann and Abraham Pais in 1955 when they suggested oscillation based on mixing for neutral kaons.

If CP is conserved, quantum mechanics suggests that the weak eigenstates are identical to the mass eigenstates. But, evidence of CP violation showed that the interaction eigenstates are not the same as the mass eigenstates of quarks, but are instead a spanning set of eigenstates related through mixing. The CKM matrix in the Standard Model, is a unitary matrix with a mass dependency which describes the mismatch of quantum states of quarks when they propagate freely and take part in weak interactions. As the mixing is unitary, the baryon eigenstates are considered to be superpositions of the mass eigenstates and vice versa. The discovery of CP violation and oscillation theory in the baryon sector played a key role in the understanding of possible mixing in the lepton sector.

*Handedness is another way describing the spin direction of a particle along its direction of motion, for example, a right handed particle's spin points in the same direction as its momentum.

## 1.3 Neutrino Oscillations

In 1957, Bruno Pontecorvo questioned whether neutrinos were actually massless, as was thought at the time, by suggesting the possibility of neutrino oscillations [20]. His quantitative theory used to describe neutrino oscillations was developed over time to what we know today and is directly analogous to the quark mixing observed in the neutral kaon system.

In the weak interaction process, neutrinos are created or annihilated as flavour eigenstates $(\nu_e, \nu_\mu, \nu_\tau)^\dagger$. The flavour eigenstates propagate through space as a superposition of the mass eigenstates $(\nu_1, \nu_2, \nu_3)$. This is due to the different masses propagating with different frequencies, which in turn develops different phases and therefore a change in neutrino flavour with distance travelled.

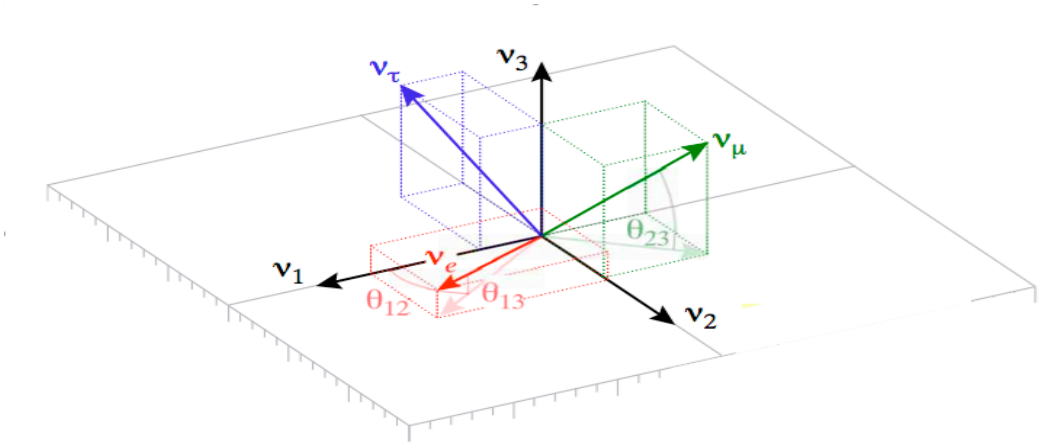


**Figure 1.1:** 3-dimensional rotation, induced by oscillation, of flavour eigenstates with respect to mass eigenstates. [1]

The relationship between the flavour eigenstates and mass eigenstates is visualised in figure 1.1 and given in quantum mechanical form in equation (1.1)

$$|\nu_\alpha\rangle = \sum_i U^*_{\alpha i} |\nu_i\rangle \tag{1.1}$$

where $\nu_\alpha$ is a neutrino with definite flavour $\alpha = \mathrm{e}, \mu, \tau$ and $\nu_\mathrm{i}$ is a neutrino with definite mass $\mathrm{i} = 1, 2, 3$ with $\mathrm{U}_{\alpha\mathrm{i}}$ representing the MNS matrix [21], which in the

$^\dagger$Here and throughout the chapter we consider the standard three neutrino theory, unless stated otherwise.

three neutrino theory case, is a unitary 3x3 mixing matrix and can be written in the form of (1.2):

$$U = \begin{pmatrix} c_{13}c_{12} & c_{13}s_{12} & s_{13}e^{-i\delta} \\ -c_{23}s_{12} - s_{13}s_{23}c_{12}e^{i\delta} & c_{23}c_{12} - s_{13}s_{23}s_{12}e^{i\delta} & c_{13}s_{23} \\ s_{23}s_{12} - s_{13}c_{23}c_{12}e^{i\delta} & -s_{23}c_{12} - s_{13}c_{23}s_{12}e^{i\delta} & c_{13}c_{23} \end{pmatrix} \tag{1.2}$$

where $\mathrm{c_{ij}} \equiv \cos\theta_{\mathrm{ij}}$ and $\mathrm{s_{ij}} \equiv \sin\theta_{\mathrm{ij}}$ and $\delta$ is a phase factor that is non-zero only if neutrino oscillation violates CP symmetry.

In vacuum, the mass eigenstates propagation can be described by plane wave solutions. From quantum mechanics, when applying Schrodinger's equation to $\nu_{\mathrm{i}}$, its evolution over time (t) can be described by [11]:

$$|\nu_i(t)\rangle = e^{-i(E_i t - p_i L)} |\nu_i(0)\rangle \tag{1.3}$$

where, assuming Lorentz invariance, $E_i$ and $p_i$ are the energy and momentum of $\nu_{\mathrm{i}}$ in the laboratory frame. Neutrinos are considered to be extremely relativistic such that, when using natural units, $c = 1$ and we say $\mathrm{t} \approx \mathrm{L}$, where L is the distance travelled. If we take $\nu_\alpha$ to be produced initially, with a definite momentum $p$, so all $\nu_{\mathrm{i}}$ components have this same momentum, we can say $\mathrm{E_i} = \sqrt{\mathrm{p}^2 + \mathrm{m_i^2}} \approx \mathrm{p} + \frac{\mathrm{m_i^2}}{2\mathrm{p}} \approx E + \frac{m_i^2}{2E}$, when E is the average energy of the $\nu_{\mathrm{i}}$ components of the neutrino and $\mathrm{p} \gg \mathrm{m_i}$. Subsituting this back into equation (1.1), we now have $\nu_\alpha$ as a superposition of mass eigenstates after propagating a distance L, so it can be written as:

$$|\nu_\alpha(L)\rangle \approx \sum_i U^*_{\alpha i} e^{-i(\frac{m_i^2}{2E})L} |\nu_i\rangle \tag{1.4}$$

then using the unitarity of U, we can invert equation (1.1) and say:

$$|\nu_i\rangle = \sum_\beta U_{\beta i} |\nu_\beta\rangle \tag{1.5}$$

where $\beta = \mathrm{e}, \mu, \tau$, now substituting $\nu_{\mathrm{i}}$ into the flavour eigenstate basis we find that:

$$|\nu_\alpha(L)\rangle \approx \sum_\beta \left( \sum_i U^*_{\alpha i} e^{-i(\frac{m_i^2}{2E})L} U_{\beta i} \right) |\nu_\beta\rangle \tag{1.6}$$

the original $\nu_\alpha$ after travelling a distance L, is now a combination of the weak flavour eigenstates, where the probability of $\nu_\alpha$ being observed with a flavour $\nu_\beta$ is:

$$P(\nu_\alpha \rightarrow \nu_\beta) = |\langle \nu_\beta | \nu_\alpha(L) \rangle|^2 \tag{1.7}$$

This probability, shown in equation (1.7), is correct for any number of generations of neutrinos. To simplify things, we will now consider the two flavour neutrino case which has a mixing matrix:

$$\mathrm{U} = \begin{pmatrix} cos\theta & sin\theta \\ -sin\theta & cos\theta \end{pmatrix}$$

From this we can then get the probability of flavour oscillation when $\alpha \neq \beta$ to be:

$$P(\nu_\alpha \rightarrow \nu_\beta) = sin^2 2\theta sin^2 \left( \frac{\Delta m^2_{ij} L}{4E} \right) \tag{1.8}$$

where $\Delta \mathrm{m}^2_{\mathrm{ij}} \equiv \mathrm{m}^2_{\mathrm{i}} - \mathrm{m}^2_{\mathrm{j}}$ is the mass squared difference and $\frac{\mathrm{L}}{\mathrm{E}}$ is an importnat ratio which dictates the oscillation pattern.

Therefore, in order to describe neutrino oscillations in the three neutrino case, it is clear that the oscillation parameters need to measured and understood, these parameters are:

- the three mixing angles: $\theta_{12}, \theta_{23}, \theta_{13}$
- the mass squared differences: $\Delta \mathrm{m}^2_{12}, \Delta \mathrm{m}^2_{23}$
- and the CP-violation phase: $\delta$

## 1.4 Evidence of Neutrino Oscillations

Many experiments have studied neutrinos over the years since their existence was proposed. These experiments have studied naturally occurring neutrinos, from the sun and the earth's atmosphere, as well neutrinos produced at nuclear reactors and neutrino beams from particle accelerators, which are produced from pion and muon decay. Various detector technologies have been used to study neutrinos and their

interactions. The detectors can't detect neutrinos directly, but instead indirectly through studying evidence of their weak interactions.

One of the first signs of possible neutrino oscillations came in the late 1960's when the Homestake experiment measured the neutrino flux coming from the sun [22]. Electron neutrinos ($\nu_e$) are continuously produced in the sun by the fusion process which is accurately described by the Standard Solar Model (SSM). The Homestake experiment only managed to detect around one third to one half of the number of the $\nu_e$ flux predicted by the widely accepted SSM. Even though this wasn't conclusive evidence of neutrino oscillations, the idea prevailed as one possible solution to the observed deficit of $\nu_e$ coming from the sun. This deficit came to be known as the 'Solar Neutrino Problem'.

Following this, in the 1980's large underground Cherenkov detectors such as Kamiokande, were designed to search for possible proton decay but instead found a deficit, in the ratio of muon neutrinos to electron neutrinos, for neutrinos produced by cosmic ray interactions in the earth's atmosphere. Again, neutrino oscillations were considered as a possible solution to this deficit, but statistics weren't considered good enough to consider it a discovery, this result became known as the 'Atmospheric Neutrino Deficit'.

The breakthrough finally came in 1998, when the Super-Kamiokande experiment announced evidence of neutrino oscillations and therefore that neutrinos have mass [23]. Through observing atmospheric neutrinos, Super-Kamiokande studied the angular distributions of muon neutrinos created in the earths atmosphere which meant they could determine from which direction they came. Since the earth is essentially transparent to neutrinos, Super-Kamiokande could observe neutrinos from all directions, including so called 'downward travelling neutrinos' from directly above ($\cos\theta = 1$) and 'upward travelling neutrinos' from the opposite side of the earth ($\cos\theta = -1$). When studying the neutrino flux as a function of zenith angle, they discovered a deficit in the upward travelling muon neutrinos but no decrease in electron neutrinos, when compared to the downward travelling neutrinos, as shown in figure 1.2. The explanation for this deficit, was determined to be due to muon neutrinos 'oscillating' into tau neutrinos, when travelling the extra distance and was considered the first conclusive evidence for neutrino oscillations.

Even though Super-Kamiokande could detect solar neutrinos and distinguish the difference between them and those from the atmosphere thanks to the significantly

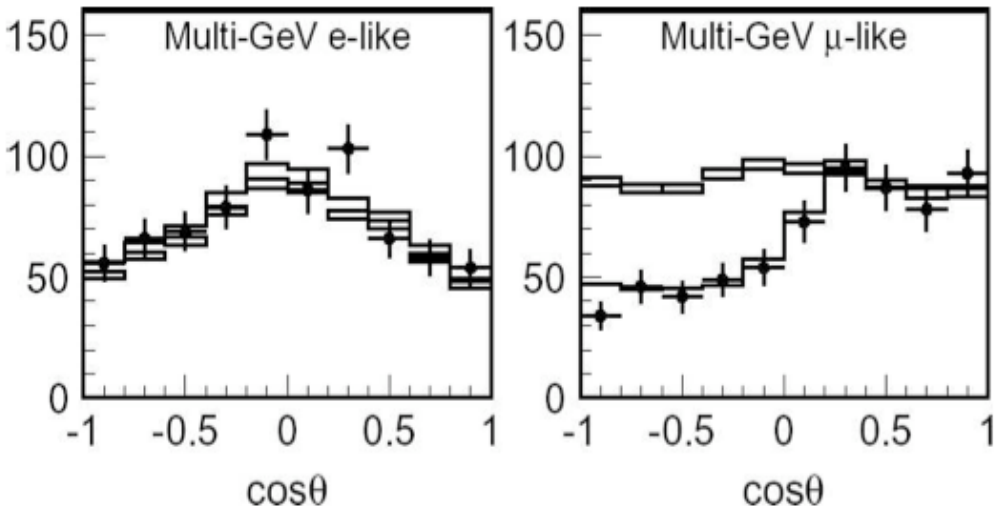


**Figure 1.2:** Super-Kamiokande zenith angle distributions. The points, boxed histograms and solid line correspond to data, MC with no oscillation and MC with best fit oscillation parameters, respectively. [2]

lower energy of solar neutrinos[‡] and by measuring the angular dependence, it couldn't differentiate between the different neutrino types with great precision at this lower energy.

Solar neutrinos, were observed with precision, at the Sudbury Neutrino Observatory (SNO), which again used a large underground Cherenkov detector but with a different interaction medium for detection. After combining the results from their solar neutrino data along with results from Super-Kamiokande, SNO produced the first direct evidence of oscillations [24] in 2001 and therefore further evidence for non-zero neutrino mass. SNO, was sensitive to all three neutrino flavours, allowing a determination of the number of muon and tau neutrinos observed at Super-Kamiokande. The SNO results also agreed with theoretical calculations from the SSM, about the number of neutrinos produced by the sun, therefore solving the previously mentioned 'Solar Neutrino Problem', by verifying the total neutrino flux for all three flavours.

The case for alternative explanations without neutrino oscillations, was finally excluded completely, following oscillation results from the KamLAND nuclear reactor experiment in 2002 [25], when considered along with the Super-Kamiokande and

[‡]Solar neutrinos tend to have an energy $< 20$ MeV and travel an astronomical unit whereas atmospheric neutrinos have an energy in the range of hundreds of MeV to GeV and a baseline of the radius of the earth

SNO results. Further confirmations and measurements have followed from various experiments including K2K [26] and MINOS [27].

## 1.5 Implications and Open Questions

Neutrino oscillations are now firmly established, implying that neutrinos are in fact massive. This important discovery means that for the first time since it was established in the late 1970's, the Standard Model of particle physics has been shown to be incomplete and needs to be extended. The implications of neutrino mass have generated more questions than they have answered and could have far reaching consequences, possibly leading to new physics, therefore many of the uncertainties involving neutrinos need to be understood.

The present limits on the absolute neutrino mass scale [28], show the mass of the neutrino to be much smaller then other fermions, which at present isn't completely understood, while at the same time current observations show the mixing angles of neutrinos to be very different from those of the quarks.

The contradictions between left handedness and mass also needs to be understood. In the context of the current Standard Model, the mechanism for generating the mass of all particles happens via the Higgs mechanism which requires both left and right handed particles to exist and at present only left handed neutrinos have been observed. Many extensions to the Standard Model, have been proposed to describe possible mechanisms generating massive neutrinos, including physics at high mass scales as seen in Grand Unified Theories (GUT), extra dimensions and supersymmetry. Therefore, a better understanding of neutrino oscillations through precision measurements of the mixing parameters in the MNS matrix could be an important step towards probing this new physics.

This exciting time for neutrino physics has led to many experiments currently trying to improve the measurements of these parameters as well as future experiments soon to begin or in the planning stages. The future neutrino experiments are focused on accelerator or nuclear reactor experiments, as opposed to solar or atmospheric experiments, as they can be controlled. Also, as neutrinos appear to oscillate over long distances, long baseline experiments are considered to be more beneficial.

Current observations haven't been able to pin down the mass differences and mixing angles of the MNS matrix, but they have narrowed down the range of possibilities for most, as shown [1]:

- $\theta_{12} = 33.9^\circ \pm 1.2^\circ$
- $\theta_{23} = 45^\circ \pm 8^\circ$
- $\theta_{13} < 13^\circ$
- $\Delta m^2_{12} = 7.7 \pm 0.2 \text{x} 10^{-5} \text{eV}^2$
- $\Delta m^2_{23} = 2.4 \pm 0.3 \text{x} 10^{-3} \text{eV}^2$

The so called solar parameters $\Delta m^2_{\text{sol}} \equiv \Delta m^2_{21}$ and $\theta_{\text{sol}} \equiv \theta_{12}$ have been measured by solar experiments such as SNO, in combination with nuclear reactor experiments such as KamLAND and CHOOZ [29]. Atmospheric neutrino experiments such as Super-Kamiokande along with accelerator experiments such as K2K, the first terrestrial long baseline experiment have determined current measurements for the so called atmospheric parameters $\Delta m^2_{\text{atm}} \equiv \mid \Delta m^2_{32} \mid$ or $\mid \Delta m^2_{31} \mid$ and $\theta_{\text{atm}} \equiv \theta_{23}$.

Current and near future experiments plan to improve the precision of some of these parameters to varying degrees, such as refining the measurement of $\theta_{23}$ (MINOS) and trying to measure $\theta_{13}$ (T2K). However, none of these and other planned experiments will be able to reach the sensitivity required for a full understanding of neutrino oscillations. In particular, these key questions will remain unanswered:

- the sign of $\Delta m^2_{\text{atm}}$ will be unknown (see figure 1.3);
- the mixing angle $\theta_{13}$ might still be measured with little precision or not at all; and
- the CP-violation phase $\delta$, will be unmeasured.

Even though neutrino oscillations cannot determine neutrino mass directly, if the sign of $\Delta m^2_{\text{atm}}$ and therefore the mass hierarchy can be determined, as shown in figure 1.3, this would be an important step, as it would mean that once a single neutrino mass measurement is made, a complete picture would exist. This would have cosmological implications, as an independent check of the contribution of neutrinos on dark matter in the universe would be possible.

Also, if the small mixing angle $\theta_{13}$, can be measured and shown to be greater then zero, this would indicate CP violation within the lepton sector and therefore require

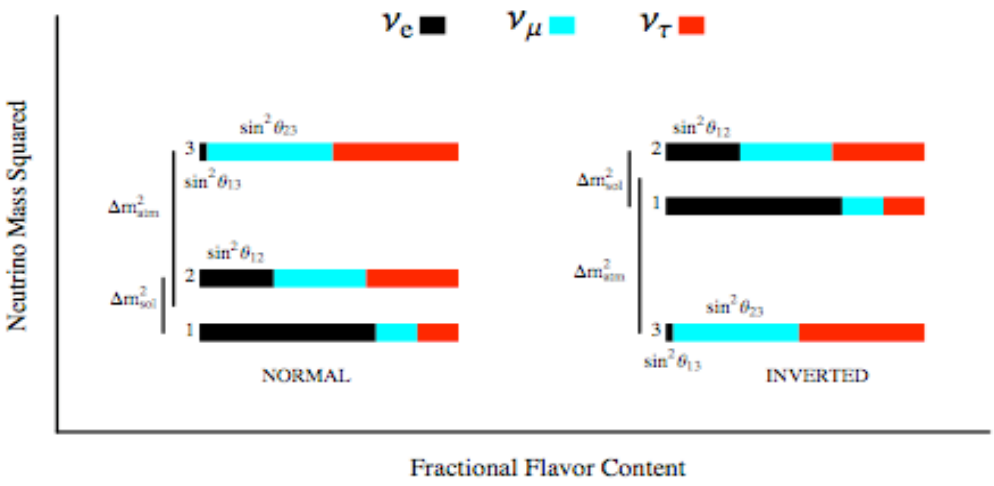


**Figure 1.3:** The possible (normal and inverted) mass hierarchies. Also, showing the approximate fractional flavour content of each of the mass eigenstates. [3]

a measurement of the CP violation phase, $\delta$. This would be a very important result and could possibly lead to an explanation of the observed matter-antimatter asymmetry in the universe.

Therefore, the advancement of the study of neutrino oscillations is regarded as not only interesting in its own right for neutrino physics but may also have important consequences leading to new physics.

## 1.6 Future of Neutrino Physics

To answer some of the previous questions described and provide the precision measurements of the neutrino oscillations that are required for a better understanding of neutrinos, three major next generation facilities have been proposed. A superbeam, beta beam and a Neutrino Factory. Existing studies, have shown that over much of the parameter space, the Neutrino Factory offers the best performance [30].

The sensitivity of the Neutrino Factory to $\theta_{13}$ and the sign of $\Delta m^2_{13}$ has been shown to be at least an order of magnitude greater when compared to other proposed neutrino facilities. Also, for smaller values of $\theta_{13}$, a Neutrino Factory has a greater sensitivity to the CP-violation phase, $\delta$. Figure 1.4, shows the sensitivity reach of a Neutrino factory to these three measurements as function of the angle $sin^2 2\theta_{13}$ at various possible detector distances [4].

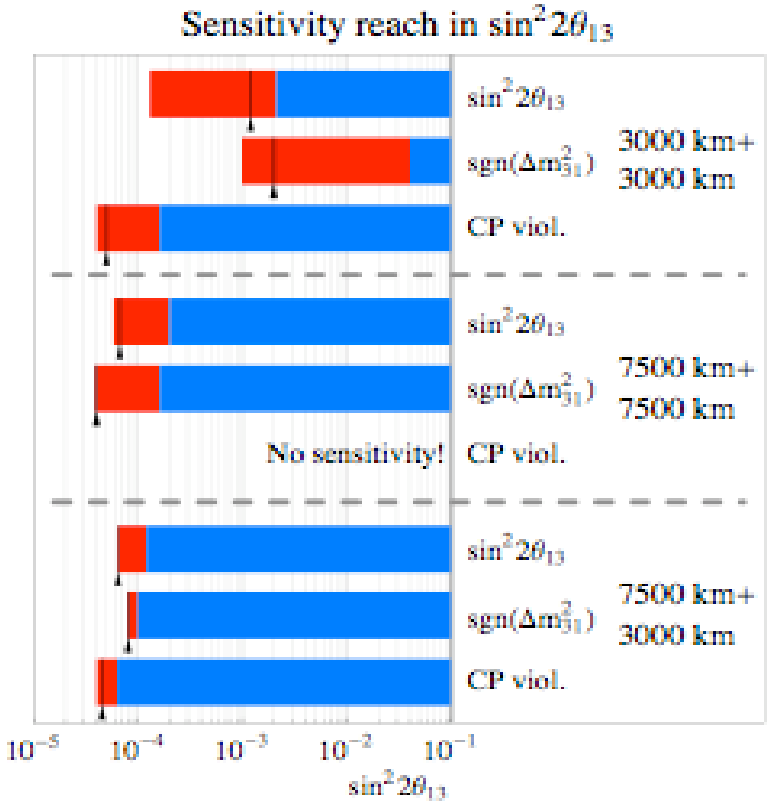


**Figure 1.4:** The Neutrino Factory sensitivity reaches as a function of $sin^2 2\theta_{13}$ for different baseline configurations. The bars show the ranges in $sin^2 2\theta_{13}$ where the sensitivity to the corresponding quantity can be achieved at the $3\sigma$ confidence level. The coloured bars mark the variations in the sensitivity within the $3\sigma$ range of the measured value of $\Delta m^2_{12}$. While, the arrows/lines correspond to the best fit values. [4]

As recently as 2007 an international scoping study (ISS) took place, examining the feasibility of these three facilities and also their possible physics reach in terms of current knowledge and also taking into consideration, where neutrino physics might be in a decade's time, when one of these next generation experiments could be realised.

The Neutrino Factory is considered to be the ultimate long baseline neutrino oscillation facility as it would provide many advantages over current and near-future neutrino facilities, by providing an intense, high energy and well characterised beam. Also, through the controlled decay of muons of both signs $\mu^+$ and $\mu^-$ a Neutrino Factory would be able to produce independent experiments using two different flavours, matter and antimatter.

A Neutrino Factory would send two high energy neutrino beams through the earth,

towards two detectors placed at different distances. The distance of the detectors and the beam energy plays an important role in the physics reach of measuring the oscillation parameters, as shown by the $\frac{L}{E}$ ratio described in section 1.3.

An international design study is currently in progress which will be considering the many technological challenges that building a facility, such as the Neutrino Factory would require, this is the focus of the following chapter.

# Chapter 2

# Neutrino Factory

## 2.1 Introduction

A Neutrino Factory is based on the idea of producing a beam of neutrinos via the use of muon storage rings. It was first proposed in 1997, around the time of the discovery of neutrino oscillations [31]. The concept suggested producing an intense neutrino beam with enough energy to probe a number of the unresolved issues within the field of neutrino physics. Since neutrinos are produced via decay and can not be accelerated themselves due to their neutral charge, a Neutrino Factory would basically add energy to the pre-decay system and also maximise the number of muons required to produce the neutrino flux to a sufficient level ($\sim 10^{21}$ neutrinos a year) to be able to study the unresolved fundamental questions discussed in the previous chapter - measurement of the mixing angle $\theta_{13}$, determining the mass hierarchy and searching for possible leptonic-CP violation.

Since the initial proposal, there have been independent conceptual designs presented in Europe [32], the US (US study I [33], US Study II [34] and US Study IIa [4]) and Japan [35]. The different designs have a lot of the same features, which will be discussed in the following sections. As recently as 2005, an International Scoping Study (ISS) was carried out, to review all the different designs as well as other next generation neutrino facilities proposed and put in place the initial foundations for a full International Design Study (IDS) [5] of a Neutrino Factory facility. The ISS was structured so that there were three main working groups; Accelerator design [7], Detectors [36] and Neutrino Physics [30]. The rest of this chapter will focus mainly on the accelerator issues, describing a baseline Neutrino Factory design.

## 2.2 General Design

The IDS Neutrino Factory design is shown in figure 2.1. The task of a Neutrino Factory is to generate an intense beam of neutrinos required for unprecedented precision measurements of the neutrino oscillation parameters and also a possible measurement of CP violation in the leptonic sector. To achieve this, a high powered proton source is required, these protons are then directed onto a target where pions are produced. These pions are then captured by a magnetic field at low energy and subsequently decay to muons. The phase space of the muons is controlled and shrunk through bunching and cooling, before being accelerated and injected into storage rings with long straight sections, where the muons decay producing neutrinos that are directed towards detectors. There are many technological challenges for each of the systems mentioned that need to be evaluated and overcome before a Neutrino Factory facility can be realised, these will now be discussed along with the current R&D programmes that are trying to understand and develop these techniques.

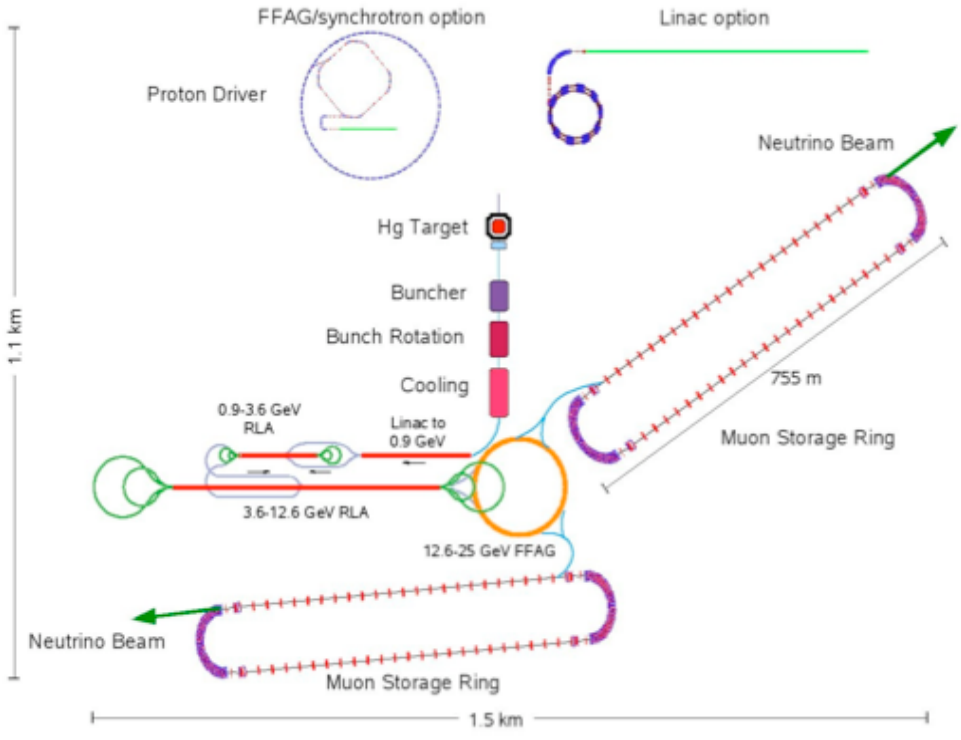


**Figure 2.1:** Schematic of IDS Neutrino Factory concept [5]

### 2.2.1 Proton Driver

The proton driver is the first part of the accelerator complex. The final design of the proton driver is still be to be decided, as there are many factors, which need to be considered, that influence the final choice of design. In addition to cost, the main factors to consider so that the required neutrino flux is achieved, include maximising the number of protons produced, while also understanding the structure and timing of the proton bunch. These factors also need to be considered in terms of their effect on the later parts of the accelerator systems, for example the pion and therefore muon yields are partly determined by the proton energy on the target material. The level of proton intensity that the target system can handle, without being destroyed, is another important consideration, as is the eventual effect that the proton bunch structure and timing will have on the capture and acceleration of the muons.

Through theoretical studies and trying to combine the differing and sometimes incompatible needs and requirements of the target, a baseline proton source with a beam power of up to 4MW has been proposed [7], comparing this to current proton sources of around 0.1MW and next generation sources of around 1MW, this will be a significant challenge. Proton beam energies ranging from 5 - 30 GeV have been considered and compared, along with various repetition rates and pulse structures. The prerequisite of pions and muons generated from the target having a small longitudinal emittance for acceleration, has led to the choice of delivering the proton bunches in 1-3 ns (rms) duration.

The different proton driver designs also vary depending on site location, as it is likely that it will be based around existing laboratory proton machines. Familiar features exist in the current proposed designs, which include all or some of the following: A high intensity $H^-$ linac, featuring a fast beam chopper, after this acceleration is performed in a number of steps using different combinations, depending on the design, of radio frequency quadrupoles (RFQs), rapid cycling synchrotrons (RCSs) and fixed field alternating gradient machines (FFAGs). A key R&D programme currently taking place is a proton driver front-end test stand at RAL [37].

### 2.2.2 Target and Capture

The target system is another key issue to be resolved for a Neutrino Factory, as mentioned already, its needs and requirements are heavily linked and sometimes

contradicting to those of the proton source. Therefore, the proton driver and target system need to be considered together, while also taking into consideration the latter sections of the complex. The main objective of the target is to create as many pions and subsequently muons as possible to be sent to the later parts of the accelerator facility.

There are many issues that need to be taken into consideration for this to be achieved. The beam energies, repetition rate and short bunch length coming from the proton driver has a massive effect as it leads to great stresses and strains on the target, therefore influencing the choice of target material. Through simulations, fixed targets have been ruled out as the intensity of the proton beam will destroy them within a few pulses, alternatives that have been proposed and studied have come in the form of moving solid targets (Carbon, Cooper and Tungsten) and moving liquid targets (Mercury). The requirement that the target operates in an environment, which is affected by strong radiation and magnetic fields from surrounding equipment also brings significant issues. The different targets perform differently depending on the energy and structure of the proton beam that the target is subjected to, taking all this into consideration the IDS has chosen liquid mercury as the baseline target material.

Many studies of different materials have or are currently taking place. One of the most notable studies is the MERIT experiment based at CERN [38]. The aim of the MERIT experiment is to examine the practicality and level of performance of a free moving liquid mercury target within a 15T magnetic field in a proof-of-principle experiment. The fact that the test is within a 15T solenoid is also significant as following the target the pions need to be captured and focused as they decay into muons. This will be achieved using a system of solenoids, where at the target centre a 20T solenoid field will be used and then tapered down adiabatically for the next 12m using a series of superconducting solenoids to around 1.75T. Even though liquid mercury has been chosen as the baseline, the option of moving solid targets is still being considered with R&D currently taking place at RAL [39].

### 2.2.3 Bunching and Phase Rotation

After the proton driver and target, which generates the incident pion beam, the following systems are needed to create, control and structure a muon beam that can be matched to the acceptance of the downstream accelerator systems. This set of

systems is called the "muon front end" of the accelerator complex [40]. Following the capture system previously mentioned, which uses solenoidal magnetic fields to capture the pions, there is a decay region of 100m in length where the pions will decay to muons.

Initially after the target the longitudinal phase space of the beam particles has a large energy spread and short time spread. This large energy spread needs to be reduced for acceptance into the downstream accelerators. This is achieved through a number of steps as shown by figure 2.2. The first step ("drift") allows an energy-time correlation to develop in the decay region following the capture channel, increasing the time spread of the beam. This correlation in longitudinal phase space is then used in a 50m buncher section, which uses RF cavities, of which frequencies increase adiabatically as they go downstream, to create 'micro-bunches'.

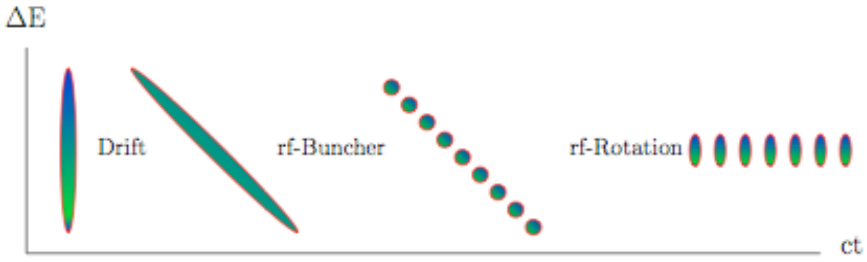


**Figure 2.2:** Change in longitudinal phase space through drift in the decay region, bunching and phase rotation [4]

Rotation of the longitudinal phase space of the beam is then used in order to reduce the energy spread with another set of RF cavities, in a 50m long phase rotation channel. To do this the RF frequency of the cavities is varied so that the macro-bunch, as shown in figure 2.2, can be manipulated in such a way that all the micro-bunches have the same energy as the centre of the macro-bunch. Therefore, muons that arrive early, will see an RF phase that reduces their energy and the late arriving muons see an RF phase that increases their energy, eventually producing micro bunches of the same energy. Simulation studies from the ISS can be seen in figure 2.3, showing the change in momentum after each section of the muon front end [4].

### 2.2.4 Cooling

As well as the longitudinal phase space issue of the initial muon beam which is controlled by bunching and phase rotation, the muon beam also has a transverse

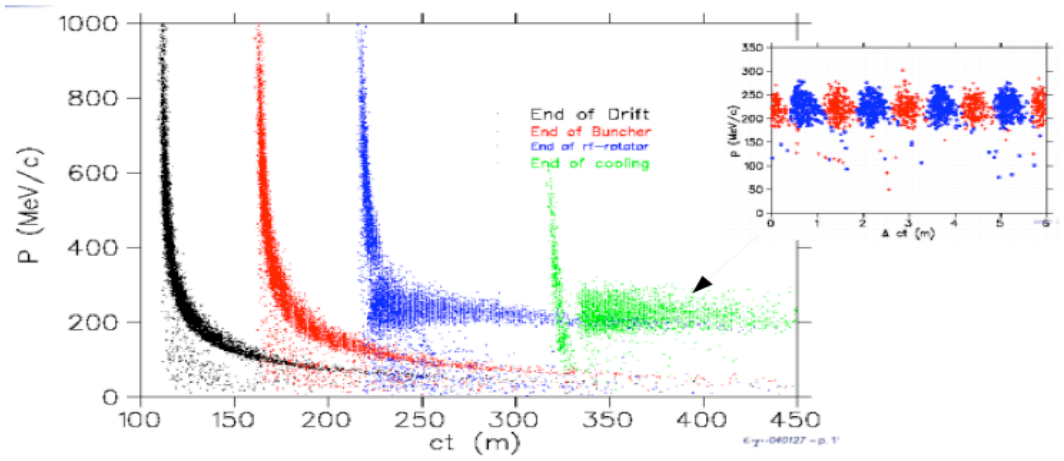


**Figure 2.3:** Simulation study of the 'muon front end'. Magnified plot shows eventual micro bunches of the same energy. The different colours indicate the change after each of the muon front end sections: Drift (black), Buncher (red), RF-rotation (blue) and cooling (green). [4]

phase space issue. The transverse emittance of the muon beam needs to be reduced to match the acceptance of the downstream accelerating stages of the Neutrino Factory.

The reduction in transverse phase space of the muon beam is achieved through a technique called ionisation cooling, which in short, involves passing the muons through a material where the particles lose both longitudinal and transverse momentum via ionisation energy loss ($\frac{dE}{dx}$) i.e.'cooling'.* After this, longitudinal momentum lost in the absorbers is restored through re-acceleration using RF cavities. The net effect is an overall reduction in transverse momentum spread, 'transverse cooling' as shown in figure 2.4.

Ionisation cooling is currently an untested technique, traditional cooling methods normally used in accelerators, such as stochastic, electron and laser cooling are not feasible for a muon beam, as they can take of the order a few seconds to minutes to produce effective cooling, which for muons with an average lifetime of 2.2$\mu$s (at rest) is too slow [34].

The different conceptual design studies by the US, Japan and Europe, have had differences in the design of the cooling section and in the case of the Japanese design, no cooling is envisaged at all, instead large apperture 'FFAGs' are used for muon acceleration meaning no reduction in the transverse emittance of the muon

*A counter effect that needs to be considered at this stage is 'heating' from multiple scattering.

beam is required. The European design suggests a cooling channel with RF cavities at a frequency of 88MHz, whereas the US studies propose RF cavities of 201MHz. Even though all designs are feasible, studies have shown that to produce the $\sim 10^{21}$ muon decays per year needed to reach the scientific aims of the facility [34], only the US design fulfils this requirement, therefore the ISS (and currently IDS) baseline is based on the US study IIa design [4], which uses lithium hydride absorbers with high gradient 201MHz RF cavities in an 80m solenoid channel.

The US study II design also meets the muon flux specification, with the only difference being the choice of absorber material. Liquid Hydrogen was the study II choice as it has been shown to be the best material for the absorbers in a cooling channel in terms of cooling performance. The choice of lithium hydride in study IIa and also for the baseline IDS Neutrino Factory design, has come from evidence that suggests that its cooling performance, even though not as efficient as liquid hydrogen, is sufficient enough for a Neutrino Factory, while at the same time being a cheaper option and also offering fewer handling and safety issues.

The IDS baseline cooling channel is predicted to reduce the transverse emittance of the muon beam from roughly 16 $\pi$ mm to about 7 $\pi$mm [7]. The theory of ionisation cooling with a description of emittance will be given in chapter 3 along with an overview of the Muon Ionisation Cooling Experiment (MICE). This experiment is an international R&D effort put together to study the feasibility of ionisation cooling and all the technical challenges that come with it [9].

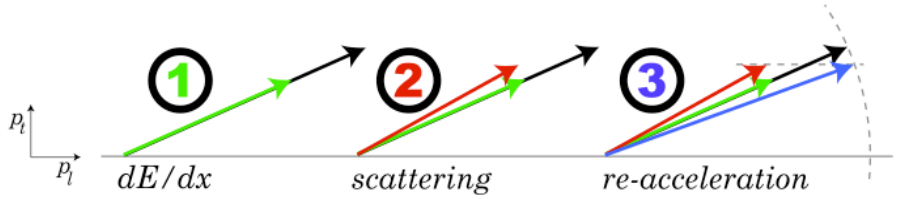


**Figure 2.4:** The principle of transverse ionisation cooling: Momentum is lost uniformly through energy loss when passing through a material (1), the counter effect of 'cooling' comes from multiple scattering i.e. 'heating' (2), finally re-acceleration restores longitudinal momentum resulting in net effect of transverse cooling. [6]

### 2.2.5 Acceleration

After the muons have exited the cooling section, which is considered the last part of the "muon front end" of a Neutrino Factory, the muons need to be accelerated

from a mean energy of ∼138MeV to somewhere in the range of 20-50GeV before injection into the storage rings for decay. The current baseline shown in figure 2.1, shows acceleration up to 25GeV. Due to the short average lifetime of muons conventional synchrotrons are not a viable option, as the ramping of the magnets needed to increase the bending magnetic fields isn't quick enough to contend with decay losses. Several alternatives have been investigated in terms of both cost and performance, with the aim of accelerating the muons as rapidly as possible, while keeping the growth in longitudinal and transverse emittance to a minimum.

The overall downstream acceleration system for a Neutrino Factory consists of various sub-systems. The choice of sub-systems comes from the beam dynamics at that point in the acceleration chain and also cost considerations. The baseline acceleration system from the ISS uses a combination of a pre-acceleration linac, recirculating linacs (RLAs) [41] and Fixed Field Alternating Gradient accelerators (FFAGs) [42].

The pre-accelerator linac, accelerates the beam from 138MeV to 0.9GeV. Once at energies of 0.9GeV, the RLAs are considered to be able to handle the spread in energy found at this point and accelerate the beam. RLAs are based on having one (dogbone design) or more (racetrack design) linacs with series of arcs used for bending the beam back into the original or next linac for further acceleration, as shown in figure 2.5.

The baseline design uses a dogbone RLA, as this reduces the number of RF cavities needed and therefore reduces the cost. Several arcs are used which have different field settings, this allows muons of different momenta going in and coming out of the arcs via the use of fixed field switchyards before re-acceleration. This is why the RLAs need to come after the original linac as the energy spread and initial beam size need to be much smaller relative to the beam energy to enable clean separation into the arcs. This non-zero energy spread, along with the increase in transverse beam size places a limit on the number of passes the beam can do through the RLAs. To compensate for this, two dogbone RLAs are proposed for the baseline to reach the required acceleration, with the smaller RLA accelerating the beam from 0.9 to 3.6GeV and the second RLA increasing this to 12.6GeV.

Following the RLAs the final sub-system foreseen is FFAG accelerators, which were originally proposed and developed successfully by the Japanese [43]. The FFAG utilises the use of one arc for all different beam energies avoiding the limitations of the RLA switchyard by using fixed field bending magnets. In the bending magnets,

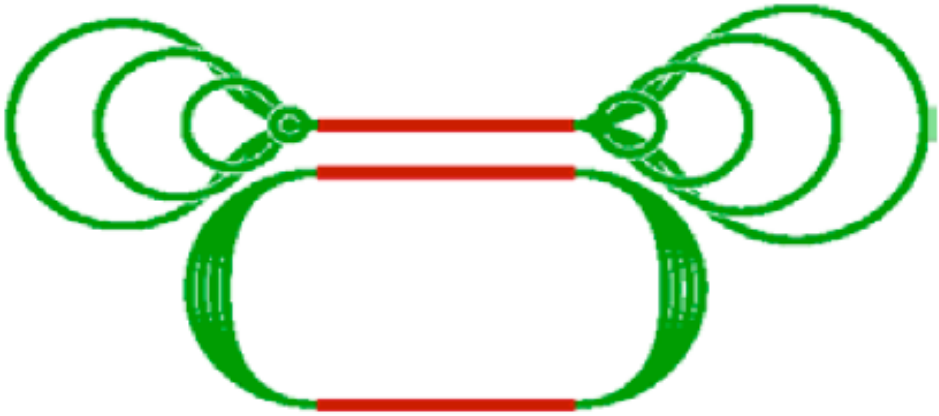

**Figure 2.5:** Geometries of 'dogbone' (top) and 'racetrack' (bottom) RLA designs, showing RF cavitiy sections (in red) [7]

the magnetic field is smaller at smaller radii, meaning particles with greater momentum are within a larger bending field and particles with less momentum are within a smaller bending field, allowing a range of momenta particles to be accelerated simultaneously, without the need to ramp the magnets.

There are two types of FFAG under consideration for a Neutrino Factory, scaling and non-scaling FFAGs. Originally scaling FFAGs were proposed by the Japanese, which scale the focussing field with radius. The scaling FFAGs require the use of expensive superconducting magnets, due to the large aperture requirement of the magnets. Also, their large time of flight variation with energy requires low frequency RF cavities to accelerate muons. Therefore, scaling FFAGs are only really feasible at lower energies and also only really required for the Japanese design, which doesn't include cooling, where a large acceptance is a necessity.

The ISS has decided to use non-scaling FFAGs in the baseline design, which don't scale the focussing field with radius. This means at higher energies they are predicted, through studies [7], to be able to address the problems mentioned with scaling FFAGs, as most of the bending takes place in the defocusing magnets, resulting in a smaller aperture and time of flight variation required. This in turn, allows for the use of higher frequency RF cavities matching those used in the baseline 'muon front end' permitting higher accelerating gradients.

In the design shown in figure 2.1 one non-scaling FFAG is expected to increase the energy from 12.6GeV to 25GeV, if necessary another FFAG can be added to

reach 50GeV. Non-scaling FFAGs may still cause problems as the smaller acceptance and variation in time of flight may cause emittance growth, especially if multiple FFAG stages are used. R&D efforts are currently studying the feasibility of FFAGs including the EMMA project at Daresbury Laboratory, UK [44], which is studying beam dynamics in a non-scaling FFAG using electrons.

### 2.2.6 Storage Ring

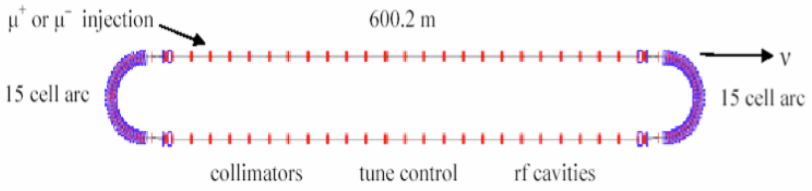


**Figure 2.6:** Schematic of ISS 'racetrack' storage ring [7]

The last stage of a Neutrino Factory is the muon storage ring. Here, the accelerated muons are captured and stored before decaying in long straight sections which are directed at detectors. The ISS 'racetrack' storage ring, as shown in figure 2.6, has two straight sections where muons will decay to produce neutrino beams, which on average will have the same direction as the muons with a small divergence. This divergence can be controlled through the use of soft focussing and large aperture magnets on the muon beam before decay. The neutrinos are sent to two detector sites, which at present are considered to be in the range of 3000-8000km. These detector distances, lead to a multi-inclined and multi-directional ring with geometrical issues that need to be well understood in consultation with the detector and phenomenological groups, so that the neutrino flux at the detectors is as high as possible. There are a few geometrical designs under consideration, these include the 'racetrack' design shown, as well as a 'triangular' and 'bow-tie' shaped ring for both sign muons. At present, the ISS prefers the racetrack design as shown in figure 2.6, but the possible detector sites from the accelerator location will play a key role in the eventual choice of storage ring design.

## 2.3 Neutrino Factory Detectors

The aim of the neutrino detectors, whether for a Neutrino Factory or another future neutrino facility, will be to measure all the parameters of the neutrino mixing matrix

with optimum sensitivity. This requires a long-baseline oscillation experiment, with detector distances of up to 7000km proposed as optimal by theoretical studies [36]. A near detector is also required to measure the flux and energy of the neutrino beam and its background, which needs to be well understood before oscillation effects take place and so the two can eventually be compared. The detector choice and distance is motivated not only by neutrino energy and flux coming from the accelerator complex, but also with the the aim of measuring the oscillation signals as accurately as possible, therefore all three need to be considered in parallel. The ISS has considered a number of options for the neutrino detectors based on current and future technologies. These are discussed in full in the detector ISS report [36].

## 2.4 Beyond a Neutrino Factory

A Neutrino Factory, is considered to be the ultimate tool for studying neutrino oscillations, including the possible discovery of CP violation in the lepton sector. It is also, an initial step towards the realisation of a future Muon Collider. A Muon Collider, is a proposed multi-TeV lepton collider, which could provide advantages (and also disadvantages) when compared to hadron colliders and electron-positron colliders. Hadron machines, such as the LHC at CERN can reach centre of mass energies within the TeV scale, but have the added issues of the size of the machine required to reach this energy scale and also the large amount of background produced such as hadronic jets. Lepton colliders on the other hand offer "clean" single particle interactions, which means the interaction energy is twice that of the machine energy, whereas for a hadron collider the effective energy is lower then that of a proton.

Next generation electron-positron colliders have been proposed following on from the successful LEP experiment at CERN, but these are limited to centre of mass energies below the TeV scale, this is due to the limiting effects synchrotron and beamstrahlung radiation would have on the cost and performance respectively. Muons, which have a much larger mass then electrons ($\frac{\mathrm{m}_\mu}{\mathrm{m}_\mathrm{e}} \approx 207$), offer the same advantages of single particle interactions, but with minimal bremstrahhlung, and can also offer comparable energies to hadron colliders, while being accelerated and stored in rings of much smaller radius. These advantages, along with others and also possible limitations of a muon collider facility are described further in [45], but it is clear, from the points made, that a muon collider is an attractive alternative that needs to be considered as a possible future particle physics facility.

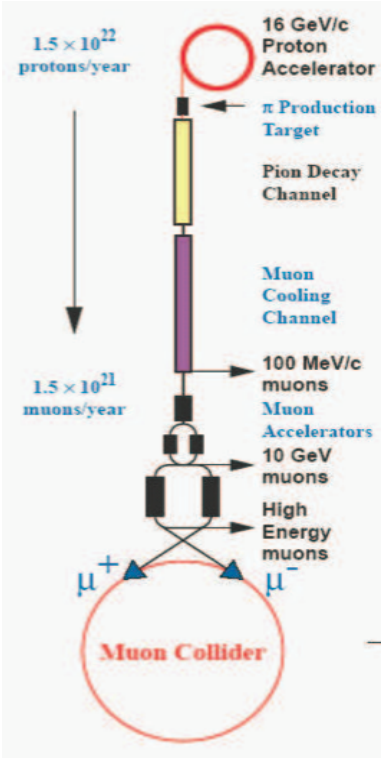


**Figure 2.7:** Schematic of muon collider design concept [8]

A Neutrino Factory and a Muon Collider have very strong connections [46], as the principles of the two are near identical up to the point of the muon storage ring as shown in figure 2.7. Therefore, much of the R&D towards a possible Neutrino Factory will be of massive use to a future Muon Collider. An essential part of this R&D, understanding the feasibility of ionisation cooling, is a necessity for a muon collider and also requires stronger cooling then that proposed for a Neutrino Factory. Therefore, an experimental demonstration of ionisation cooling is seen as an essential R&D effort for both facilities. MICE, is the main programme currently taking place to achieve this demonstration and this will now be discussed in detail in chapter 3.

# Chapter 3

# MICE

Following on from the discussion about the need for cooling for a proposed Neutrino Factory, an international collaboration was put together to study the feasibility of Ionisation Cooling. In this chapter an overview of the Muon Ionisation Cooling Experiment (MICE) will be presented.

## 3.1 Introduction

The principle of ionisation cooling is well understood theoretically, but at present has never been realised in practice. This is the motivation for MICE as essentially a proof-of-principle experiment and a key part of R&D required for a future Neutrino Factory and/or Muon Collider. The objectives of MICE, as set out in the MICE proposal [47], are not only to demonstrate muon ionisation cooling but also:

- To show that it is possible to design, engineer and build a section of cooling channel capable of giving the desired performance for a Neutrino Factory.
- To place it in a muon beam and to measure its performance in various modes of operation and beam conditions, thereby investigating the limits and practicality of cooling.

To achieve this MICE will be carried out at Rutherford Appleton Laboratory (RAL) in the UK, developing many untried techniques, and combining accelerator R&D

with some standard particle physics detection systems which have been adapted for specific MICE operation. The initial emittance of the muon beam for MICE will be varied from roughly 2 $\pi$ mm - 10 $\pi$ mm*. The MICE cooling channel (based on the US study II cooling channel [34]), when subjected to muons with momenta ranging from 140MeV/c to 240MeV/c is expected to result in a reduction of transverse beam emittance of $> 10\%$. This reduction in transverse emittance should be measured with an absolute precision of $\pm 0.1\%$.

## 3.2 Overview of MICE

The full layout of the baseline MICE design is shown in figure 3.1. MICE consists of a cooling channel located between a pair of particle spectrometers and placed in a 200MeV/c muon beam. The MICE muon beam originates from protons coming from the ISIS 800MeV/c proton synchrotron. These protons interact with a target developed specifically for MICE producing a secondary pion beam, which is then transported along a newly assembled pion-muon beamline into MICE. The experiment has been setup in such a way as to enable measurements of the emittance to be made on individual muons before and after the cooling channel.

Upstream of the cooling channel, the muon beam first interacts with a pair of time of flight counters (TOF0 and TOF1) and a Cherenkov detector (CKOV) whose purpose is to distinguish muons from proton and pion contamination. Following this a lead diffuser is used to produce the matched input emittance. The muons then pass through the upstream spectrometer, which consists of a scintillating fibre tracker within a magnetic field, individual muon tracks will be reconstructed providing (with TOF) the 6D phase space coordinates needed to determine the input emittance. After this, muons enter the cooling channel itself, which is composed of absorbers followed by RF cavities. The role of the absorbers is to reduce the muon's longitudinal and transverse momentum through ionisation energy loss, following this, the longitudinal momentum is replaced in the RF cavities. The third and final absorber (not included in the study II design) is added mainly to shield the downstream tracker from radiation produced by the RF cavities, as this could affect the systematic error measurement coming from the tracker.

*The initial emittance (pre-cooling) for the Neutrino Factory is expected to be $\sim 16\pi$mm [7], but these two initial emittances cannot be directly compared as the MICE cooling channel is shorter then that expected at a Neutrino Factory.

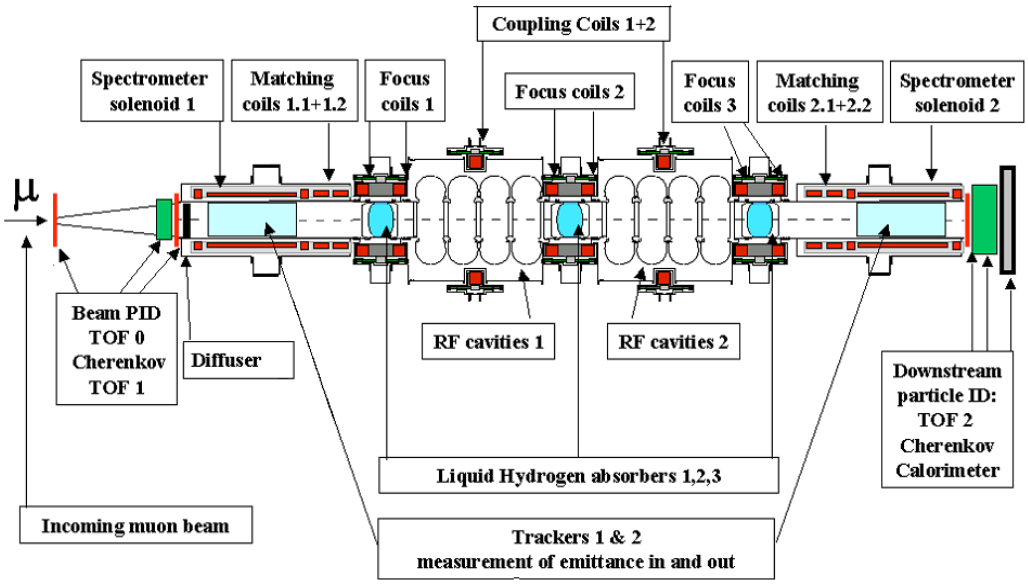


**Figure 3.1:** Schematic of full MICE setup [9]

The whole cooling channel is situated within a solenoidal magnetic field to provide the beam optics required. Once the muons have traversed the cooling channel the muons pass through a second spectrometer where measurements are made to determine the output emittance. Finally, after exiting the second spectrometer further particle identification is needed to reject beam contamination of pions and possible muon decays while traversing the channel, this will be achieved via a third time of flight counter (TOF2) and an electromagnetic calorimeter (EMCAL). All these components will be described individually in the following sections.

## 3.3 Beamline

The MICE muon beamline, shown in figure 3.2 is based upon well developed methods for a pion to muon decay channel, it is required to deliver a high purity, high

rate muon beam with the added specification for emittance tuning and matching into the experiment. The beam is produced by dipping a titanium target into the halo of the ISIS proton beam producing mainly pions but also protons and a few muons, which are then captured by a quadruple triplet. Following this, the particles are momentum selected by a rectangular dipole which bends the beam towards the MICE hall, before entering the 5m long, superconducting 5T decay solenoid where pions decay to muons. After the decay solenoid a second dipole magnet is used, which aims to produce a"clean" muon beam by accepting muons of a desired momentum, separating them from most of the undecayed pions and protons. Finally, the muon beam is sent to the MICE area via a large acceptance transport channel which consists of another two sets of quadruple triplets.

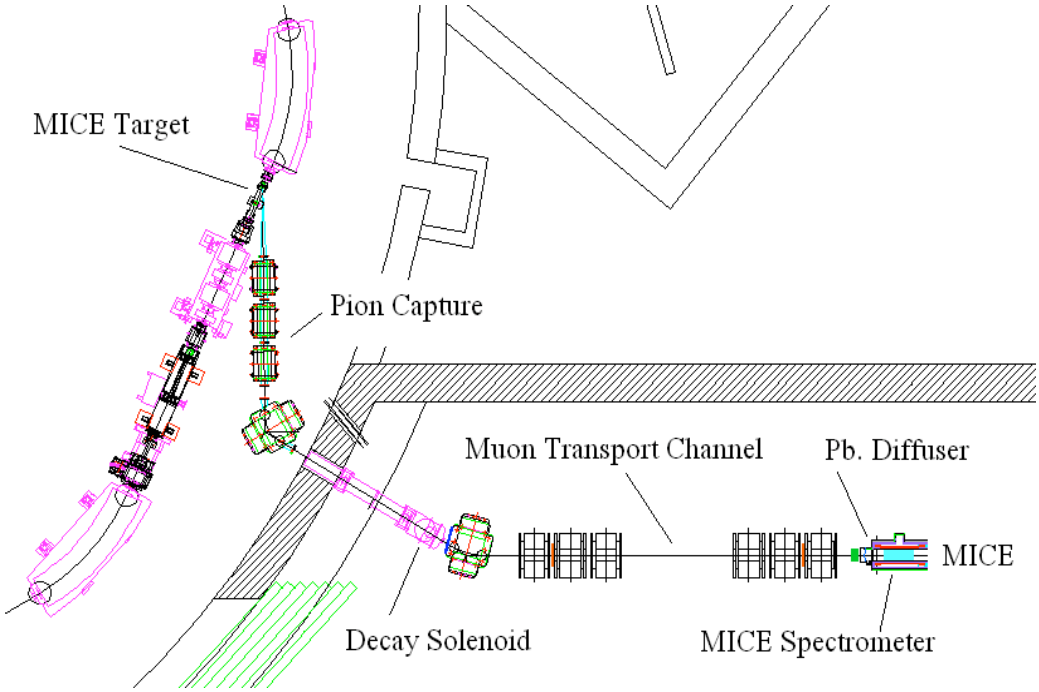


**Figure 3.2:** MICE Beamline layout from ISIS ring [9]

The cooling performance of MICE, will be studied as a function of beam momentum and beam emittance. The desired muon beam momentum is established via dipole settings within the transport beamline. The emittance of the muon beam also

needs to be determined, due to limitations in the beamline the incoming beam is smaller than the matched beam required, to solve this the emittance of the muon beam is increased and controlled by passing it through a lead diffuser to fill the matched emittance of the cooling channel. The lead diffuser thickness will be varied depending on the different configurations and setups to be used. It will be placed immediately before the upstream spectrometer which also gives it the added side effect of working as a radiation shield for TOF1 from RF induced background.

## 3.4 Emittance

In conventional particle beamlines it is desirable to minimise divergences in the beam, so to limit particle losses [48]. Particle trajectories and their deviations, when moving along a beam transport system such as a solenoidal channel are described in six-dimensional phase space and defined in terms of generalised transformations and Hamiltonian dynamics [49] [50].

In ionisation cooling, it is useful to extend this treatment of a particle trajectory to consider the entire bunch of particles through the solenoidal beamline. To do this, a conservation law of phase space in a particle beam known as Liouville's theorem is considered [51]. Liouvilles theorem states that the phase space volume of a particle beam is considered constant when only conservative forces[†] are applied. This phase space volume of a particle beam is defined as the emittance, $\varepsilon$.

The six-dimensional phase space variables of a particle beam can be expressed as $(\mathrm{x}, \mathrm{p_x}, \mathrm{y}, \mathrm{p_y}, \mathrm{t}, \mathrm{E})$, the transverse position coordinates x, y, the transverse momentum coordinates $p_x$, $p_y$ and the longitudinal coordinates energy, E and time, t. In accelerator physics literature, it is sometimes more common to use trace space variables instead $(\mathrm{x}, \mathrm{x}', \mathrm{y}, \mathrm{y}', \mathrm{t}, \mathrm{E})$, where $\mathrm{x}'$ and $\mathrm{y}'$ are the transverse divergences of the beam and are defined, for example in the x dimension, as $\mathrm{x}' = \mathrm{atan}(\frac{\mathrm{p_x}}{\mathrm{p_z}}) \simeq \frac{\mathrm{p_x}}{\mathrm{p_z}}$, where $\mathrm{p_z}$ is the longitudinal momentum and therefore, $\mathrm{x}'$ is considered to be small.

Liouvilles theorem is considered a very useful tool when considering the transformation of a particle beam along the beam direction z, even though the phase space beam can take on many forms, it is common, to describe the beam in phase/trace space using an ellipse. An example of a 2D $(\mathrm{x}, \mathrm{x}')$ trace space ellipse is shown in figure 3.3. It is described analytically by:

[†]i.e. in magnetic or general fields which are independent of velocity.

$$\gamma x^2 + 2\alpha x x' + \beta x'^2 = \varepsilon \tag{3.1}$$

this is the equation of the ellipse also known as the Courant and Synder invariant [10]. The area of the ellipse, A (also sometimes called the 'beam emittance') is Liouville invariant and given by:

$$A = \pi x x' = \pi \left(\varepsilon\beta\right)^{\frac{1}{2}} . \left(\frac{\varepsilon}{\beta}\right)^{\frac{1}{2}} = \pi\varepsilon \tag{3.2}$$

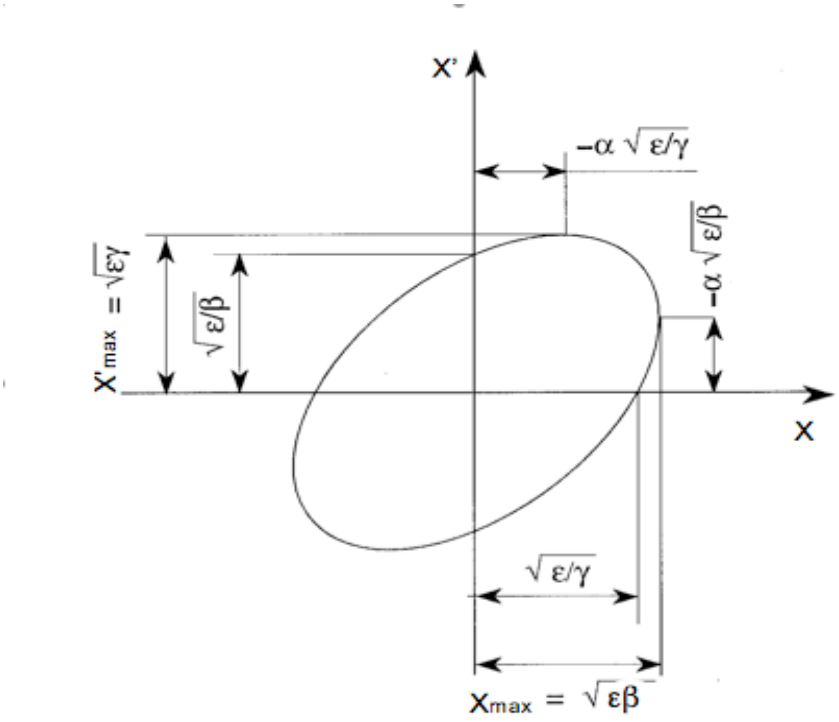


**Figure 3.3:** A phase space ellipse example with parameters [10].

From Liouvilles theroem it is understood that the particle density enclosed in the ellipse is conserved. Therefore, to describe the particle beam all that is needed is a description of how the ellipse parameters shown in figure 3.3, also known as the Twiss parameters (periodic functions) of the lattice, transform along the beamline. During this transformation the phase space ellipse will continually change its form and orientation but not its area, where the linearised transformation yields a matrix formulation of the ellipse parameters.

The equation for an ellipse can be written as:

$$u^T V^{-1} u = 1 \tag{3.3}$$

where u = $\left(\frac{\mathrm{x}}{\mathrm{x}'}\right)$ and V is a covariance matrix containing information of the moments of the beam parameters.

Applying equation (3.3) in 2D we get an ellipse equation of the form [51]:

$$\sigma_{22} x^2 + 2\sigma_{12} x x' + \sigma_{11} x'^2 = \varepsilon^2 \tag{3.4}$$

which when compared to the Courant Synder equation (3.1) for an ellipse and using the geometric interpretation of emittance conservation, we have a correlation between the ellipse parameters giving $\beta\gamma - \alpha^2 = 1$, we can then define the 'beam matrix' in 2D to be:

$$V_{2D} = \begin{bmatrix} \sigma_{11} & \sigma_{12} \\ \sigma_{21} & \sigma_{22} \end{bmatrix} = \begin{bmatrix} \sigma_{xx} & \sigma_{xx'} \\ \sigma_{xx'} & \sigma_{x'x'} \end{bmatrix} = \varepsilon \begin{bmatrix} \beta & -\alpha \\ -\alpha & \gamma \end{bmatrix} \tag{3.5}$$

The phase space area of the ellipse can now be expressed using the determinant of the covariance matrix of beam parameters as:

$$A = \pi \sqrt{det V_{2D}} = \pi \sqrt{\sigma_{xx}\sigma_{x'x'} - \sigma_{xx'}^2} = \pi\varepsilon \tag{3.6}$$

The Twiss parameters can therefore be expressed using the rms phases as:

$$\beta_x = \frac{\langle x^2 \rangle}{\varepsilon_x} \tag{3.7}$$

$$\gamma_x = \frac{\langle x'^2 \rangle}{\varepsilon_x} \tag{3.8}$$

$$-\alpha_x = \frac{\langle x x' \rangle}{\varepsilon_x} \tag{3.9}$$

Up to this point, the linearised transformation of a particle beam in phase space has been shown in 2D, this can be expanded to more dimensions through using the same method corresponding to hyper-ellipsoids [52]. Emittances tend to be described in 2D, 4D or 6D, and in solenoidal beam optics to first order approximation (i.e. a stable lattice) the transverse and longitudinal phase spaces are decoupled therefore the 4D transverse and 2D longitudinal emittances are conserved under first order transformation [50]. Emittance is given in units of mm mrad which comes from the expression of the area of an ellipse with two axis x (displacement, mm) and x′ (divergence, mrad). The units are sometimes expressed in $\pi$ mm as well, which is the chosen preference for MICE and also in this thesis.

Up to this point, emittance has been conserved using non-canonical variables within a general field where the forces involved are independent of velocity. The conservation of emittance of a particle beam becomes invalid when acceleration is added to the system, through a phenomenon known as adiabatic damping. In order to restore Liouville invariance in this case, a canonical transformation is required introducing the concept of normalised emittance:

$$\varepsilon_n = \beta_{rel}\gamma_{rel}\varepsilon \tag{3.10}$$

where the relativistic factors $\beta_{\mathrm{rel}}$ and $\gamma_{\mathrm{rel}}$ (not to be confused with the twiss parameters) scale the beam divergence with momentum, in order to take account for the natural decrease in beam size when accelerated. Where $\mathrm{p} = \mathrm{m_0 c}\beta_{\mathrm{rel}}\gamma_{\mathrm{rel}}$ and $\mathrm{x}' \approx \frac{\mathrm{p_x}}{\mathrm{p_z}}$, we can write:

$$\varepsilon_n = \frac{\varepsilon}{m_0 c} \tag{3.11}$$

Finally this leads us to the definition of normalised emittance as defined by Penn [53], where in a solenoidal muon beam line such as that for MICE we can write the 4D normalised transverse emittance in phase space as:

$$\varepsilon_n\left(4D\right) = \frac{1}{m_\mu c}\sqrt[4]{\left|V_{4D}\left(x, p_x, y, p_y\right)\right|} \tag{3.12}$$

and the longitudinal 2D emittance as:

$$\varepsilon_n\left(2D\right) = \frac{1}{m_\mu c}\sqrt[2]{\left|V_{2D}\left(E, t\right)\right|} \tag{3.13}$$

## 3.5 Ionisation Cooling

In previous chapters, it was shown that for a proposed Neutrino Factory to reach its physics goals, it is important to maximise the flux of the neutrino beam, which is dependent on the number of muons which can be injected into the acceleration and storage rings. When muons are produced from pion decay after the target system, the phase space volume of the muon beam is too large to fit into the acceptance of the downstream acceleration systems. Therefore, 'cooling' of the transverse emittance of the muon beam is required.

Techniques for cooling particle beams are well established in accelerator physics, such as stochastic, electron and laser cooling [10], but none of these familiar methods are feasible for muons. The problem arises through the fact that these current methods take too long for effective cooling when considering muons, due to the particles rapid decay time. Therefore, a new cooling technique has been proposed to reduce the transverse normalised emittance of the muon required for a Neutrino Factory and eventually, a possible Muon Collider facility.

The novel method proposed to achieve the cooling of a muon beam, is ionisation cooling. The principle of ionisation cooling, is to pass the muon beam through a material (absorber) in which both transverse and longitudinal momentum is reduced, before replacing the longitudinal momentum through acceleration in RF cavities. This method of moderation and acceleration, shown in figure 2.4, is then repeated a number of times (dependent on cooling channel design), resulting in the net effect of a reduction in transverse emittance.

Ignoring any perturbation, ionisation cooling would be able to produce extremely small emittances, but there are effects during ionisation energy loss ($\frac{\mathrm{dE}}{\mathrm{dx}}$) such as multiple scattering and stochastic effects, such as energy straggling (the fluctuation in the energy loss), which counteract the cooling effect causing 'heating'.

The Bethe-Bloch equation [11] gives the mean energy change of a muon beam per unit length of an absorber, ($\frac{\mathrm{dE}}{\mathrm{dx}}$) as shown in figure 3.4 and the increase in angular spread per unit length of the beam, x′ is given by the Moliere scattering formula [11] which using a gaussian approximation that can be expressed as:

$$\frac{d\left\langle x'^2\right\rangle}{dz} \approx \frac{13.6^2}{\left(\beta_{rel}cp\right)^2 X_0} \tag{3.14}$$

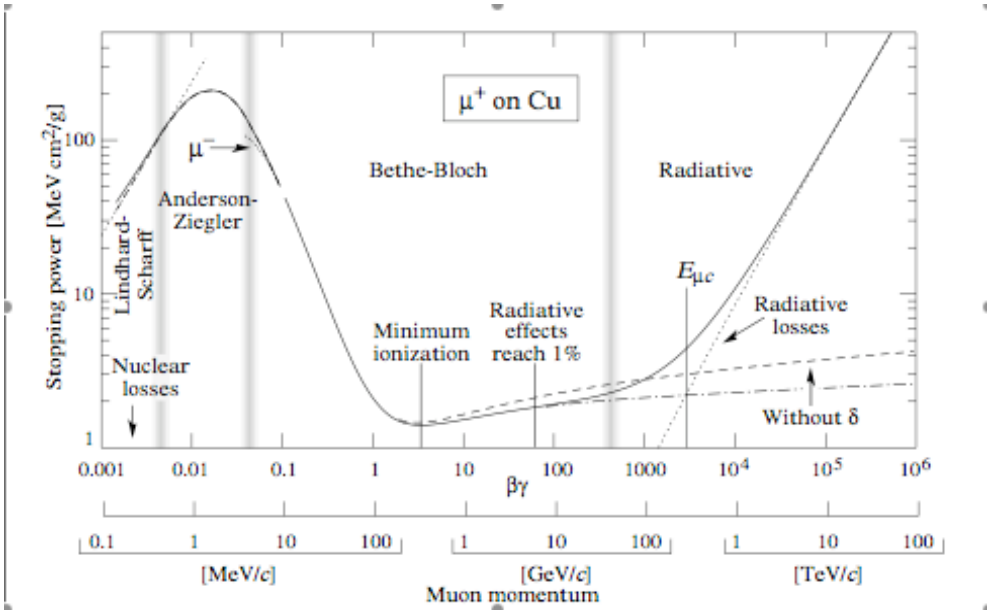


**Figure 3.4:** Energy loss of muons in matter. Muons in the energy range between $\sim 150$MeV/c and $\sim 400$MeV/c are minimum ionising particles and have been shown to be best for muon cooling channels [11].

The cooling and heating contributions during the ionisation cooling process can be related through deriving an expression for the change in emittance.

Utilising the beam matrix defintion in equation (3.5) and the ellipse equation in equation (3.4) we can write the rms geometric transverse emittance of a beam in 2D to be:

$$\varepsilon^2 = \langle x^2 \rangle \langle x'^2 \rangle - \langle xx' \rangle^2 \tag{3.15}$$

If the beam passes through a thin absorbing material of thickness dz, such that $\frac{\mathrm{dx}}{\mathrm{dz}} = 0$ can be assumed, when considering a cylindrically symmetric beam ($\alpha = 0$) and ignoring second order effects such as energy straggling we can ignore the last term in equation (3.15) such that there is no correlation between x and x′. Therefore, the change in emittance when passing the beam through the absorber can be given as:

$$2\varepsilon \frac{d\varepsilon}{dz} = \langle x^2 \rangle \frac{d \langle x'^2 \rangle}{dz} \tag{3.16}$$

we can then split the change in divergence of the beam into two terms for the separate cooling and heating contributions:

$$2\varepsilon\frac{d\varepsilon}{dz} = \left(\left\langle x^2\right\rangle \frac{d\left\langle x'^2\right\rangle}{dz}\right)_{cooling} + \left(\left\langle x^2\right\rangle \frac{d\left\langle x'^2\right\rangle}{dz}\right)_{heating} \tag{3.17}$$

Recalling that the divergence can be expressed as $\mathrm{x}' \simeq \frac{\mathrm{Px}}{\mathrm{Pz}}$ under constant conditions, gives the change in divergence as [6]:

$$\frac{d\left\langle x'\right\rangle}{dz} = \frac{d}{dz}\left(\frac{p_x}{p_z}\right) = \frac{1}{p_z}\frac{d}{dz}p_x + p_x\frac{d}{dz}\frac{1}{p_z} \tag{3.18}$$

if we ignore multiple scattering for a moment we can consider that in the absorber total momentum p is reduced by dp/dz, then after the absorber $\mathrm{p_z} \approx \mathrm{p}$ is restored while $\mathrm{p_x}$ is constant. This implies we can then ignore the last term in equation (3.18), therefore for the cooling term, we can express the change in $\mathrm{x}'$ to be:

$$\frac{d\left\langle x'\right\rangle}{dz} = \frac{x'}{p}\frac{dp}{dz} \tag{3.19}$$

substituting equation (3.19) into the cooling contribution of equation (3.17) and also substituting the multiple scattering equation (3.14) into the heating term of equation (3.17) now gives (3.20):

$$2\varepsilon\frac{d\varepsilon}{dz} = \left(\left\langle x^2\right\rangle 2x'\frac{x'}{p}\frac{dp}{dz}\right)_{cooling} + \left(\left\langle x^2\right\rangle \frac{13.6^2}{(\beta_{rel}cp)^2X_0}\right)_{heating} \tag{3.20}$$

recalling the expression for the transverse beta function, $\beta_\perp$ from equation (3.7) and to first order considering $\varepsilon^2 = \langle \mathrm{x}^2\rangle \langle \mathrm{x}'^2\rangle$ we know have:

$$\frac{d\varepsilon}{dz} = \varepsilon\frac{1}{p}\frac{dp}{dz} + \frac{\beta_\perp 13.6^2}{2p^2\beta_{rel}^2c^2X_0} \tag{3.21}$$

we can now transform equation (3.21) to be the change in normalised emittance for a muon beam through equation (3.10) and using the relativistic relations $\mathrm{E} = \gamma_{\mathrm{rel}}\mathrm{m_0c^2}$, $\mathrm{p} = \mathrm{m_0c}\beta_{\mathrm{rel}}\gamma_{\mathrm{rel}}$ where $\mathrm{c} = 1$ and $\mathrm{p}\frac{\mathrm{dp}}{\mathrm{dz}} \approx \mathrm{E}\frac{\mathrm{dE}}{\mathrm{dz}}$ such that the change in normalised transverse emittance of a muon beam can be expressed as:

$$\frac{d\varepsilon_n}{dz} = \frac{\varepsilon_n}{E\beta_{rel}^2}\left\langle\frac{dE}{dz}\right\rangle + \frac{\beta_\perp 13.6^2}{2m_\mu\beta_{rel}^3 X_0 E} \tag{3.22}$$

where the first term (cooling) is always negative, as $\left\langle\frac{\mathrm{dE}}{\mathrm{dz}}\right\rangle$ is always negative in the absorber. This expression for the reduction in normalised transverse emittance was first shown by Neuffer [54] and is the same as that given in the MICE proposal [47].

From equation (3.22) it can be seen that the heating term is proportional to the optical transverse beta function ($\beta_\perp$) and inversely proportional to the radiation length ($X_0$) of the absorber material. Therefore, for optimal cooling to be achieved strong focusing is required to keep $\beta_\perp$ small and the absorber should be a low Z (atomic number) material. In addition to this, high gradient RF cavities are required for re-acceleration, so the ionisation cooling process can be repeated many times before particle decay and beam losses take effect [47].

As previously mentioned, at small emittances multiple scattering (and stochastic effects) can completely counteract the cooling effect, the point at which this happens is called the equilibrium emittance, which is given when $\frac{\mathrm{d}\varepsilon_\mathrm{n}}{\mathrm{dz}} = 0$, therefore equation (3.22) can be re-arranged to be:

$$\varepsilon_n(equilibrium) = \frac{\beta_\perp 13.6^2}{2m_\mu\beta_{rel}X_0\left\langle\frac{dE}{dz}\right\rangle} \tag{3.23}$$

Measuring the equilibrium emittance will be one of the aims of MICE.

## 3.6 Emittance Measurement

The detectors in MICE, are required to make precision measurements of the emittance of the muon beam, both upstream and downstream of the cooling channel. They are also needed to identify unwanted particles within the beam, including the loss of any muons while traversing the channel. As previously described (section 3.4), emittance is defined as the volume occupied by a beam in phase-space. The coordinates required to measure the 6D emittance are $(\mathrm{x}, \mathrm{p_x}, \mathrm{y}, \mathrm{p_y}, \mathrm{E}, \mathrm{t})$, with the transverse 4D emittance therefore using $(\mathrm{x}, \mathrm{p_x}, \mathrm{y}, \mathrm{p_y})$. The Sci-Fi tracker will measure five of the six of coordinates, with the time coming from the TOF.

To achieve the precision emittance measurements demanded for demonstrating cooling, MICE will use a single-particle method based on standard particle-physics detection techniques rather then the conventional multi-particle methods used in beam instrumentation, with a 'virtual bunch' created offline. The necessity for a single-particle measurement comes from the use of solenoidal magnetic fields for the cooling channel and also the tracking devices where the emittance measurements will be made, as this leads to strong correlations between the six coordinates, introducing a bias in the emittance measurement [47].

The single-particle method will allow the properties of each particle to be measured before and after the cooling channel, where a figure of merit for the experimental resolution has been determined such that the emittance measurement is not significantly affected [47] [55]. This figure of merit requires that the rms resolution of each phase space variable measured, must be better than 10% of the rms beam size of the same variable at equilibrium emittance (see section 5.6). Apart from the time which comes from the TOF, these phase space measurements from the tracker, are discussed in more detail in chapter 5.

The other advantage of single-particle measurements, is that the transmission can be determined. Through measuring each particle as it enters and leaves the cooling channel, particle losses can be determined and separated cleanly from the effect of cooling.

Figure 3.5 shows initial simulations [9] based on the interpretation of normalised 4D emittance shown in equation 3.12. It shows the simulated expectations of the transmission and change in emittance expected from MICE, compared to the input emittance for the baseline configuration and central momentum of 200MeV/c. We can see that at very low input emittance values the beam goes from being cooled to heated, passing the equilibrium emittance point, where input and output emittance are equal. For the MICE baseline configuration the equilibrium emittance is considered to $\sim$2.5 $\pi$ mm. At larger input emittance values, the transverse cooling is shown to increase, while transmission decreases, which is due to the larger beam size resulting in more losses through scraping in the cooling channel. Although not shown in figure 3.5, longitudinal emittance is expected to increase by $\sim$10% for all input emittance values.

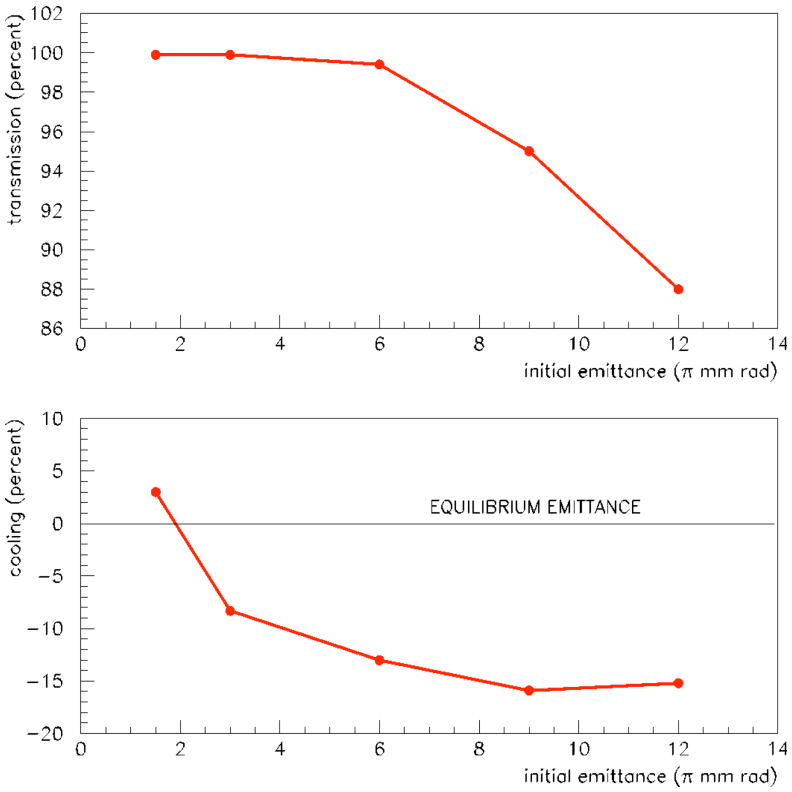


**Figure 3.5:** Predicted transmission and cooling measurement for the baseline MICE configuration and central momentum of 200MeV/c [9]

## 3.7 Particle Detectors

MICE will use two identical trackers, one will be placed upstream and one downstream of the cooling channel. These tracker devices along with the TOF counters immediately upstream and downstream of the cooling channel, will provide the muon phase space measurements. In addition to these detector systems, there is another TOF counter further upstream for a $t_0$ timing signal. MICE will also have a Cherenkov detector and downstream Electromagnetic Calorimeter required for particle identification. These will all be briefly discussed in turn but for a more detailed description of each detector system see the MICE Technical Reference Document [9].

### 3.7.1 TOF

A set of time of flight scintillators (TOF0, TOF1 and TOF2) will be used for MICE, with both TOF0 and TOF1 placed upstream of the cooling channel and TOF2 downstream, as shown in figure 3.1. All three counters consist of two perpendicular planes (x-y arrangement)[‡] of 2.5cm thick scintillating slabs shown in figure 3.6. Each slab is readout at both ends by a fast photomultiplier via light guides.

TOF0 and TOF1 will be used for upstream muon identification and will also provide the trigger for MICE in coincidence with the ISIS clock. In addition to this, TOF1 will provide the incoming muon timing signal (relative to the RF phase) which is required for the longitudinal emittance measurement, with TOF2 providing the outgoing muon timing signal. This downstream counter TOF2 in coincidence with TOF1 will also be able to select particles that have passed through the entire cooling channel, therefore allowing the emittance measurements due to cooling to be differentiated from those due to losses or decays.

The TOF scintillator materials and fast PMTs needed for all three counters have been studied in detail depending on their own specific needs to produce the expected timing resolution of 50ps [9]. This timing resolution along with a related x,y measurement will provide both effective 99% rejection of beam pions and also determine the RF phase to a satisfactory precision of 5°.

The most upstream counter TOF0 is the smallest of the three TOFs. The reason for this is that TOF0 is placed $\sim 10m$ upstream of TOF1 where the size of the beam is smaller and the rate of the particles greater. The TOF0 planes are made up of ten slabs with a width of 4cm giving TOF0 an overall size of 40x40cm$^2$. The other upstream counter TOF1 is placed just in front of the lead diffuser. Its planes consist of seven 6cm wide slabs giving it an overall size of 42x42cm$^2$. Since TOF1 is placed next to the cooling channel it is in a high magnetic field region, this has led to steps being taken to shield both the PMTs and the detector itself from fringe fields. The final counter TOF2 is situated downstream, immediately after the spectrometer and before the calorimeter. It is the largest of the TOF counters, with each plane consisting of ten 6cm slabs resulting in an overall size of 60x60cm$^2$. Like TOF1, it is situated in a high magnetic field region, so again similar shielding requirements are foreseen.

[‡]The coordinate system used in MICE is right-handed with the z-axis pointing in the direction of the beamline, the x-axis horizontal and the y-axis vertical.

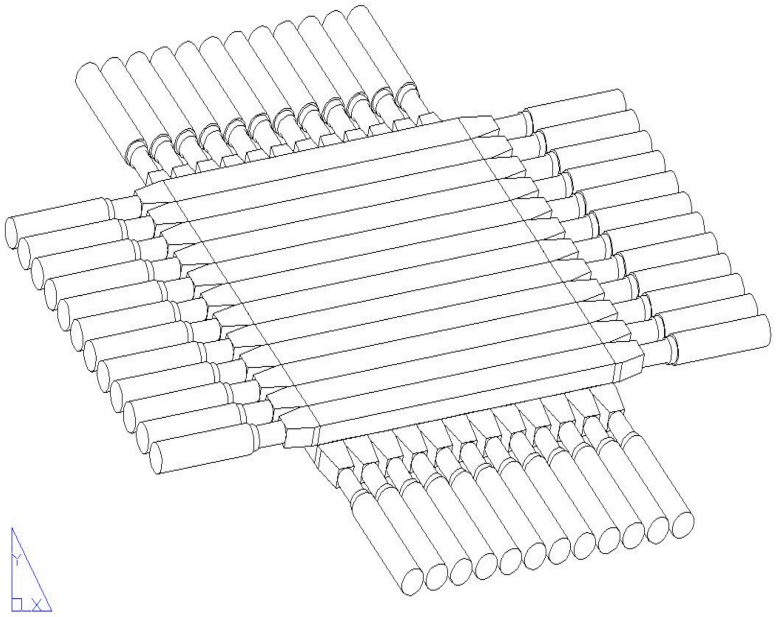

**Figure 3.6:** X/Y plane structure for TOF0, showing slabs, lightguides and PMT collars and housing units (latest TOF0 consists of 10 slabs instead of the 12 shown here) [9]

### 3.7.2 Cherenkov

As MICE requires a clean muon beam, the inclusion of a threshold Cherenkov detector (CKOV) is needed upstream for pion/muon/electron separation in addition to the time of flight technique. The Cherenkov device is situated immediately upstream of TOF1. At this point the majority of beam pions have decayed to muons, but there still exists a small contamination by pions and decay electrons. The necessity for the Cherenkov to complement the time of flight counters upstream is due to MICE being operated in a large range of momenta, where at the high-momentum region the TOF alone can not provide the muon-pion separation required. As already mentioned, the main issue comes from the large range of beam momenta that will be used for MICE, where it is clear that no single radiator material exists with a refractive index that is sufficient to distinguish between pions and muons for all the different beam momenta. Therefore, MICE will use a "dual" radiator CKOV

setup, where two planes of Aerogel will be located "sequentially" along the beam line with refractive indices of n = 1.07 and n = 1.12 respectively. The size of each CKOV radiator unit is 78.6 x 78.6 $cm^2$ and each unit is readout by four PMTS. The expected photon yields are shown in figure 3.7 and define three momentum regions (I, II and III) that establish the respective muon and pion thresholds.

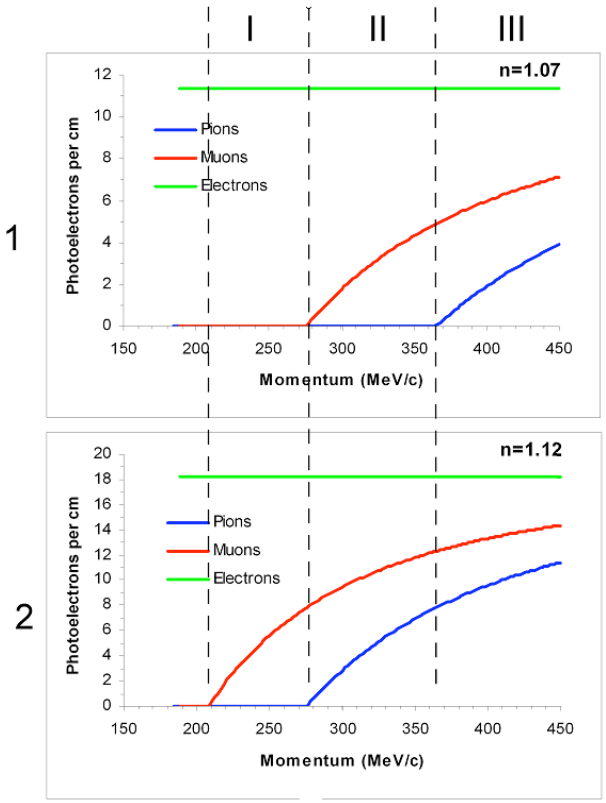


**Figure 3.7:** Cherenkov Detectors expected photon yields for the two radiators (1) n = 1.07 and (2) n = 1.12 [9]

When the momentum is above 365MeV/c (region III), muons and pions will generate light in both radiator units making them indistinguishable. This is not considered to be an issue, as MICE does not plan to operate in beam momenta exceeding 350MeV/c. In the momentum range 276MeV/c < p < 365MeV/c (region II), only particles that trigger both radiators are considered muons. In the momentum range 207MeV/c < p < 276MeV/c (region I), the particle is considered to be a muon if only the first radiator (n = 1.07) is triggered.

Simulations have shown that for beam momenta above 207MeV/c rejection of pion contamination is > 99% [9], below this momentum value CKOV is shown to be blind

to pions and muons but as indicated previously, time of flight on its own is sufficient for pion discrimination at low momenta.

### 3.7.3 Sci-Fi Tracker

Two scintillating fibre trackers will be used in MICE, one upstream of the cooling channel and one downstream. Each tracker will be embedded inside a 4-Tesla magnetic field providing the full set of six muon parameters (with TOF), required for an emittance measurement. The majority of the authors work is focussed on the construction, software and testing of the trackers, therefore the trackers will be discussed extensively in the subsequent chapters of this thesis.

### 3.7.4 Electromagnetic Calorimeter

As muons have a relatively short lifetime (2.2$\mu$s at rest) it is expected in MICE, that roughly 1% of the muons passing through the spectrometers and cooling channel will decay [9]. These decays produce electrons which, along with undecayed pions, need to be identified as they introduce considerable systematic errors on the emittance measurements. Downstream PID is primarily achieved by kinematic measurements using TOF1, TOF2 and the downstream tracker which provides a rejection of the undecayed pions and roughly 80% of the decay electrons. However, this remaining 20% of contamination is still deemed to have a detrimental effect on the emittance measurement, so downstream of TOF2 an electromagnetic calorimeter (EMCAL) will be used for this additional electron-muon separation that is required.

The MICE EMCAL is based on the calorimeter designed for KLOE [56]. It involves scintillating fibres of 1mm diameter interspersed between 0.3mm thick lead layers. The overall size of the EMCAL is 120 x 120 $cm^2$ transverse to the beam with a total width of 16 cm. The EMCAL light output is readout through PMTs via lightguides. The downstream PID performance is described in [8].

## 3.8 Cooling Channel

In section 3.5, ionisation cooling was described, showing that to demonstrate cooling, the normalised emittance of a muon beam needs to be reduced. The equation derived

(3.22), giving the approximate rate of change in normalised emittance was shown to be dependent upon the energy loss and radiation length of the absorber material and also the ability to have a strongly focused beam. As these three elements are crucial to demonstrate cooling, they are the key influence in the design of the study II and MICE cooling channels, a brief overview of the experimental components will now be described in turn, for a more detailed description see [34] and [9]

### 3.8.1 Absorbers

'Cooling' for MICE is achieved by the use of liquid-hydrogen ($LH_2$) absorbers. In the MICE cooling channel there are three Absorber Focus Coil Modules (AFC) as shown in figure 3.1. The goal of the absorbers is to reduce the normalised emittance of the MICE muon beam. Through ionisation, the muons lose energy in the absorber material, this reduces their momentum in both the longitudinal and transverse directions, which results in an increase in their phase space density. The main considerations in terms of design of the absorber were to minimise multiple scattering, achieve a sufficient heat transfer rate so the absorber density and temperature can remain uniform and also allow safe operation.

After reviewing various options, liquid-hydrogen was deemed to be the best option in terms of performance for the absorber material. This comes from liquid-hydrogen having a large ionisation energy loss rate i.e. 'cooling' and a small probability of multiple scattering i.e. 'heating'. To further reduce the effect of heating, the absorber is placed within a high-gradient focusing magnetic field. The focusing solenoid and the absorber itself are one single module, which is where the name Absorber Focus Coil Module (AFC) comes from, as shown in figure (3.8).

In terms of design, the absorber has a length of 35cm and a diameter of 30cm and has a hydrogen volume of 21 litres, sealed within aluminium windows and cooled using a cryocooler. The windows are curved instead of cylindrical so they can withstand higher pressure, therefore allowing for a thinner window, helping reduce the effect of multiple scattering even more.

The absorber modules are also removable, allowing for the possibility of using different materials, for example lithium-hydride (LiH) which although achieves slightly less 'cooling', it is more practical than liquid-hydrogen (see section 2.2.4). Safety issues have also played a key role in the design, including the choice of having two

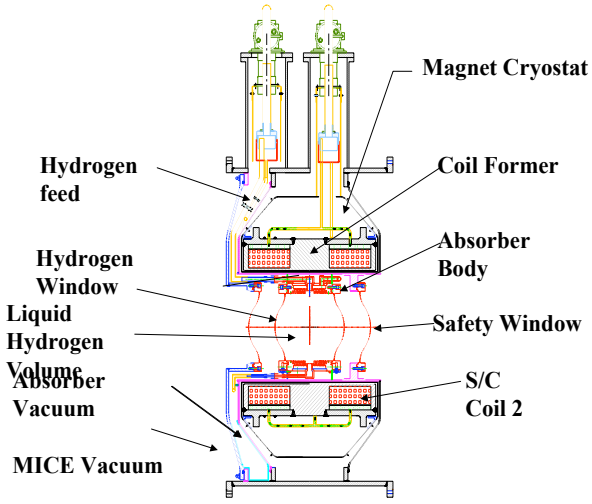


**Figure 3.8:** AFC Module [9]

sets of aluminium windows. The inner window is the absorber itself and the outer window provides a safety buffer in the event of a failure or leak from the absorber. The space between the two windows is vacuum pumped.

### 3.8.2 RF Cavities

Once a muon has passed through an absorber and lost both longitudinal and transverse momentum, it passes through the RF cavities where just the longitudinal component of momentum is increased, resulting in the final effect of a reduction in transverse momentum with respect to longitudinal momentum i.e. "transverse cooling".

In the MICE cooling channel, there are two assemblies of 201-MHz RF cavities (figure 3.9). These cavities, also situated in a focusing solenoid, are based on the same design as those used for the Neutrino Factory Study II cooling channel [34]. The MICE RF cavities will have a maximum operating gradient of 8MV/m (compared to the Study-II cooling specification of 16MV/m) due to financial limitations on the power available to run the cavities, thus a maximum accelerating RF voltage of 21MV will be provided. The linac will therefore operate on crest and be designed in such a way that, all the muon energy lost in the absorbers will be restored.

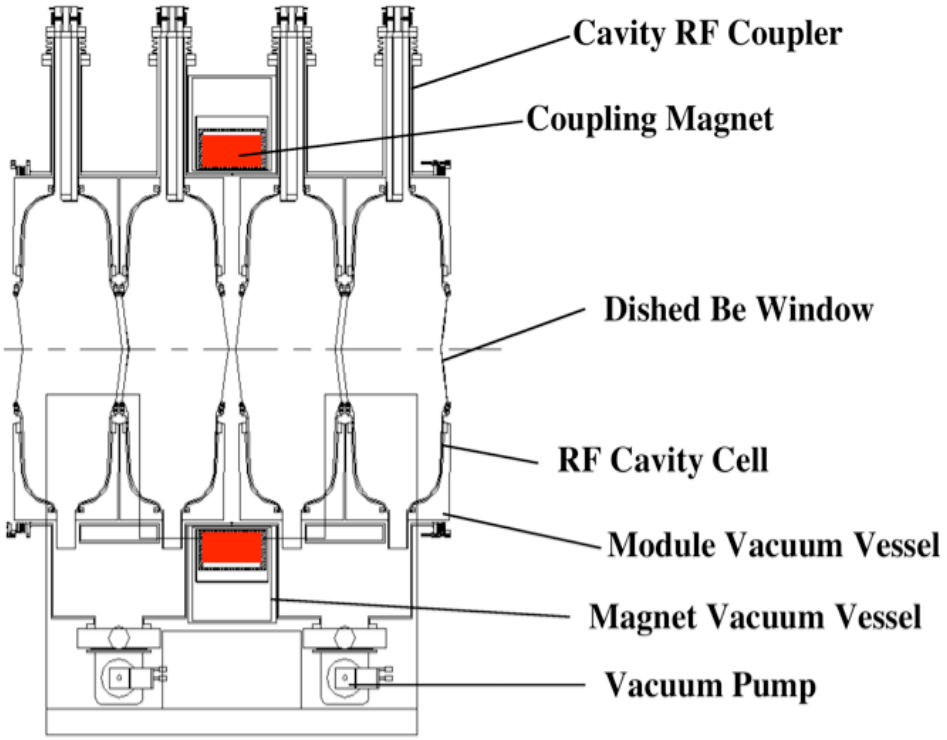


**Figure 3.9:** RF Coupling Coil Module (RFCC) [9]

It is also worth mentioning that the RF cavities produce very large dark current and secondary X-ray backgrounds, via Bremsstrahlung, which needs to be considered in regards to the particle detectors. As mentioned previously, this is one of the reasons for the addition of the third and final absorber as it is thick enough to absorb all the electrons produced by the dark currents from the cavities. The tracking detectors are also built from low-Z material, therefore are expected to be able to distinguish between hits generated by muons and those generated by possible X-rays passing through the absorber.

### 3.8.3 MICE Magnetic Channel

The MICE cooling channel keeps the muon beam confined through the use of a solenoidal magnetic field. There are seven magnetic assemblies, which in total consist of eighteen superconducting solenoid coils. The seven assemblies are:

- Two spectrometer solenoids;

- Three Absorber Focus Coils (AFC); and
- Two RF coupling coils

The full MICE cooling channel is physically symmetric about its centre (z = 0). The field-flip configuration (needed for cancelling the build up of canonical angular momentum [50]) and the on-axis $B_z$ are both shown in figure 3.10.

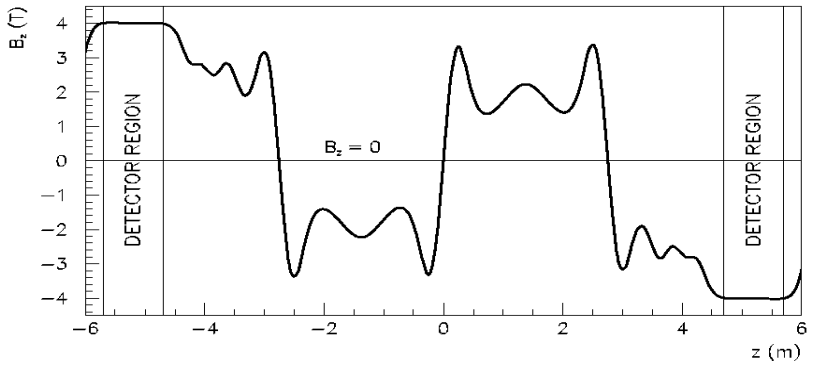


**Figure 3.10:** Longitudinal magnetic field $B_z$ for the baseline MICE cooling channel with central momentum of 200MeV/c and a transverse beta function of 42cm at the centre of the absorbers [9]

The three absorbers each sit between two focus coils, these coils have the desired effect of reducing the transverse beta function $\beta_\perp$ required to deliver optimal cooling. At the centre of each of the two RF cavities there is a single coupling coil. Two pairs of matching coils, match the beam (such that there is a smooth transition from the detector region to the cooling channel, as shown in 3.10) between the cooling channel and the upstream and downstream spectrometers. The spectrometers themselves consist of three coils each, providing a uniform 4-Tesla field in the detector region of the spectrometer, which meets the criterion that ($\Delta B/B < 0.01$) for the full 1m length of the tracker. This uniform field region can be seen in figure 3.10.

## 3.9 MICE Software

An essential aim of MICE is to measure the beam dynamics with a high level of precision and compare these results with simulations. The simulation, reconstruction and analysis of MICE is carried out by the G4MICE software package [57] [9]. G4MICE is written in C++ and got its name by originally being conceived to perform GEANT4 simulations, which is still the case, but now also provides other services as well beyond simulation.

The MICE particle detectors will be interspersed between the elements of the cooling channel (absorbers, RF cavities and solenoid magnets) as well as the beamline (quadruple magnets), therefore a Monte Carlo framework is essential, where all elements are accurately modelled. As previously mentioned the package chosen to do this is the GEANT4 toolkit [58] which is becoming the standard HEP physics simulation package as it is flexible, can be extended and includes the functionality to support complex geometries and up-to-date models of physical processes.

G4MICE has the ability to simulate the beamline and detectors and has been used to study the overall experimental design and performance as well as detector optimisation, which has required detector responses and simulation of electronics. In addition to simulation, G4MICE contains applications to calculate accelerator physics parameters like emittance and all detector reconstruction. The same reconstruction software will be used to for both real data coming from the experiment as well as from simulation, an example of which has already been successfully shown through the simulation and analysis of a test beam, used to study the performance of a prototype tracker (see chapter 6).

The G4MICE software is under continuous development and its functionality has been grouped into packages implemented as libraries. The package dependencies are shown in the domains diagram in figure 3.11. G4MICE also uses external packages which are shown in the bottom line of figure 3.11. Further external packages used include G4Beamline [59] and ICOOL [60] which can be used for simulating and tracking particles through an accelerator system, such as the MICE beamline coming from ISIS. A quick overview of some of the G4MICE package contents are now given[§], for more detailed descriptions of all packages and the software package as a whole, see [9] and [57]):

[§]The packages marked with a $*$ indicate those in which the author played a role in developing.

- *Persist*: "transient" objects are made persistent, for example classes such as SciFiHit, SciFiKalTrack can be stored and saved to file for later use.
- *Simulation**: generation and tracking of particles through MICE including all physical processes.
- *Analysis**: tools for calculating physcis output including beam parameters, bunching etc.
- *DetModel*: handles modelling of the detector volumes (geometry and materials) and controls data output for simulation of detector response (generation of detector hits).
- *EngModel*: handles modelling of the cooling channel components and electromagnetic fields (absorbers, RF Cavities, magnet coils etc.).
- *Optics*: calculates first order transfer maps such as betatron functions, periodic lattices and field maps.
- *DetResp**: simulates the electronics response of the detectors i.e. creates digits from the simulated data (hits).
- *Recon**: uses information from either DetResp or real experimental data to reconstruct tracks and other data for analysis.
- *BeamTools*: tools for modelling quadrupoles, solenoids and RF fields.
- *Config**: configuration setups the geometry, cabling information, materials and all physical data.
- *Calib*: handles detector calibration data such as pedestals, electronic noise and dead channels.
- *GSL*: GNU scientific library, adds mathematical functionality etc.
- *GEANT*4: HEP simulation toolkit.
- *CLHEP*: utility library.
- *Kalman*: calculates optimal track parameters (see chapter 5).
- *ROOT*: analysis toolkit.

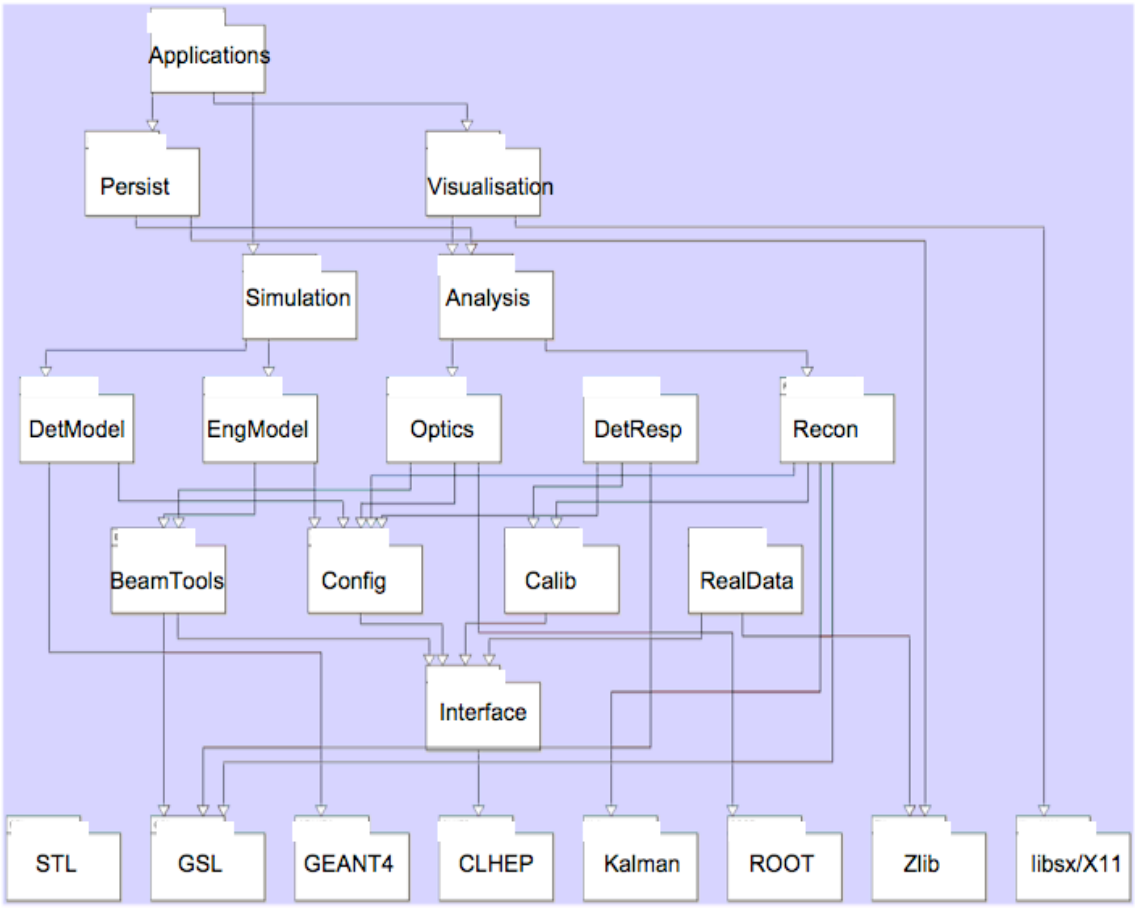


**Figure 3.11:** G4MICE architecture, showing the various packages where the arrows show that packages can use other packages below them or their daughters if connected.

The applications package is the highest level domain shown in figure 3.11, which contains all executables, existing key applications include simulation, digitisation and reconstruction. Other user-defined special purpose programmes can and have been written where one or more of the G4MICE packages can be used and linked. Examples of this, are the individual applications written by the author in G4MICE in order to simulate the beam, the trigger and reconstruct the data (Monte Carlo and Real data) of a beam test at KEK (chapter 6).

In chapter 5 of this thesis, an overview and description of the tracker software in G4MICE has been given, focussing mainly on the tracker reconstruction. Also data from the test beam described in chapter 6, has been analysed using G4MICE.

## 3.10 Evolution of MICE

The MICE experiment will be constructed and operated in six defined stages as shown in figure 3.12. This allows preparatory studies to be carried out before the final stage where a full MICE cooling channel will be assembled and tested under various conditions.

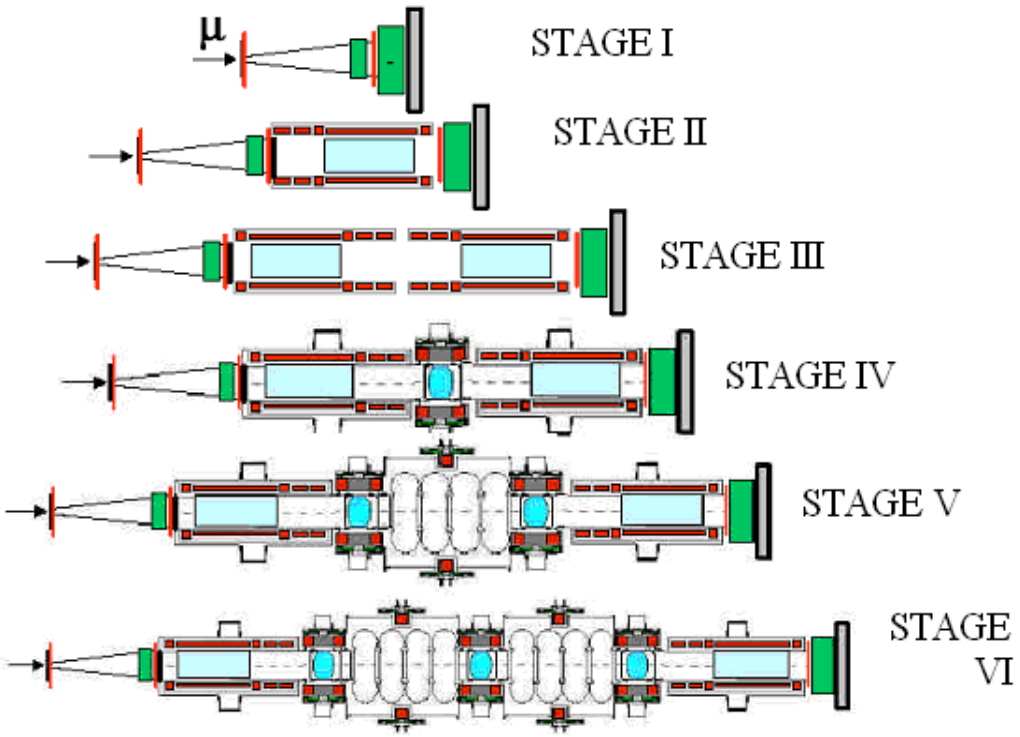


**Figure 3.12:** The six stages of MICE [9]

Stage 1, which at the time of writing is the current status of the experiment, PID detectors will be calibrated and characterisation of the beam will be achieved. Following this (stage II), the first spectrometer will be placed into the beam where it will be calibrated and provide the first 6D emittance measurement, allowing the quality of matching between the beamline and the MICE channel to be optimised. Stage III, will see the second spectrometer installed, which will enable the two spectrometers to be calibrated against each other to test for systematic errors, as at this point in construction there is no material between them, so beam properties

measured should be the same for both. By the completion of stage III testing, all particle detectors should be calibrated and the beam characteristics understood.

Stage IV will provide the first measurement of cooling, by the addition of one absorber focus coil (AFC) module between the two spectrometers. Experience will be gained in operating the absorber under a variety of focussing conditions and in measuring energy loss and multiple scattering which are key parameters to the theory of ionisation cooling. In stage V, the first RF and coupling coil (RFCC) module will be introduced, along with a second AFC module. At this juncture, the true performance capabilities of the cooling channel will start to be studied. Finally in stage VI, the full baseline MICE channel will be realised with the inclusion of the final RFCC and AFC modules.

The full MICE channel will be operated under various different beam settings with the input emittance ranging from $2\pi$mm (equilibrium emittance) to $10\pi$mm at central momenta between 140 and 240 MeV/c. In terms of timescale, the stages of MICE are obviously dependent on when certain equipment construction can be completed and then implemented at RAL, which varies for each, but the current planned completion date for MICE to achieve all its goals is 2013.

# Chapter 4

# SciFi Tracker

An overview of MICE in the previous chapter, showed that to demonstrate muon ionisation cooling with a section of cooling channel, requires precision measurements of the relative change in emittance. To achieve this, MICE is conceived as a single-particle experiment with spectrometers placed upstream and downstream of the cooling channel, where the parameters of each individual muon will be determined when entering and exiting the channel. The MICE spectrometers, are superconducting solenoids instrumented with a charged-particle tracking device. MICE, will use scintillating-fibre (Sci-Fi) trackers, that utilise the speed and efficiency of scintillation from organic plastic fibres, readout with visible-light photon counters (VLPCs). The remainder of this thesis will present details of the detector construction, it's simulated performance - testing the pattern recognition and track fit reconstruction and also commissioning and operation of a full scale prototype. This chapter, will give an overview of the detector operating principle, the design, construction and the readout system.

## 4.1 Tracker Specification and Development

The two spectrometers placed immediately upstream and downstream of the cooling channel are required for MICE to perform measurements of beam transmission and emittance reduction with an absolute precision of $\pm 0.1\%$. To achieve this, the Sci-Fi trackers need to have a high track-finding efficiency in the presence of large dark current and X-ray backgrounds coming from surrounding high-gradient RF cavities.

In order to demonstrate that the Sci-Fi tracker(s) can reach the specification required with realiable and efficient operation, a number of key steps have been taken in the development of the device:

- Through the construction, commissioning and operation of an initial full-scale prototype (3 stations) using cosmic rays in 2003, the level of light yield, cross talk, dead channel rate and degree of RF pickup were checked to see if they were consistent with the efficiency and reliability required [12].
- Through simulation of the MICE stage VI setup, the performance of the tracker pattern recognition and track fitting algorithms has been assessed (chapter 5), to check that adequate resolution in the reconstructed track parameters can be determined, therefore allowing the measurement of emittance to be made with an absolute precision of 0.1%.
- A second full-scale prototype (4 stations) was operated and studied, this time in a beam test at KEK in late 2005 (chapter 6). The purpose of this second prototype was to analyse the construction (with upgrades and new additions) and operation of the device in a realistic environment, investigating light yield and alignment and also to demonstrate tracking in a solenoidal magnetic field.
- Through the experience gained from the construction, commissioning and testing of the prototypes, issues found were resolved through developing quality assurance (QA) procedures for the final detector construction process. Once, the detectors had passed the QA tests [9], the final five station trackers were examined in cosmic-ray tests at RAL in 2008 and 2009 (chapter 7), before they are eventually installed in the MICE hall.

## 4.2 Operating Principle

Charged particle tracking in MICE is based on the production of light in plastic scintillating fibres. Charged particles pass through plastic optical fibres and deposit energy, which is converted into scintillation light. Through the use of fluorescent, organic dyes and mulitclad fibres a fraction of the light produced is optically trapped within the fibre. One end of the fibre cylinder is mirrored, allowing all the trapped light to travel to the other end of the doped fibre where it is mated to 'clear' optical

fibre. The clear optical fibre then transports the light over a certain distance to the photosensor.

There are many technical challenges that need to be put in place for this method of particle detection to work, with the performance of the tracker determined by the light yield and fibre pitch (i.e. spatial resolution). Therefore, active fibres need to be fixed and precisely known. The scintillation light produced needs to be high enough for detection, whilst at the same time keeping a low level of self-absorption. To reduce the effect of multiple scattering to an acceptable level, a specific fibre diameter needed to be determined. The optical transmissions of the fibre-to-fibre interconnections need to be near unity and clear fibre needs to be able to 'pipe' light over large distances to the photosensor, so little or no light is lost. Finally, the photosensor itself is required to have a high rate capability and high quantum efficiency. After all this, the signal coming from the detector is given as a mean number of photoelectrons $\langle N_{PE} \rangle$. Finally, the data is reconstructed offline to determine the track parameters.

## 4.3 Mechanical Design & Construction

The Sci-Fi trackers requirement to deliver efficient tracking with high resolution, has had a direct impact on the mechanical design of the device and its components. From making sure all ∼22,000 scintillating fibres per tracker are arranged and fixed carefully to stations, so their positions remain consistent and known, all the way through to the alignment of the stations relative to each other within the trackers and subsequently within the nominal beam line axis.

The baseline design consists of a five-station tracker placed in a solenoidal magnetic field (figure 4.1), where each station has three planar layers of scintillating fibre laid out in a 'v, x, w' arrangement on a station body, with an active diameter of 30cm, required to allow precision measurements [9]. The tracker will be placed inside the 40cm inner bore of a superconducting solenoid producing an axial field of 4T, which will be uniform at the 1% level over the full 1.10m tracker region. The scintillating fibre diameter chosen to limit multiple scattering is 350$\mu$m [12], but to reduce the cost of readout electronics, the fibres will be bundled into groups of seven and then mated to clear fibre light guides, with a diameter of 1.05mm, at the station via station connectors. The light guides, will then transport the scintillation light from

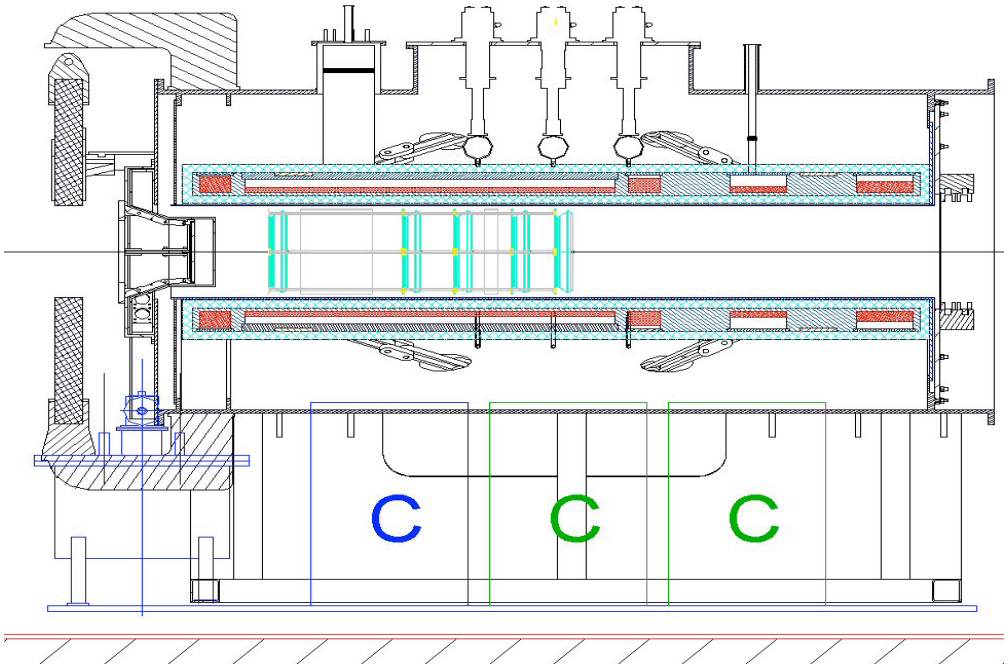


**Figure 4.1:** Engineering drawing of the upstream spectrometer, showing the five stations of the tracker, within the solenoid bore and the optical patch panel assembly (shown on the far left of the drawing). [9]

the stations to the readout electronics via an optical patch panel, which is required to form a gas seal.

The choice of readout electronics, is based on that used by the DØ central fibre tracker (CFT) [61], which uses visible light photons counters (VLPCs) [62]. The following sections will give an overview of each component of the MICE Sci-Fi tracker, along with brief details of the construction process, in which the author played a role, within the tracker team. For a more comprehensive discussion on the equipment and construction details see [9] [12].

### 4.3.1 Scintillating Fibre Setup

The scintillating fibres in MICE are 350$\mu$m diameter Kuraray, double clad, doped polystyrene (PS) fibres. The fibres are dyed with a primary and secondary dopant, para-terphenyl (pT) and 3-hydroxyflavone (3HF) respectively. The primary dopant is required to increase the speed of energy transfer, from the energy deposited by a

| Component | Parameter | Value |
|---|---|---|
| **Scintillating fibre tracker** | Scintillating fibre diameter | 350 μm |
| | Primary dopant, pT, concentration | 1.25% (by weight) |
| | Secondary dopant, 3HF, concentration | 0.25% (by weight) |
| | Fibre pitch | 427 μm |
| | Estimated light yield per doublet (photo-electrons) | 10.6 |
| | Number of scintillating fibres per optical readout channel | 7 |
| | Position resolution per plane | 470 μm |
| | Views per station | 3 |
| | Radiation length per station | 0.45% $X_0$ |
| | Stations per spectrometer | 5 |
| | Station separation: 1 – 2 | 45 cm |
| | Station separation: 2 – 3 | 35 cm |
| | Station separation: 3 – 4 | 20 cm |
| | Station separation: 4 – 5 | 10 cm |
| **Tracking volume** | Sensitive volume: length | 1.10 cm |
| | Sensitive volume: diameter | 30 cm |
| **Spectrometer solenoid** | Magnetic field in tracking volume | 4 T |
| | Field uniformity in tracking volume | 1% |
| | Field stability | 1% |
| | Bore diameter | 40 cm |
| | Pressure in magnet bore | Vacuum |

**Table 4.1:** Tracker Module Key Parameters. [9]

charged particle (passing through the fibre), via ionisation radiation in the PS base. The secondary dopant, 3HF, is then required as a wavelength shifting dye, which is spectrally matched to the pT, so it efficiently absorbs the radiation emitted by the pT ($\lambda \sim 350$nm) and emits it at a longer wavelength ($\lambda \sim 525$nm) required for the light to travel further within the plastic and to match the spectral response of the VLPCs so that greater quantum efficiency is provided [61] [63]. The concentration of these two dopants has been optimised, so that the light yield is maximised and the optical cross talk from fibre-to-fibre minimised. The baseline specification for the dopant concentrations was chosen, based on experience gained by DØ and also on the light yield results from the initial prototype test [12].

In principle, the expected light yield can be calculated by estimating the number of photons generated by the passage of a minimum ionising particle. However, various parameters need to be entered into the calculation which are either unknown or uncertain, such as the energy-to-photon conversion efficiency, capture probability, attenuation length, lost light at various interfaces along the readout chain and the quantum efficiency of the photosensors

Through calculations extrapolated from the DØ CFT measured light yield results (which used scintillating fibre with 830$\mu$m diameter), the expected mean number

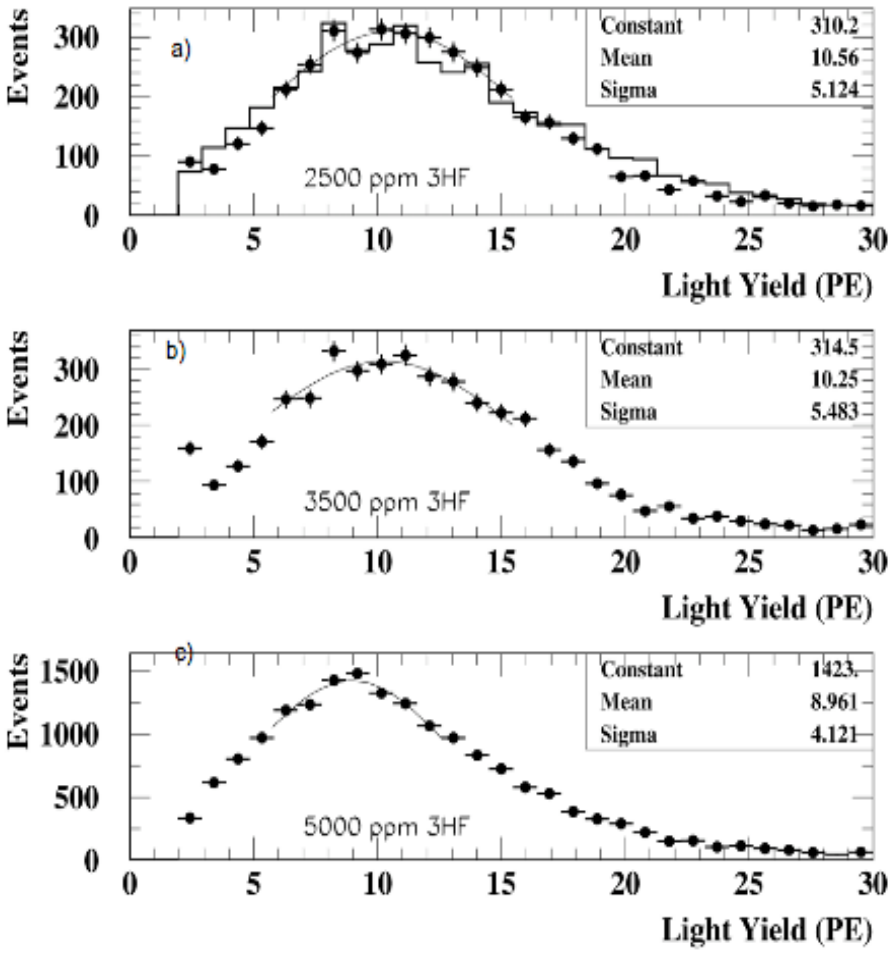


**Figure 4.2:** Pulse height distributions from the cosmic ray test of initial tracker prototpe, for the different concentrations of 3HF: (a) 2500 ppm; (b) 2500 ppm; (c) 5000 ppm. The points are for data and in (a) the histogram is from MC simulation. The mean of a gaussian fit to the peaks gives the most probable light lield (PE). [12]

of photo-electrons for the MICE trackers, was found to be $\langle N_{PE} \rangle \simeq 11.2$. After, including an extra interface for the MICE tracker readout ('patch panel connectors'), where a light transmission of $\geq 90\%$ is expected, an overall expected light yield of approximately $\langle N_{PE} \rangle \geq 10.1$ is found, for the MICE trackers [64].

In order to test this approximation, it was decided by the MICE tracker team, to measure the light yield of a full scale prototype, in a cosmic ray test at Fermilab, using the chosen baseline MICE scintillating fibre, based on the scintillating fibre used by the DØ CFT. It was also considered a useful test to examine the effect of different concentrations of the secondary dopant (3HF), on the light yield performance. The results, as shown in figure 4.2 [12], show that when considering the

2500 ppm 3HF concentration (now the baseline), the measured results, are in close agreement with those estimated through calculation.

The small diameter of 350$\mu$m for the scintillating fibres needed to reduce multiple scattering, had the knock on effect of producing a very large channel count and therefore electronics cost. To solve this, fibres were 'bundled' into groups of seven, to form a single channel, which is then readout, via one clear fibre waveguide (see figure 4.6). The effect of this, is a sensitive channel element that is 1.63mm across, giving a resolution of 470$\mu$m, which has been shown by simulation to be acceptable in [12] and in chapter 5 of this thesis. There are three fibre planes per tracker station, where each plane consists of a scintillating fibre doublet layer, with the two layers offset, as shown in figure 4.3, leaving no dead spaces. The three views will all be at an angle of 120° to one another, on the station body, where each view will provide between 212-214 scintillating fibre channels (bundles of seven) to be readout, as shown in figure 4.6 and 4.7.

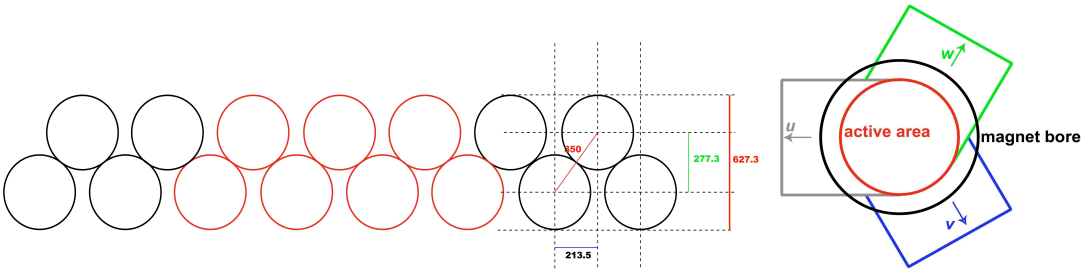


**Figure 4.3:** Arrangement of scintillating fibres in a tracker station. On the left, a cross-sectional view of a fibre doublet layer is shown, with the red fibres indicating a single readout channel (bundle of seven fibres). On the right, the 120° angle between each of the three doublet layers per station is shown. [9]

The doublet fibre layers were made, following the same techniques, as that used by the DØ experiment for their fibre tracker (CFT). Firstly, all fibres are cut to length, with one end of the fibre polished, so that a vapour deposited aluminium mirror can be applied. Reflectivity of the mirrors has not been studied for MICE, however when using this exact technique, DØ found that an average reflectivity, of approximately 90% was achieved [64]. The doublet fibre ribbons were then constructed, using precision techniques (described in detail in [9] and [12]), which included grooved moulds for fibre placement and applying adhesive, which is allowed to cure, once all fibres in the doublet ribbon are in place.

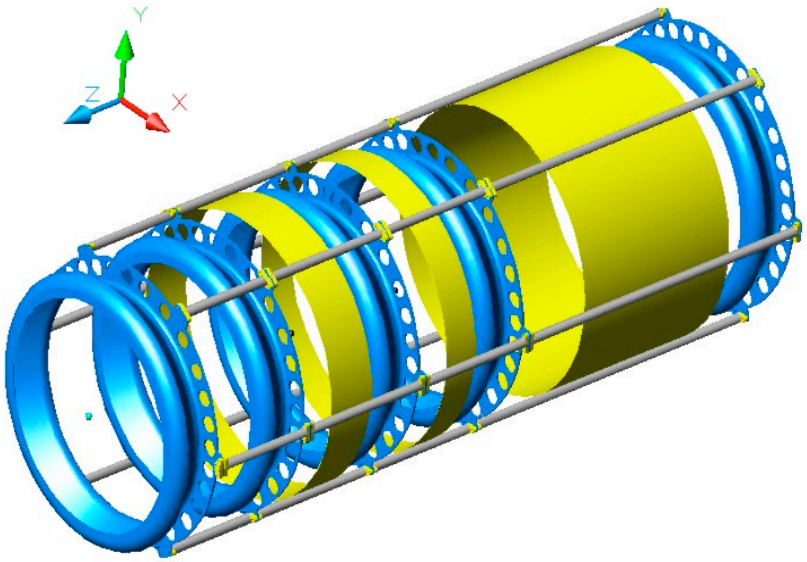


**Figure 4.4:** Schematic drawing of the tracker, showing the five station bodies, which are held in position and supported by carbon fibre rods. [9]

### 4.3.2 Sci-Fi Tracker Structure and Stations

Each of the Sci-Fi trackers are made up of five stations, which are held in position by a carbon fibre space frame (see figure 4.4). The space frame will be locked into position within the solenoid bore by supports at each end of the magnet. Also, through the use of adjustable alignment supports, doweled to the patch panel on the end of the solenoid, the axis of the tracker is aligned to the axis of the experiment. The inner bore of the solenoid will be filled with helium to help reduce multiple scattering. In principle, having just three tracking stations is sufficient, to constrain a circle (helix), needed to provide the transverse momentum ($p_t$) measurements. But, since MICE will use different beam momenta and magnetic field settings, in order to produce a good tracking performance within all input beams and configurations, a requirement of five stations, with varying spacings has been chosen. The baseline spacings, were based on simulation results [65] and are shown in table 4.1.

The carbon fibre stations are designed and constructed so that they offer a rigid structure to support and hold the scintillating fibre planes in position, providing an

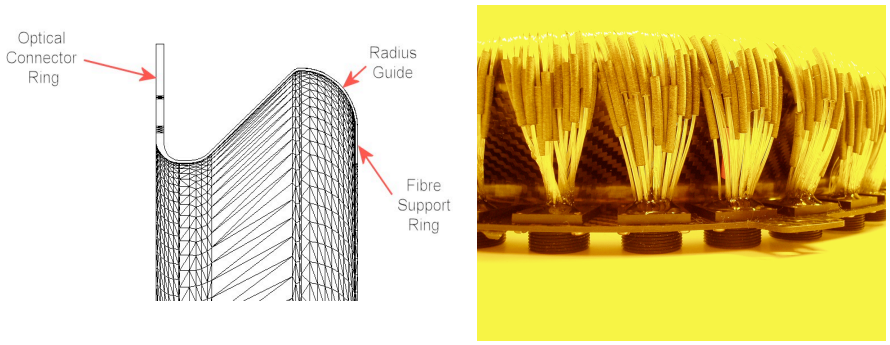


**Figure 4.5:** On the left, is a drawing showing the station body design and on the right, a photograph of a fully developed tracker station showing the fibre run from the doublet layer to the station connector. [9]

active area of 30cm diameter. The station body consists of three main features; a thin flat support ring, where the fibre planes are bonded to the station; a radius guide, which is then used to transmute and feed the fibres round to the optical station connectors, whilst ensuring that the bend radii of the fibres is kept to a minimum; and finally, a flat annulus ring is used, to allow the mounting of the station connectors (see figure 4.5 and 4.6).

### 4.3.3 Optical Connectors and Waveguides

The optical station connectors (30 per station) are required to mate seven 350$\mu$m scintillating fibres to one 1.05mm clear fibre. Each connector has 22 holes of 1.05mm diameter, which is matched to the seven scintillating fibres as shown in figure 4.6. The station connectors use an asymmetric hole pattern, as an initial prototype connector which had a symmetric hole pattern led to errors when threading the fibres into their designated channels (holes).

The clear fibres used, are also round-type and multi-clad, they have a 2.5% tolerance at the 3$\sigma$ level and an attenuation length of 7.6m [12] [64]. They transport the scintillation light from the stations to the readout system, where all the clear fibre runs from each of the five tracker stations have a total length of 4m. The clear fibre waveguide assemblies, which start at the station connectors and terminate at the readout system, are split into two stages, 'internal' and 'external'. The first stage, is the clear fibre runs within the tracker volume, here the fibres coming from six station connectors, of 20-22 channels, form a bundle of 128 clear fibres, which are

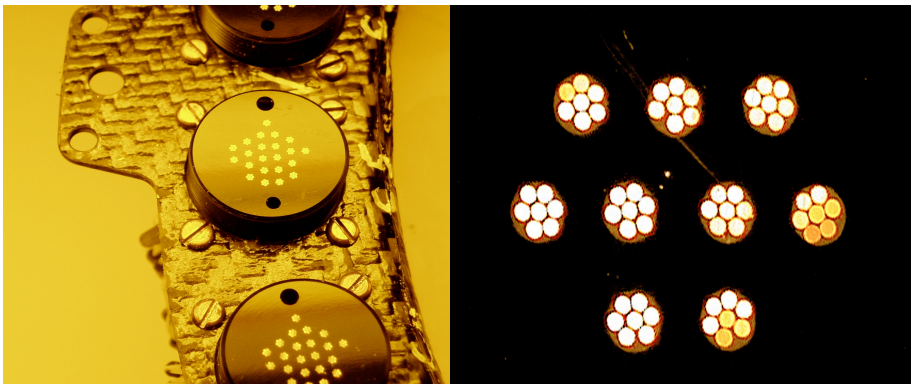

**Figure 4.6:** Photographs showing station connector face, with station body on the left and with LED illumination of fibre channels on the right, clearly indicating the bundles of seven fibres.

then fed into one set of connectors at the patch panel, as shown figure 4.7. The distance, from the patch panel to each station varies, therefore different lengths of 'internal' clear fibres are required, ranging from 1.3m for the station closest to the patch panel, to 2.4m for the furthest station.

The patch panel connectors, as shown in figures 4.7 and 4.9, have 128 fibre holes (channels), offering a $one-to-one$ match to the final 'DØ connectors', needed for the readout system. The patch panel connectors, are built in such a way, that they not only pass the clear fibres out of the tracker volume, but also form a gas seal. There are twenty five patch panel connectors in total, for each tracker (five per station).

The 'external' clear fibre waveguides, which again differ in length (to make the overall total waveguide length of 4m), depending on which station they originate from, transport the light from the 128 channel patch panel connectors, to a final set of connectors. These connectors, called the 'DØ connectors', as they interface to the DØ VLPC readout system [62], developed for the DØ CFT and adopted by MICE. Each DØ connector, contains 128 fibre channels, matching the fibres to channels on the readout cassettes. The DØ connectors used, are specifically built for MICE, such that the only difference from the 'actual' DØ connectors, is that they have the 1.05mm diameter of the MICE clear fibres. However, due to the readout fibres on the VPLC cassettes, which the DØ connector interfaces to having a 0.965mm diameter (DØ design specification), results in an approximate 15% loss of light, but this has already been shown not to be a significant issue in terms of the final light yield performance [12].

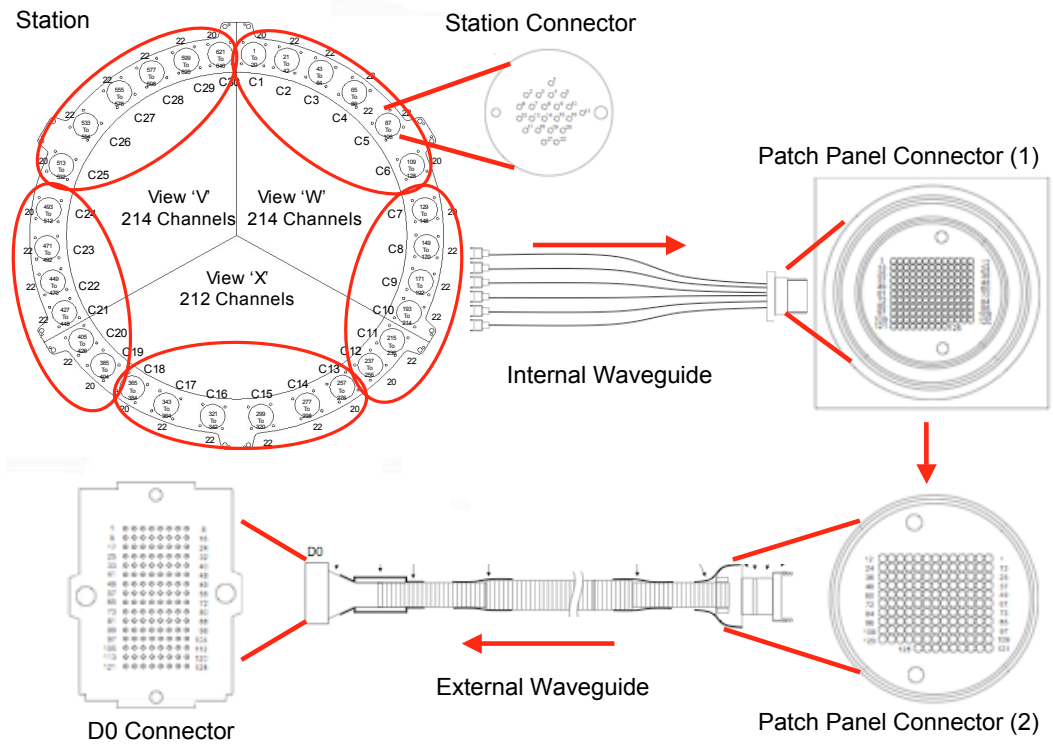


**Figure 4.7:** The waveguide readout chain of the tracker, from the station connectors, to the'DØ connectors' which interface to the optical readout and electronics system.

The method for assembling the fibres and potting them into the connectors is basically the same for both types of fibres (scintillating and clear). First, the fibre (or bundle of fibres) are potted into the appropriate connector hole, the fibres are then glued in the holes, before being trimmed so the connector face can be polished using a diamond fly-cutter. The full assembly process is described in more detail in [9]. With so many fibres, channels, and different connectors required for the tracker readout, much care has been taken during the construction process, with the fibre mapping and routing, so that all fibres/channels are precisely known, from positions on the stations all the way through to the various steps within the VLPC readout chain.

## 4.4 Tracker Readout

The optical readout and electronics system used by MICE for the Sci-Fi trackers, is the same as that used and developed by DØ for the central fibre tracker (CFT) [61]. Visible light photon counters (VLPCs) are used as the photodetector, which

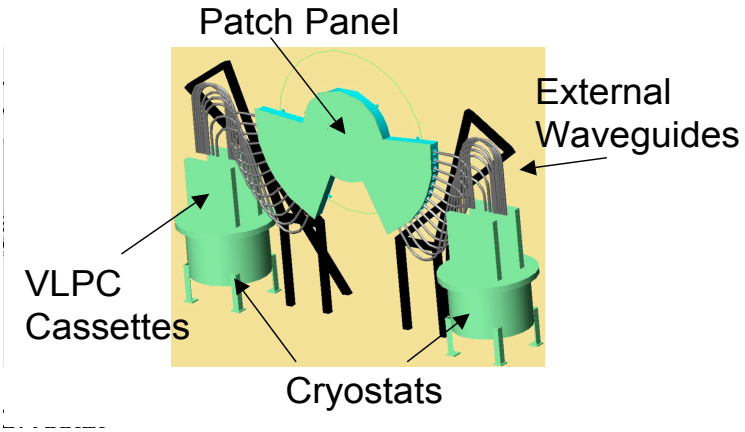


**Figure 4.8:** Schematic of how the readout will be setup in the MICE hall, from the patch panel, to the optical readout and electronics system, via the external waveguides.

require cold operation using a cryogenic system. The VLPCs are packaged into cassettes, which are integrated into the cryogenic assembly. There are two (1,024 channel) cassettes per cryostat, which interface to the clear fibre waveguides, via the DØ connectors. Optical fibres within the cassettes, pipe light from the DØ connector interface to the VLPCs. Finally, the analogue signals from the VLPCs are passed to the electronic readout boards, of which there are two per cassette (four per cryostat). The two electronic readout boards (512 channels each), provide the acquisition, digitisation and readout as well as temperature control and VLPC bias. A schematic showing an overview of the readout system leading from the patch panel is shown in figure 4.8.

### 4.4.1 VLPC system

The VLPC, is a cryogenically operated impurity band silicon-avalanche photo-detector device, a descendant of the solid state photomultiplier [62]. It has undergone various iterations, leading to the HISTE VI design, which is used by DØ and adopted by MICE. Once a photon enters a VLPC, it is converted into an electron-hole pair. An electron avalanche is then created by the hole drifting to the gain layer. The VLPCs are in an 8-element array, in 2x4 element geometry, as shown in figure 4.10, with each pixel in the array having a 1mm diameter. The probability that the photon incident on the VLPC develops into a full electron avalanche, is roughly 80% (the quantum efficiency). The gain of the VLPC used, is roughly 50,000 electrons per converted photon, with an operating temperature of 9K and an operating bias of

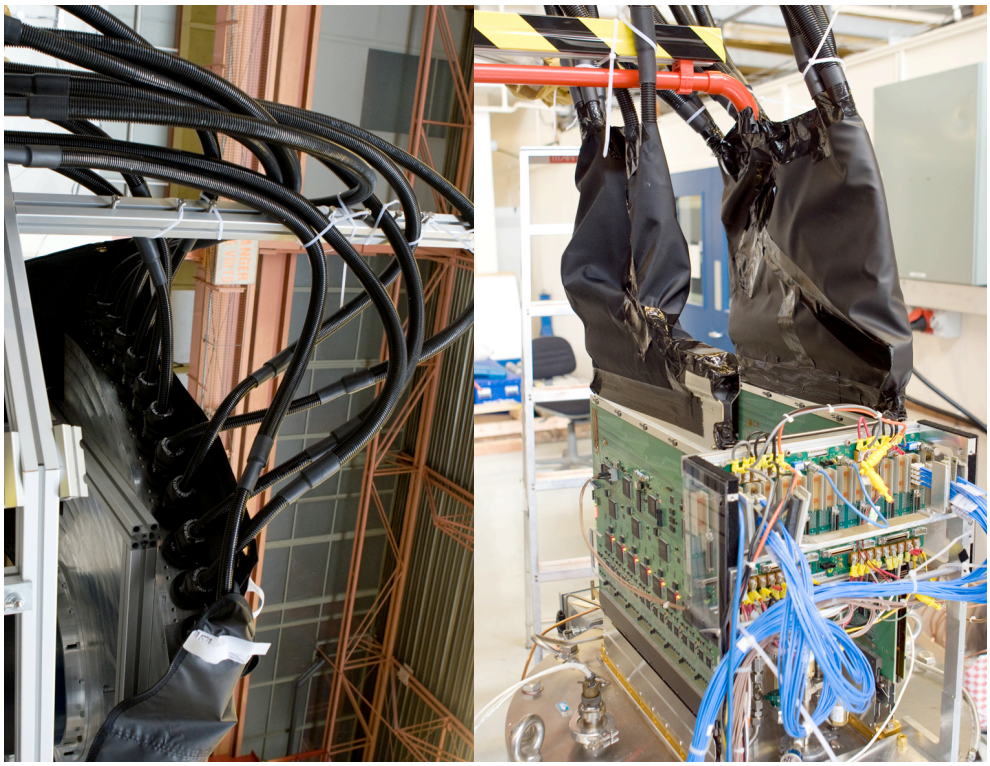

**Figure 4.9:** Photographs of readout chain, showing external waveguides coming from the patch panel (left photograph) and the other end of the external waveguide interfacing to the VLPC cassettes (right photograph).

6-8V. The VLPCs are insensitive to the magnetic fields produced by the spectrometer solenoids. Also, demonstrations have shown that there is no significant effect on the VLPCs from the RF backgrounds expected in MICE [12].

A cryo-system is required as the VLPCs operate at the cryogenic temperature of 9K. A new cryogenic system has been developed and built at Fermilab by DØ with a full prototype commissioned and successfully operated at the prototype tracker beam test, at KEK (chapter 6) and at the cosmic-ray tests at RAL (chapter 7). Four of these cryostats will be used in MICE (two per tracker).

The VLPC cassettes, contain 1024 channels of VLPC readout. They have a "cold end", which sits within the cryostat and a "warm end " outside of the cryostat, which is at room temperature (figure 4.11). Inside the cassette body there are 8 x 128 channel, optical-bundle assemblies, which accept light from the detector waveguides. These optical bundle assemblies, pass through the cassette from the warm end, where they are mated to fibres from the DØ optical connectors, to the 8 assemblies at the cold end, which consist of sixteen VLPCs (eight channels each).

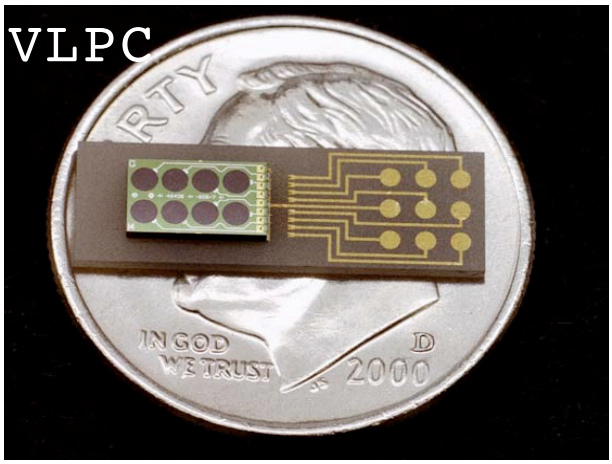


**Figure 4.10:** Photograph of the 8-element VLPC array (shown on top of a coin, to indicate size).

The low level analogue signals from the cold end assemblies (VLPCs), are then passed back via 'kapton flex circuits' to the warm end, where the electronic readout boards are mounted. These flex circuits and the readout boards themselves, are mechanically and electrically connected via a high density connector assembly [9].

### 4.4.2 AFEII Boards and DAQ System

The Analogue Front End (AFEII) electronic boards [12], are used to readout the VLPC system and are mounted onto the VLPC cassettes (1024 channels) at the warm end. There are two AFEII boards per cassette and each board will provide 512 channels of readout. Like the rest of the tracker readout system, they are adopted from the DØ experiment and are required to digitise the input analogue pulses from the VLPCs. The AFEII boards, have been used and tested, for MICE, at the tracker beam test, at KEK in October, 2005 (see chapter 6) and also cosmic test runs [12].

The AFEII board, receives charge signals from the scintillating fibre tracker, via the VLPCs, from which, it provides both digital hit pattern and charge amplitude information, by accepting analogue data from all 512 channels and passing them through discriminators. A bit map of fibres whose charge is above a certain threshold, is produced by the discriminators, which are readout via high-speed serial data links.

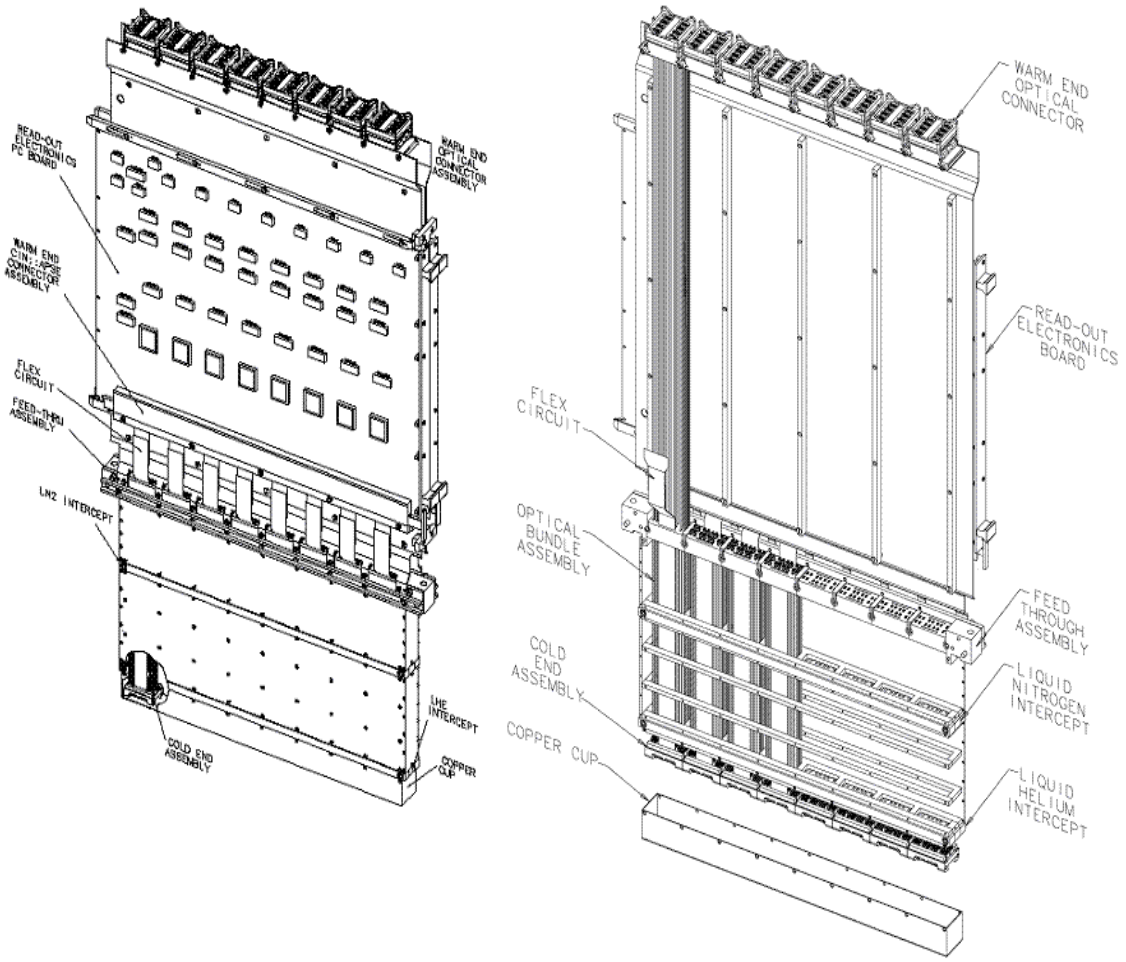


**Figure 4.11:** VLPC cassette, with electronics readout board attached (on the left) and with cassette body removed (on the right). [9]

Each AFEII board, consists of eight 'multi-chip modules' (MCMs), which each serve 64 VLPC channels. Within each MCM, lies two Trigger and Pipeline (TriP) chips, which are mixed signal ASICs (Application Specific Integrated Circuits), providing and storing analogue charge data in 48-level pipelines and also providing the digital discriminator information previously described. The TriP chips are the heart of the AFEII, with the bulk of the components on the AFEII board, only needed for support, configuration and readout of the TriP. The latest upgrade to the chip by DØ includes the addition of timing information as well as the original analogue charge and discriminator data, this chip is called TriP-t with the electronic boards they are implemented on, subsequently called AFEII-t [66].

MICE, will use the AFEII-t boards for the tracker readout, but the extra timing information has been shown to slow the overall digitisation time considerably. The

expected muon trigger rate for MICE is about 600kHz. Therefore, the goal is to acquire, digitise and readout 600 through-going muons every millisecond that the RF cavities are on (once per second), though this may not be possible when total charges and relative times are digitised as well as the discriminator data. Using the DØ implementation for total data readout, only 225 muons/ms would be achievable for MICE. R&D is currently being carried out to try to find different methods of digitisation within the TriP-t chips for MICE, so that the goal of 600 muons/ms can be reached, for further discussion on this see [67] [9].

The readout chain as shown in figure 4.12, shows that after a muon passes through the tracker inducing light pulses within the scintillating fibres, the light is then passed through the waveguides to the VLPCs, where they are amplified. These amplified analogue signals, are then read in as input by the TriP-t chips on the AFEII-t boards and generate three outputs:

- Digital discriminator signal.
- Analogue pulse proportional to the amplitude of the input pulse charge (A-pulse).
- Analogue pulse proportional to the amplitude of the input pulse time relative to the time gate (t-pulse).

The ISIS beam structure will be the time gate used for MICE. The Discriminator data is only digitised for channels where the signal is above a predetermined threshold. The A-pulse and t-pulse are both stored in a 48-level pipeline and are only readout upon receipt of a trigger signal, Level 1 ACCEPT (L1A). In MICE, the L1A trigger will come from a signal within that of the ISIS beam structure combined with other detector signals indicating a through-going muon. Once the TriP-t receives this L1A trigger, it is directed by the AFEII-t board to 'Acquire', 'Digitise' and 'Readout' the three output signals.

For readout of the AFEII-t board on a Linux PC, a VME crate is required with a Bit3 interface, a MIL-STD 1553 interface [68] and a 'VLSB' (VME64 LVDS SERDES Buffer) module [69]. An optical connection is needed between the VME and PCI components of the Bit3, with the other end of the connectors leading to the PCI card in the Linux PC.

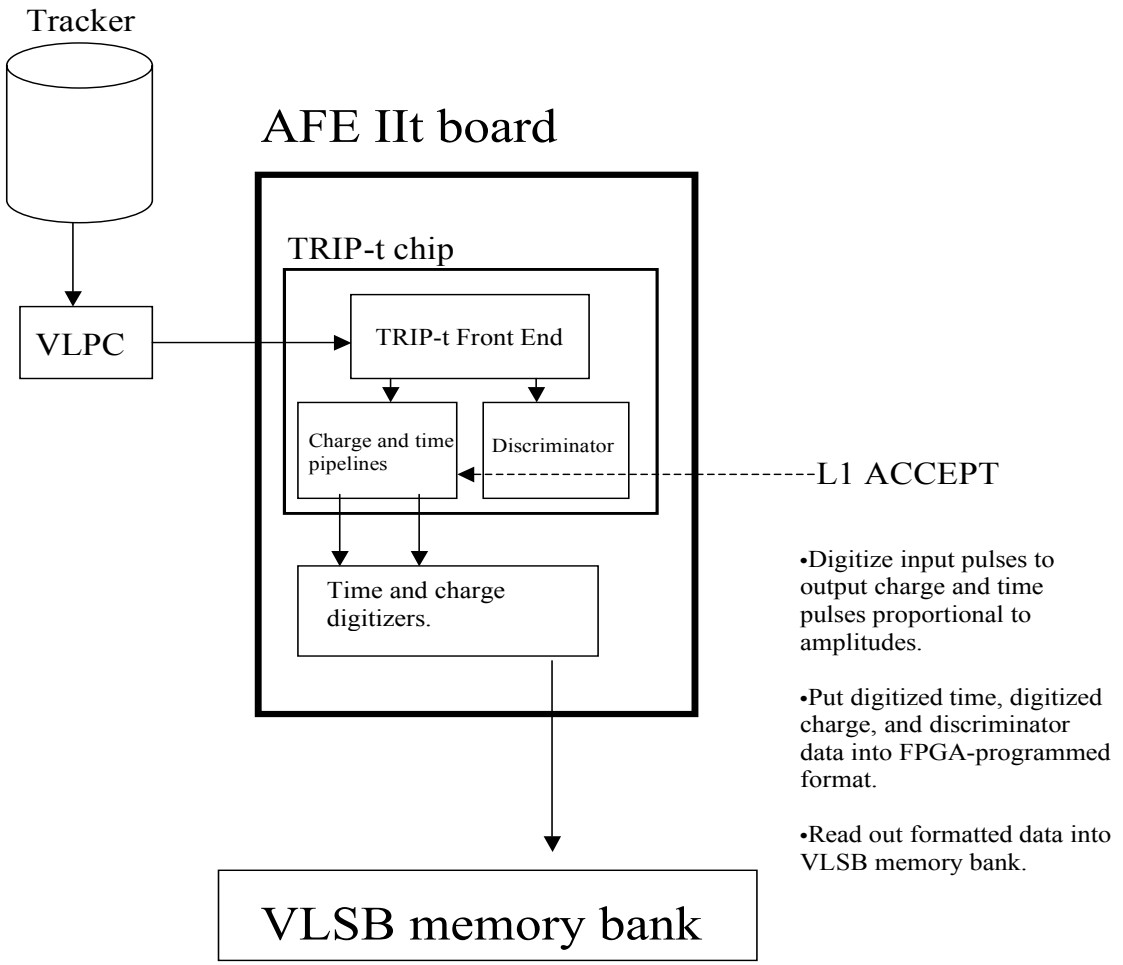


**Figure 4.12:** Schematic diagram of full readout chain. [9]

The Bit3 module is an interface between the VME and PCI, and makes it possible to send VME commands to control all the VME devices (1553 and VLSB) from the PC. The 1553 controller is used to communicate with the AFEII-t board. The majority of commands and initialisation routines are sent to the 1553 controller (via the Bit3 interface). The 1553 sets up the AFEII-t board through a PIC micro-controller, so that it is ready for data taking operation, by controlling the power of the TriP-t chips, FPGA (Field Programmable Gate Array) chips, and other programming chips.

The clock (timing) signals that drive the AFEII-t boards to allow and control triggering and acquisition modes are derived from the ISIS synchrotron signals. The AFEII-t has three modes of operation, idle, acquire or trigger. When set to trigger, the AFEII-t board waits for a suitable signal above a required threshold and au-

tomatically acquires and digitises the data, which is finally sent for readout on the Linux PC. As the board is designed for DØ and therefore synchronised to signals from the Tevatron at Fermilab and not ISIS, modifications are being made to the board and it's firmware to fit into the MICE trigger system, allowing easier readout and greater efficiency.

The final part of the VME architecture is the DØ VLSB [69], it is a VME64 single width 6U module used for retrieving data from the AFEII-t board system for MICE. It is a custom LVDS SERDES (SERialser-DESerialiser) Buffer with 4 LVDS (Low Voltage Differential Signal) input channels. At the heart of the VLSB there is a 'module controller FPGA', which handles the VME and subsequent interfaces, the timing, the diagnostics and also supervises the data flow operation. The VLSB receives and stores the data transmitted by the AFEII-t over the LVDS links via a dedicated link, the data is then streamed to the PC, through the VME interface, for offline reconstruction using G4MICE.

# Chapter 5

# Tracker Reconstruction

## 5.1 Introduction

This chapter describes the software written to reconstruct particle trajectories. Tracking of beam particles in MICE is achieved using the scintillating fibre trackers, which were described in detail in chapter 4. This chapter will briefly explain the simulation chain of the MICE trackers, beginning with a brief recap of the SciFi detector then a description of the simulation and detector response, which is pertinent to the SciFi detectors. Next a description of the various stages of the software reconstructing the particle trajectories will be given along with results showing the simulated tracker performance and how it compares to the specification required of the tracker to produce the level of precision expected from MICE. The main focus of the chapter will be on the space point reconstruction, pattern recognition and Kalman fit as this was the main contribution of the author.

## 5.2 Scintillating Fibre Tracker

The beam particles in MICE are tracked by the two SciFi detectors, which are placed immediately upstream and downstream of the MICE cooling channel. Each tracker has five scintillating fibre stations, where each station is composed of three planar layers of scintillating fibre placed at 120° to one another, therefore enabling better measurement of the hit positions. Each fibre has a diameter of 350$\mu$m chosen as the size required to reduce multiple scattering to an acceptable level. These fibres are

then bundled into groups of seven, which is then taken to be a single channel to be readout. An overview of the dataflow for the tracker software in G4MICE is shown in figure 5.1 for both Monte Carlo and real data.

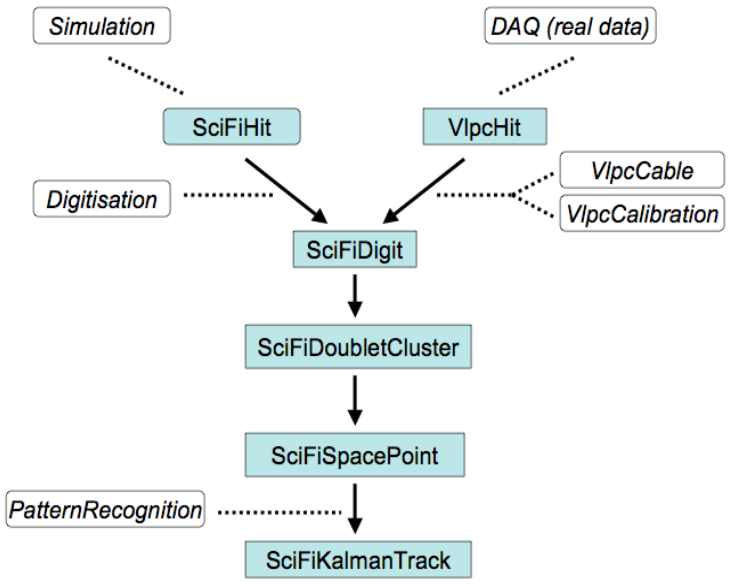


**Figure 5.1:** The dataflow of the tracker software for both Monte Carlo and real data.

## 5.3 Simulation

The Sci-Fi tracking detector is modelled in detail in G4MICE using a series of geometrical objects and materials, ranging from the cylindrical 'mother volume' all the way down to the glue that holds the fibre layers together. The scintillating fibres are modelled individually in GEANT4 as two cylinders, one representing the core, which is inside the other representing the cladding of the fibre. A hit (*SciFiHit*) is recorded whenever a particle passes through any of the fibres. For each "hit" recorded, various information is given, including the time of the hit, position, momentum, energy deposited and particle type. This information including all other detector "hit" details is written to the output file of the G4MICE simulation executable.

## 5.4 Digitisation

The role of the digitisation executable is to simulate the detector response. It uses the stored Monte Carlo hits (*SciFiHits*) and converts them into digits (*SciFiDigits*),

as a simulated response from the VLPC system. For each hit the energy deposited is converted into a number of photoelectrons (see section 6.7.1). This is achieved by using parameterisations to simulate the amount of light produced, such as: photoelectrons converted (see section 6.7.1), the trapping efficiency of the fibre, the propagation along the fibre (mirror efficiency and radiation length) transport to the VLPC (clear fibre radiation length and light transmission at connector interface) and the VLPC response and the readout electronics. All of the processes mentioned have been parameterised based on previous experience taken from the DØ experiment and then tuned to match results obtained from the tracker prototype data [12].

The digits produced from the hits contain both ADC and TDC information*. For a digit to be accepted a certain threshold value for ADC and TDC counts needs to be reached, these threshold values are determined by the readout electronics (see section 4.4). In the case when there is more then one hit on the same channel, the pulse heights are added and the time recorded is that of the earliest signal, therefore giving one digit per channel per event. Finally all digits accepted and stored are written to the digitisation output file and later used for event reconstruction and pattern recognition, which will now be discussed.

## 5.5 Reconstruction Stages

The MICE software framework includes a package called RecPack [70] which is responsible for applying the Kalman filter technique to the track fitting for the SciFi detectors. In this section, a description of the algorithms, which constitute the different stages of the SciFi reconstruction software will be given, with results showing the tracker performance. Also, a brief overview of the theory behind the Kalman filter will be shown along with an explanation of how the SciFi reconstruction software interfaces to this package.

The reconstruction of beam particles in MICE is achieved via a series of stages and algorithms. The algorithms used at each stage in the reconstruction carry out all processes which are required to turn the detector's raw data, which contains information on which fibres were hit and the position of these hits found from the geometry and alignment files into reconstructed tracks. These different stages of

*Only ADC information is produced from AFEII boards (used for KEK test, in chapter 6). MICE will use AFEII-t boards, which will have the added TDC information

the reconstruction and their algorithms will be explained in order in the following subsections. In order to produce a validated track fit in G4MICE, reconstruction tests were written to test the space point reconstruction, pattern recognition and the Kalman fitted tracks. Finally, results from the Kalman fit test (the final stage of the reconstruction) will be presented, showing the tracker performance and comparing it to the specification set out for the tracker.

### 5.5.1 Clusters

Cluster building is the first stage of the reconstruction, it is needed for possible situations where a particle passes between the boundary of two groups of 7 fibres i.e. between two channels, producing light in both, as shown in figure 5.2.

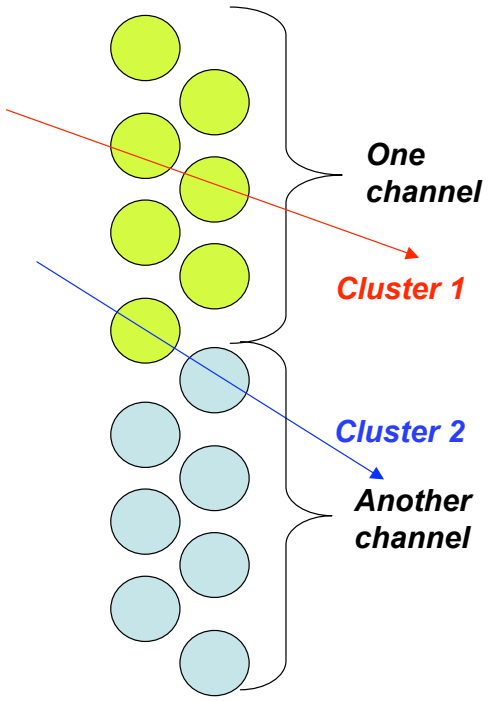


**Figure 5.2:** Visualisation of the clustering technique used in the reconstruction software. Showing the two possible scenarios; isolated clusters (passing through one SciFi channel) and two neighbouring hits combined to form a cluster.

The clustering technique used in G4MICE is as follows. All isolated digitised hits which have a pulse height of >2PE (photoelectrons) will be considered a cluster. In the case where there are two neighbouring hits, they will be considered a cluster as long as the combined pulse height of the two neighbouring hits is >2PE.

The first step of the cluster search, is to loop over all digits and create a list of all the hits with a pulse height >1PE, i.e. half of the required signal of at least 2PE, the chosen cut value [12] which corresponds to ∼3 times the typical width of the pedestal. These hits are then sorted by decreasing light yield, so that the hit with the highest signal is always used first. The next step is to search for any neighbouring hits. Once neighbouring hits have been identified and both have a pulse height >1PE, they are merged together giving a combined signal >2PE and therefore considered as a cluster.

The last stage of the clustering process, involves a loop over all stored clusters and for the case where we have combined two neighbouring hits, the position of the cluster is taken to be the pulse height weighted mean of the two individual hit positions.

### 5.5.2 Space Points

The aim of the space-point algorithm is to define and assign three-dimensional or two-dimensional coordinates (points) to signals detected in the fibre channels of the tracker stations, as shown in figure 5.3, which is an event display of a cosmic ray event, from the recent cosmic ray test at RAL of the final MICE tracker. The space-point algorithm, takes as an input the stored hits/clusters and its output is either a "triplet" or a "duplet", which is a combination of three or two clusters respectively.

After we have all the stored clusters with the required signal, the next stage is to build spacepoints from these clusters. This is achieved by searching through all the clusters to try and find "triplets" which consist of three clusters, one from each of the three views of a single tracker station. By forming a $\chi^2$ value from the internal residual of the reconstructed positions from two clusters and that of a third along with the difference in the measured "hit" time of each of the three clusters, combinations of clusters are stored as space-points, once a cluster has been stored within a space-point it is then 'locked off' from the remaining search for points. After all triplets have been found, any remaining combinations of two clusters from two different views in a single station that are found, are used to create "duplet" space points.

### 5.5.3 Pattern Recognition

The aim of the pattern recognition is to recognise tracks, it takes as input the space point coordinates and its output is tracks, i.e. groups of space points recognised

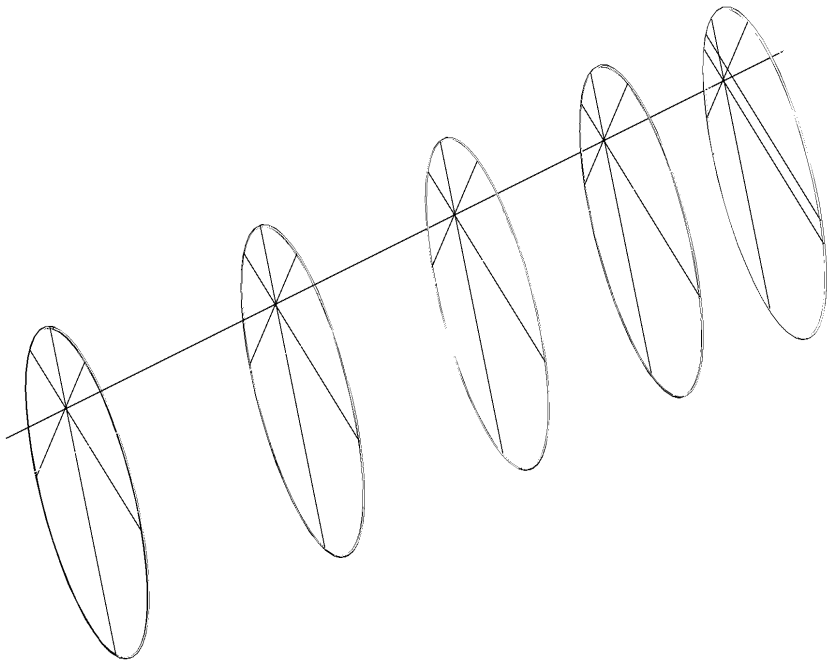

**Figure 5.3:** Visualisation of space points in the MICE tracker from a cosmic ray event.

as belonging to the same track, these track candidates are eventually passed to the Kalman filter for the final stage of the reconstruction, which is the track fit.

In G4MICE the pattern recognition method used can be broken down into two steps. The first step is the seed algorithm, where all space points are assigned to a collection of full-track elements containing a measurement of the position, the direction and momentum of the track. The space points and track elements found by the seed routine are combined to track candidates which are then tested in order to discriminate between good track candidates and combinatorial background. As the MICE tracker only has a few points, the quality of the initial seed to the track fit has a strong effect on the final fit.

The routine starts by determining the radius of the circle in the x-y plane using three space points and from that the transverse momentum $p_t$ is found. Then using the value of $p_t$ and looking in the R$\phi$ vs z plane, the longitudinal momentum $p_z$ is found. The second step then makes predictions as to further points belonging to the track candidate, this is achieved through interpolation or extrapolation of the current track model based on the track candidate found by the seed so far. If additional points are found, they are added to the candidate.

The pattern recognition algorithm in G4MICE is based on three elements [71]:

- A parametric track model, which connects a particle trajectory with a set of track parameters and provides a method of transport, i.e. extrapolation along the trajectory;
- A method to generate track seeds, i.e. rudimentary initial track candidates formed by just three space point hits which serve as a starting point for the track following procedure;
- A quality criterion, which allows distinguishing good track candidates from 'ghosts', so that the latter can be discarded.

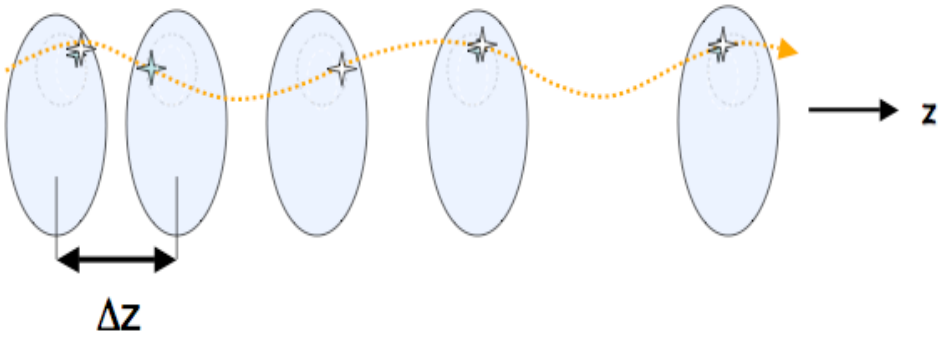


**Figure 5.4:** Helical trajectory of a charged particle in the five station tracker.

The trajectory of a charged particle in a magnetic field is a helix, which can be described by five parameters $(x, y, x', y', 1/p)$. To obtain these parameterisations for tracking in a magnetic field $\vec{B}$, we first need to solve the equations of motion [71] [72]. From the Lorentz force, which is derived from Maxwell's equations and for now, neglecting material effects, in a vacuum, the equation of motion is given as:

$$\frac{d\vec{p}}{dt} = \frac{d(m\gamma\frac{d\vec{x}}{dt})}{dt}$$
$$\frac{d\vec{p}}{dt} = c^2\kappa q\vec{v}(t) \times \vec{B(t)} \tag{5.1}$$

where $m$ is the rest mass and $\vec{x}$ is the position (space point) of the particle, $c$ is the velocity of light, $q$ is the charge of the particle, $t$ is the time in the laboratory frame and $\kappa$ is a proportionality factor (dependent on unit choice). We can then express the equation of motion (5.1) in terms of only the geometrical quantities:

$$\frac{d^2\vec{x}}{ds^2} = \left(\frac{\kappa q}{P}\right)\left(\frac{d\vec{x}}{ds}\right) \times \vec{B}(s) \tag{5.2}$$

where $s(t)$ is the path length along the trajectory, with $ds/dt = v$ and the momentum of the particle $P = m\gamma\beta c$ and since magnetic fields only change the direction of charge particles, both $\gamma = (1-\beta^2)^{\frac{1}{2}}$ and $\beta = \frac{v}{c}$ are constant [71].

In a homogenous magnetic field, which is parallel to the z axis (i.e. along the beam) $\vec{B} = (0, 0, B_z)$, the equations of motion (5.2) can then be expressed as three differential equations:

$$\frac{d^2x}{ds^2} = \left(\frac{\kappa q}{P}\right)\left(\frac{dy}{ds}\right)B, \qquad \frac{d^2y}{ds^2} = -\left(\frac{\kappa q}{P}\right)\left(\frac{dx}{ds}\right)B, \qquad \frac{d^2z}{ds^2} = 0 \tag{5.3}$$

solving these simultaneously, gives a helix with an axis parallel to z, where $x$, $y$ and $z$ are expressed as functions of the path length $s$:

$$\begin{aligned} x(s) &= x_1 + R\left[\cos\left(\Phi_0 + \frac{hs\cos\lambda}{R}\right) - \cos\Phi_0\right] \\ y(s) &= y_1 + R\left[\sin\left(\Phi_0 + \frac{hs\cos\lambda}{R}\right) - \sin\Phi_0\right] \\ z(s) &= z_1 + s\sin\lambda \end{aligned} \tag{5.4}$$

where we have the following five parameters which are visualised in figure 5.5:

- $x_1$, $y_1$ and $z_1$ is the starting point (i.e. first space point) at s = 0
- $\lambda$, is the 'dip' angle, where ($\frac{\pi}{2} \leq \lambda \leq \frac{\pi}{2}$)
- $R$, is the radius of the helix
- $h$, is the sense of rotation of the helix in the xy-plane, i.e. $h = -sign(qB_z) = \pm 1 (= sign(d\phi/ds))$
- $\Phi_0$, is the azimuth angle of the starting point (in cylindrical coordinates) with respect to the helix axis and $\phi = \Phi + \frac{h\pi}{2}$ ($\phi$ is the track direction)

### Track finding algorithm

The pattern recognition algorithm takes as input space points with dimensional coordinates $(x_i, y_i, z_i)$, which are subsequently put in order of increasing z position. These space points, are assigned to possible track candidates, which is achieved by searching for a collection of three space points for which the parameters describing a helix can be determined analytically. The pattern recognition algorithm doesn't directly search for helix candidates, but rather builds links between space points in the different tracker stations. This information is then used to measure the momentum of the particle.

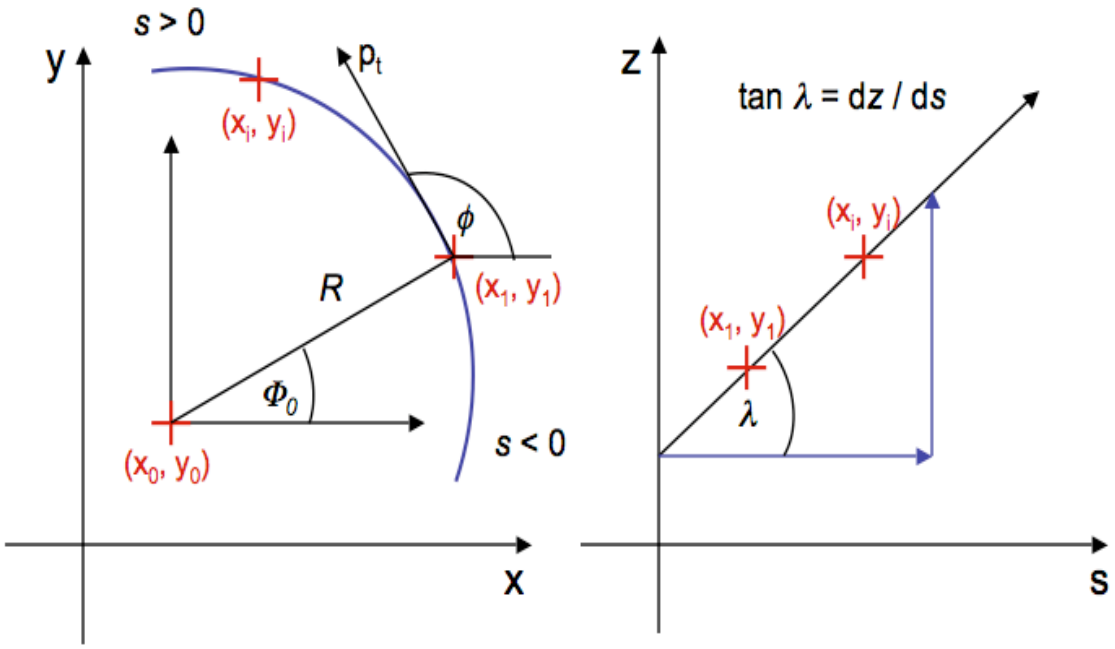


**Figure 5.5:** Helix parameterisations

The fitting procedure starts by producing a circular fit in the xy-plane, which gives the centre of the fitted circle $(x_0, y_0)$ and the curvature $\rho = \frac{1}{R}$ where R is the radius of the fitted circle [73].

The method used to do this uses the equation of a circle passing through the three space points $(x_i, y_i)$, where $i$ =1, 2, 3. From these three points a triangle is formed and a 'circumcircle' is found. The circumcircle is the unique circle that passes through the three vertices (points) of the triangle, where the equation of the circle is given by 5.5, which is found from a geometrical construction [74]:

$$\begin{vmatrix} x^2+y^2 & x & y & 1 \\ x_1^2+y_1^2 & x_1 & y_1 & 1 \\ x_2^2+y_2^2 & x_2 & y_2 & 1 \\ x_3^2+y_3^2 & x_3 & y_3 & 1 \end{vmatrix} = 0 \tag{5.5}$$

From this equation, the centre ($x_0$, $y_0$) and the radius (R) of the circle formed by the triangle can be found by assigning coefficients of a quadratic curve [75]:

$$ax^2 + cy^2 + dx + ey + f = 0 \tag{5.6}$$

where a = c and b = 0 (no x y cross term). Therefore, completing the square of equation 5.6 gives 5.7:

$$a\left(x + \frac{d}{2a}\right)^2 + a\left(y + \frac{e}{2a}\right)^2 + f - \frac{d^2+e^2}{4a} = 0 \tag{5.7}$$

which with a circle of the form 5.8:

$$(x - x_0)^2 + (y - y_0)^2 = R^2 \tag{5.8}$$

identifies the centre and the radius of the circle in equations 5.9, 5.10 and 5.11 to be:

$$x_0 = -\frac{d}{2a} \tag{5.9}$$

$$y_0 = -\frac{e}{2a} \tag{5.10}$$

$$R = \sqrt{\frac{d^2+e^2}{4a^2} - \frac{f}{a}} \tag{5.11}$$

where the parameters of the equation a, d, e and f are given by 5.12, 5.13, 5.14 and 5.15 respectively:

$$a = \begin{vmatrix} x_1 & y_1 & 1 \\ x_2 & y_2 & 1 \\ x_3 & y_3 & 1 \end{vmatrix} \tag{5.12}$$

$$d = -\begin{vmatrix} x_1^2 + y_1^2 & y_1 & 1 \\ x_2^2 + y_2^2 & y_2 & 1 \\ x_3^2 + y_3^2 & y_3 & 1 \end{vmatrix} \tag{5.13}$$

$$e = \begin{vmatrix} x_1^2 + y_1^2 & x_1 & 1 \\ x_2^2 + y_2^2 & x_2 & 1 \\ x_3^2 + y_3^2 & x_3 & 1 \end{vmatrix} \tag{5.14}$$

$$f = -\begin{vmatrix} x_1^2 + y_1^2 & x_1 & y_1 \\ x_2^2 + y_2^2 & x_2 & y_2 \\ x_3^2 + y_3^2 & x_3 & y_3 \end{vmatrix} \tag{5.15}$$

Now, the centre of the circle ( $x_0$, $y_0$) and the radius of the circlular fit are known, the transverse momentum of the particle ($p_t$) given in GeV/c is determined using:

$$p_t = q\kappa BR \tag{5.16}$$

where q is the charge of the particle, $\kappa$ is proportional to the velocity of light and is defined as $\sim$0.3(GeV/c)$T^{-1}m^{-1}$ [72], B is the magnetic field in Tesla (T) and R is the radius of the fitted circle in metres (m).

The phase of the helix is given by:

$$\Phi_0 = arctan\left(\frac{y_1 - y_0}{x_1 - x_0}\right) \tag{5.17}$$

Using equation 5.17 we can determine $\phi$, for each of the three space points $\phi_1$, $\phi_2$ and $\phi_3$. Using this information along with $p_t$, the transverse momentum coordinates $p_x$ and $p_y$, can then be determined as follows:

$$\begin{aligned} p_x &= p_t cos\phi_1 \\ p_y &= -p_t sin\phi_1 \end{aligned} \tag{5.18}$$

The next step in the algorithm is to calculate $\Delta\phi$ between the three points, whilst testing that there are no $2\pi$ ambiguities. After this, a consistency test checks the $\frac{\Delta\phi}{\Delta z}$ ratios between the points to check their colinearity, where $\Delta z$ is the distance

between stations. If these tests are passed, the longitudinal momentum $p_z$ is then calculated by:

$$p_z = p_t tan\lambda \tag{5.19}$$

The momentum resolutions $\sigma_{px}$, $\sigma_{py}$ and $\sigma_{pz}$, along with the spatial resolutions $\sigma_x$ and $\sigma_y$ can be estimated with a detailed knowledge of the tracker and are required for the initial conditions of the covariance matrix of the Kalman fit (see section 5.5.4). The spatial resolutions, are limited by the finite thickness of the scintillating fibres and therefore dominated by the channel pitch and given to a good approximation to be:

$$\sigma_x \simeq \frac{channelpitch}{\sqrt{12}} \tag{5.20}$$

The transverse momentum shown in 5.16 is proportional to the radius of the fit where $\mathrm{R} = \sqrt{\mathrm{x}^2 + \mathrm{y}^2}$ giving an approximation of $\sigma_R$ to be:

$$\begin{aligned} \sigma_R^2 &\sim \left(\frac{dR}{dx}\right)^2 \sigma_x^2 + \left(\frac{dR}{dy}\right)^2 \sigma_y^2 \\ &\sim \frac{x^2\sigma_x^2 + y^2\sigma_y^2}{R^2} \end{aligned} \tag{5.21}$$

therefore the transverse momentum resolution is a function only of the spatial resolution and when considering ($\sigma_x \simeq \sigma_y$), can be estimated using the following:

$$\sigma_{pt} \simeq \kappa B \sigma_x \tag{5.22}$$

where $\kappa$ is the proportionality factor and B is the magnetic field as shown in equation 5.16. The transverse momentum coordinate resolutions $\sigma_{px}$ and $\sigma_{py}$ are subsequently estimated to be:

$$\sigma_{px} \simeq \frac{\sigma_{pt}}{\sqrt{2}} \tag{5.23}$$

$$\sigma_{py} \simeq \frac{\sigma_{pt}}{\sqrt{2}} \tag{5.24}$$

The longitudinal momentum measurement is known to be highly correlated to the longitudinal and transverse momentum of the tracks themselves, therefore an estimation of the longitudinal momentum resolution is simply given to be:

$$\sigma_{pz} \simeq p_z \left( \frac{\sigma_{pt}}{p_t} \right) \tag{5.25}$$

Once the track parameters have been derived for a collection of three space points, if the total momentum is within a plausible range and the reconstructed time of the three points are consistent with a particle travelling downstream, the combination of three points is kept for consideration as a track candidate.

Following this, an extrapolation is made using the track parameters to the other two remaining stations, such that if a space point is found within a small road width, the extra point(s) are added to the track candidate. The combinations of 5, 4 or 3 point tracks are then passed to the Kalman filter track fit where the combination with the smallest $\chi^2$ per degree of freedom is kept. All points, which are used in stored tracks are then removed so that they cannot be used in subsequent track searches. The whole pattern recognition process is then repeated until eventually all points are used or no more tracks can be found.

### 5.5.4 Kalman Fitting

The role of the G4MICE tracker reconstruction software described is to select possible track candidates to be passed to an external software package called RecPack [70] which using the Kalman filtering technique [76], will provide track fitting and a calculation of $\chi^2$ values. A brief overview of the principle of the Kalman filter will be described, followed by a brief description of how the G4MICE software interfaces to and makes use of the RecPack package.

A track in space can be described by a five-dimensional 'state vector':

$$\mathbf{x} = (x, y, \frac{dx}{dz}, \frac{dy}{dz}, \frac{1}{p}) \tag{5.26}$$

where p is the momentum and x, y and z are its spatial coordinates at each measurement point along the trajectory, defined by its position in z. The Kalman filter

technique is used as an optimal estimator of the state vector (track) of a linear dynamic system, as it minimises the mean square estimation error.

By using a system of linear equations the evolution of the state vector can be described as:

$$\mathbf{x}(z_k) \equiv \mathbf{x}_k = \mathbf{F}_{k-1}\mathbf{x}_{k-1} + \omega_{k-1} \tag{5.27}$$

which uses the previous state vector measurement $\mathbf{x}_{k-1}$ to define the change to the new state vector, along with $\mathbf{F}_{k-1}$ which represents the track propagator from measurement k-1 to the current measurement k. The variable $\omega_{k-1}$ describes the random noise processes of the system, such as multiple scattering and systematic effects such as energy loss, which is required when tracking particles through dense media as these kinds of physical processes can influence the final trajectory of the particle.

The actual measurements $\mathbf{m}_k$ of the detector (tracker) at measurement point k, are functions of the state vector $\mathbf{x}_k$, which is not observed directly:

$$\mathbf{m}_k = \mathbf{H}_k\mathbf{x}_k + \epsilon_k \tag{5.28}$$

where $\mathbf{H}_k$ describes the relationship between the measured quantities and the state vector and $\epsilon_k$ is the noise coming from the measurement.

Three distinct operations are performed by the Kalman filter to determine the evolution of the state vector:

- **Prediction:** An estimation of the state vector at a future measurement point.
- **Filtering:** An estimation of the current state vector based on all previous measurements.
- **Smoothing:** An estimation of the state vector at a previous measurement is re-evaluated using new information from all the new measurements up to the previous measurement.

Before the Kalman filter is used for the SciFi track fit, it is provided with geometry information by the G4MICE reconstruction software. Here the experimental setup from the configuration and geometry files in G4MICE provides the Kalman filter with all the volume and surfaces required with well defined position and size information. It is also here where the magnetic field information and material properties (radiation length, energy loss) are provided.

Once this information is accessible, the Kalman track fit proceeds using the three distinct operations mentioned. The prediction of the state vector at future measurement points is made from the current state vector which initially is given by the first space point of the track candidates coming from the pattern recognition, providing the seed track parameters and their covariance matrix.

Through each preceding step in the Kalman filter, the state vector and its covariance matrix are constantly updated using incorporated measurement information. The residuals (prediction - measurement) are updated at every step along with the covariance matrix of the residuals themselves, so a $\chi^2$ measurement can also be evaluated and updated throughout the whole track fit process.

## 5.6 SciFi Specification

To demonstrate that the MICE cooling channel can provide the cooling performance required for a Neutrino Factory an absolute emittance measurement accuracy of 0.1% is necessary [47]. To achieve this two requirements must be fulfilled, firstly the statistical errors on the measurements must be smaller then 0.1%, which will be achieved through obtaining sufficient statistics and secondly that any systematic offset must be removed.

A description of the technique used to remove the offset in the emittance calculation has been shown elsewhere [55], but the key element of the technique, is the dependence on having a well calibrated detector system. The tracker(s) will produce the majority of the phase space measurements, for the emittance measurement, therefore constraints have been put on the tracker resolution, so that not only are the measurement errors coming from the device well known, but that they are also within tolerances set out in the MICE proposal [47] and discussed in detail here [55]. An overview of the tracker specification will now be shown, with a brief explanation of the argument behind it.

If we have a true phase space coordinate $q_i^{true}$, where $i$ is the $i^{th}$ phase space variable (i.e. either x, y, px, py, E or t)[†] we can write the definition of normalised RMS emittance in the form of equations 3.12 and 3.13 to be:

$$\varepsilon_{rms} = k\sqrt{\prod_i \sigma^2(q_i^{true})} = k\prod_i \sigma(q_i^{true}) \tag{5.29}$$

where the constant k, is the normalisation factor, $\frac{1}{m_\mu c}$. In equation 5.29, to first approximation, it is assumed there are no correlations between the errors on the phase space variables and that $\sigma(q_i^{true})$ is the variance of the true phase space coordinate. In this approximation the RMS spread of the measured phase space variable $\sigma(q_i^{meas})$ can be shown to be:

$$\sigma(q_i^{meas}) = \sqrt{\sigma^2(q_i^{true}) + \sigma^2(q_i^{res})} \tag{5.30}$$

which is the addition in quadrature, of the variance of the true phase space variable ($q_i^{true}$) and the resolution of the phase space variable ($q_i^{res}$).

This uncertainty in the measurement errors introduces a bias in the emittance measurement. Therefore, in order to estimate this bias assuming $\sigma(q_i^{true}) \gg \sigma(q_i^{res})$ we can use a binomial expansion to give:

$$\sigma(q_i^{meas}) \simeq \sigma(q_i^{true})\left[1 + \frac{\sigma^2(q_i^{res})}{2\sigma^2(q_i^{true})}\right] \tag{5.31}$$

when estimating that the measurement errors can be understood with a relative accuracy of 10%, the requirement of an absolute emittance measurement precision of 0.1% leads to a requirement of a 1% error in each of the phase space variables [55], therefore using equation 5.31:

$$\left(1 + \frac{\sigma^2(q_i^{res})}{2\sigma^2(q_i^{true})}\right) < 1.01 \tag{5.32}$$

leads to the specification on the measurement accuracy for each phase space variable to be:

[†]where t comes from TOF system, not the tracker.

$$\frac{\sigma(q_i^{res})}{\sigma(q_i^{true})} < 14\% \tag{5.33}$$

As other unforseen sources of errors may arise, a figure of merit has been chosen, such that the RMS resolution $\sigma(q_i^{res})$ in each phase space variable must be less than 10% of the RMS true width $\sigma(q_i^{true})$ of the same variable at equlibrium emittance.

## 5.7 SciFi Performance

A Monte Carlo simulation of the MICE stage VI (see figure 3.12) setup has been performed to test the performance of the tracker using the tracker reconstruction software described, showing measurement resolutions and how they compare to the tracker specification.

The baseline MICE stage VI configuration has been used with all experimental apparatus, including the full cooling channel with all volumes and material descriptions, along with all measured tracker geometry information and parameters such as the light yield (now confirmed in a recent cosmic ray test, see chapter 7). A matched 2.5 $\pi$ mm transverse emittance beam has been used, as this is considered to be (or close to) the equilibrium emittance for MICE, with $\beta_\perp$ of 420mm, $\alpha$ of 0 and a mean momentum of 200MeV/c. The following analysis (and that in chapter 6) has been produced using PAW (Physics Analysis Workstation) [77].

The $\chi^2$ per degree of freedom distribution of the Kalman track fit is shown in figure 5.6. The efficiency of the track fit is summarised in table 5.1 where the track fit efficiency is calculated to be the ratio of all successfully reconstructed 5, 4 and 3 point tracks (i.e. 3+) and the number of simulated events. The error given, is the estimated standard deviation of the efficiency, coming from the standard error formula of a random sample from the event population [78]. The efficiency, is also given for a subset of successfully fitted tracks in the cases where; 4+ point tracks are found and also just 5 point tracks.

As described in section 5.6, the performance of the tracker is determined by the accuracy to which the reconstructed momentum and position of the particles in MICE can be measured. If the RMS width of the phase space variables resolution (reconstructed - truth) can be found to be $< 10\%$ than that of the same variables

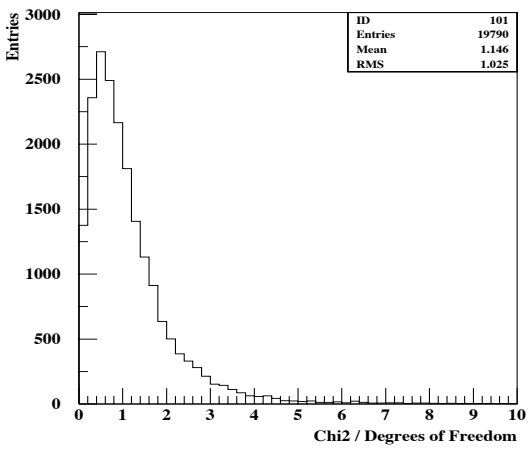


**Figure 5.6:** $\chi^2$ per degree of freedom distribution from the Kalman track fit.

| Number of points in track | Track fit efficiency (%) |
|---|---|
| 5 | 95.38 ± 0.21 |
| 4+ | 98.86 ± 0.11 |
| 3+ | 99.95 ± 0.02 |

**Table 5.1:** Efficiency of track fit for different requirements on the number of points.

RMS true width at equilibrium emittance, then the bias introduced to the emittance measurement from the systematic error can be removed.

Therefore, the simulated true distribution and resolution for all five phase space variables measured by the tracker (x, y, $p_x$, $p_y$, $p_z$) for both the upstream and downstream trackers are shown in figures 5.7 and 5.8. The track fit results are summarised in table 5.2, where the last two columns compare the ratios of RMS resolution and RMS spread of the same variable at equilibrium emittance, for the current track fit results and also old results, presented in the tracker validation report [12], which used a near identical simulated beam and setup but different reconstruction algorithms.

The comparison of the performance has shown that the new reconstruction algorithms and track fit, has improved all phase space variable measurements. All the transverse variables (x, y, $p_x$, $p_y$) are found to be measured well within the specification, with the longitudinal momentum $p_z$ just failing the requirement but still is an improvement from the old reconstruction. To improve this, further studies could be

made, for example providing the track fit with a better estimation of $\sigma_{pz}$ compared to that given in equation 5.25, which could be considered to be over simplified as it does not take into consideration the error on the measurement of the angle used to calculate $p_z$.

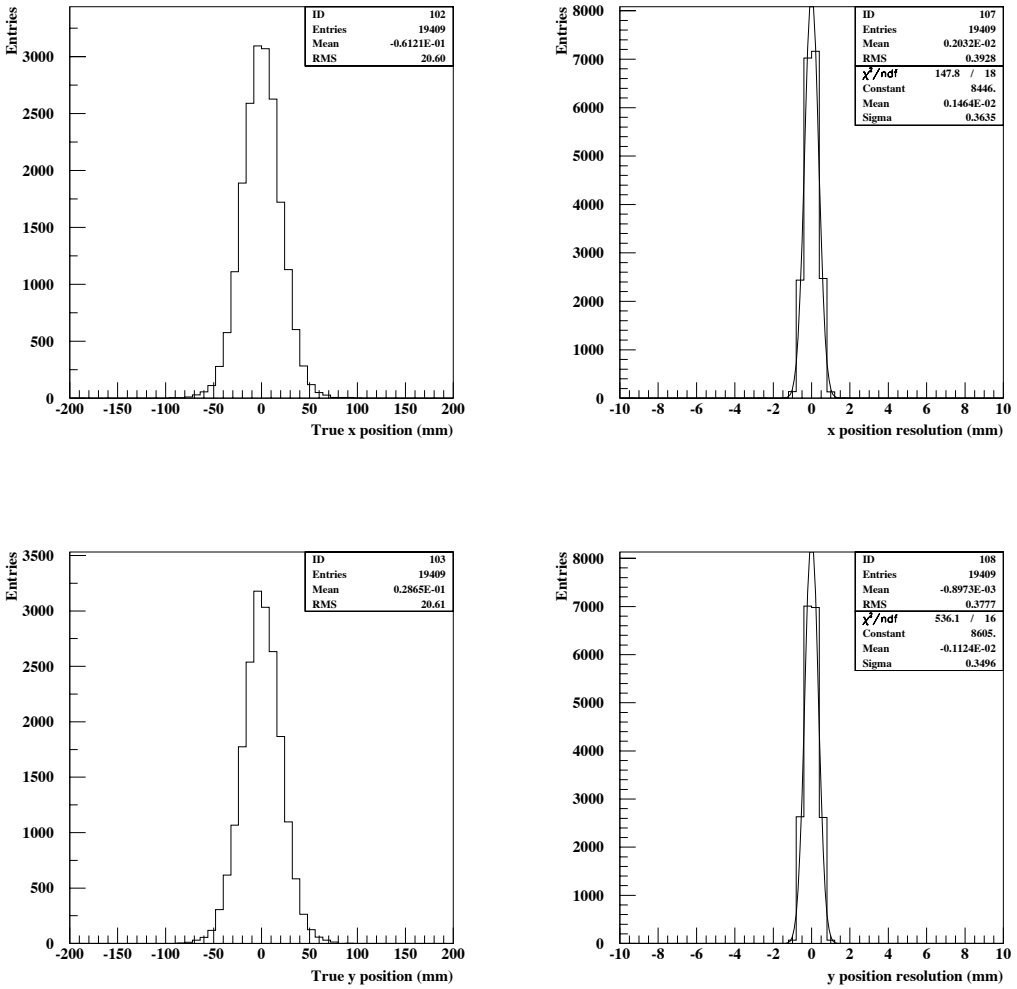


**Figure 5.7:** Monte Carlo true x position distribution (top left), with x position resolution (reconstructed - true) distribution (top right) and Monte Carlo true y position distribution (bottom left), with y position resolution (reconstructed - true) distribution (bottom right)

## 5.8 Summary

In this chapter the G4MICE tracker reconstruction has been described, mainly focusing on the work of the author, which was the space point, pattern recognition

and track fit reconstruction. A Monte Carlo simulation has been used to show the performance of the reconstruction software and compared these results, to results produced by an old version, used for the MICE tracker validation. The results given, show that the new tracker reconstruction has improved the phase space variable measurements since the tracker validation and shown that the transverse variables needed for the transverse emittance measurement are all well within specification.

| | RMS (true) | $\sigma_{res}$ | RMS (res) | $\frac{RMS_{res}}{RMS_{true}}$ (%) | Old $\frac{RMS_{res}}{RMS_{true}}$ (%) |
|---|---|---|---|---|---|
| x (mm) | 20.60 | 0.364 | 0.393 | 1.91 | 2.58 |
| y (mm) | 20.61 | 0.350 | 0.378 | 1.83 | 2.10 |
| px (MeV/c) | 20.35 | 0.910 | 1.037 | 5.10 | 11.5 |
| py (MeV/c) | 20.23 | 0.913 | 1.030 | 5.09 | 8.53 |
| pz (MeV/c) | 27.71 | 2.187 | 4.124 | 14.9 | 15.9 |

**Table 5.2:** Summary of tracker performance, including the ratios: RMS(resolution)/RMS(true), required to check if each phase space variable measurement is within specification. The results found are also compared to previous results from the tracker validation [12]

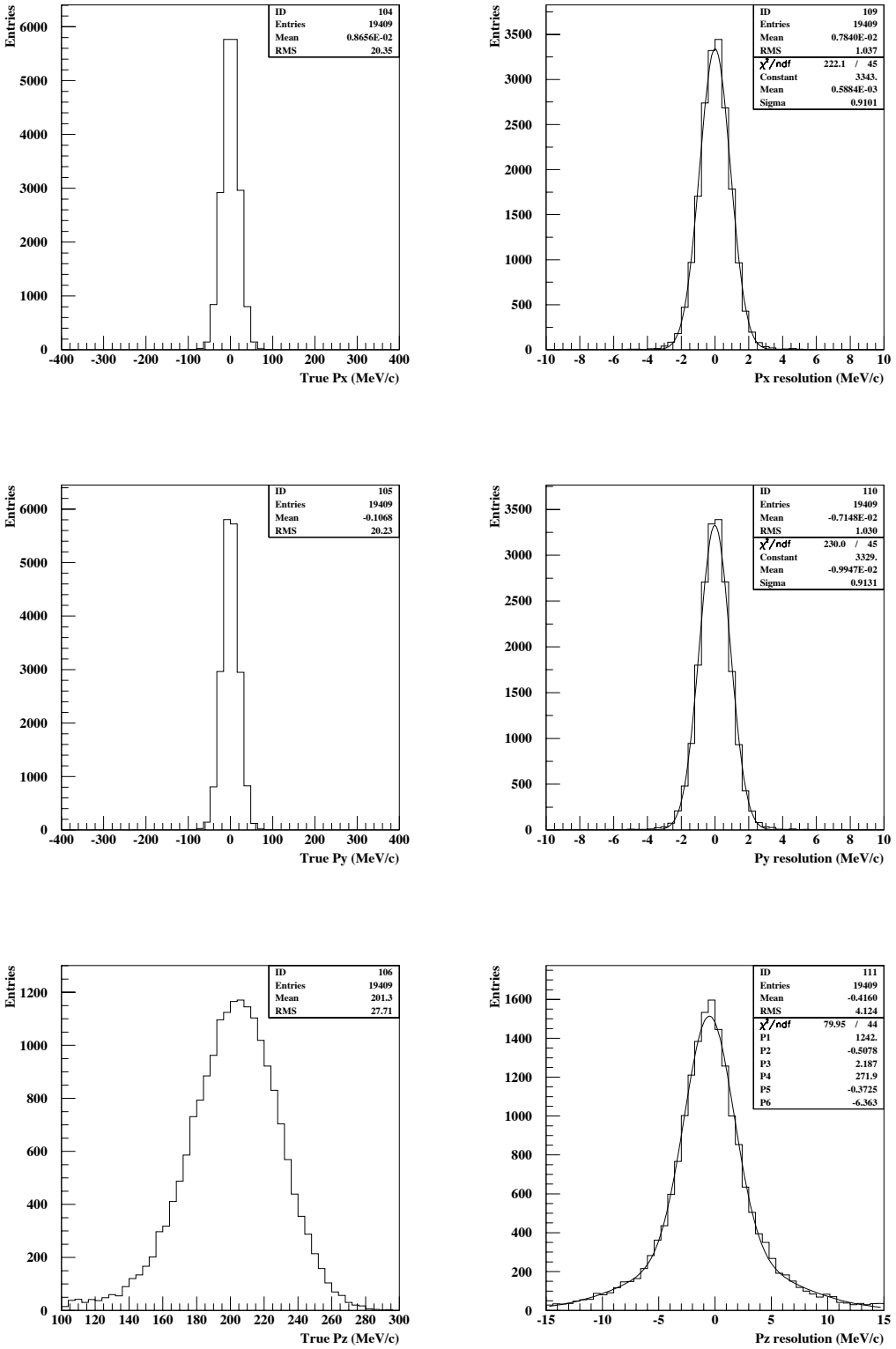


**Figure 5.8:** Monte Carlo true distributions (left), with resolution (reconstructed - true) distributions (right), for $p_x$ (top), $p_y$ (middle) and $p_z$ (bottom)

# Chapter 6

# Tracker Prototype Performance Test

## 6.1 Introduction

In October 2005, a four station prototype of the MICE scintillating fibre tracker was examined in a beam test performed in a one week period at the KEK laboratory in Tsukuba, Japan using the KEK-PS $\pi 2$ beamline. The aim of the test was to measure the light yield of the prototype in a beam similar to one that will be used for MICE, whilst also checking the tracker construction, the alignment and finally to demonstrate tracking in a 1-tesla solenoidal magnetic field.

This chapter presents the analysis of the beam test, which was achieved using the G4MICE software, including the tracker reconstruction algorithms described in the previous chapter. The analysis had complications due to some limiting factors such as fewer tracking planes then are in the final detector and a magnetic field that was a quarter of that to be used in MICE. Also, the simulated beam has not been tuned to match exactly that of the real beam produced by the $\pi 2$ beamline, as the real beam was not characterised due to a lack of dedicated beamline instrumentation. All these factors have been considered and have had an impact on the overall efficiency of the tracking but not on the evaluation of the performance of the prototype, such that the aims of the test have still been achieved.

## 6.2 Experimental Setup

### 6.2.1 Tracker Prototype

The four station prototype tracker was constructed using three 'old' stations called A, B and C used in a previous cosmic ray test [12] and a new fourth station called D, which was constructed using newly designed station connectors described in section 4.3.3, which removed a symmetry issue which led to errors when threading the fibre bundles into the correct channel holes. Also, a new extra interface, called patch panel connectors, which are required for the final MICE trackers were used on station D's clear fibre readout. The clear fibres that were used for the three old stations passed straight from the station connectors, to the VLPC optical readout and electronics system.

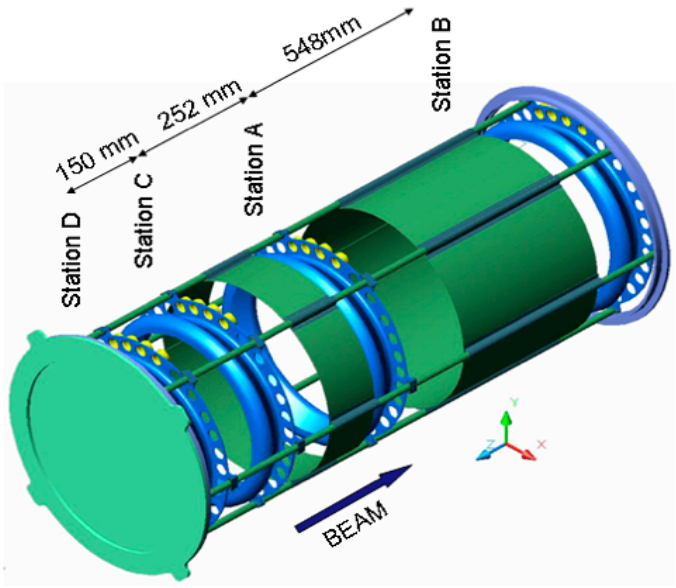


**Figure 6.1:** Schematic drawing of the four station tracker prototype used at KEK, showing the four stations, the different spacings between them and the coordinate system used at KEK.

Station D and station B each had three fibre doublet fibre layers (views) V, X and W as shown in figure 4.3, whereas stations A and C only had two doublet fibre layers V, X and X, W respectively, as a consequence of limited materials when the stations were constructed. The fibre pitch (distance between neighbouring fibres in one singlet layer) was 420$\mu$m. The scintillating fibres used in the prototype are the same 350$\mu$m diameter Kuraray multiclad doped polystyrene fibres that are used for the final MICE trackers. The primary dopant (pT) was at 1% concentration (by

weight) for all scintillating fibres, with different secondary dopant (3HF) concentrations per view. This was a consequence of using the three old stations which were originally used to study light yield as a function of 3HF and the new station (D) was constructed using spare fibre doublet layers. The prototype tracker along with the station spacings is shown in figure 6.1 and the 3HF concentrations per plane (view) are given in table 6.1.

| | Position | X View | V View | W View |
|---|---|---|---|---|
| Station D | -475mm | 2,500 ppm | 2,500 ppm | 5,000 ppm |
| Station C | -325mm | mixture | N/A | 5,000 ppm |
| Station A | -73mm | 5,000 ppm | 5,000 ppm | N/A |
| Station B | 475mm | 5,000 ppm | 2,500 ppm | 3,500 ppm |

**Table 6.1:** Station positions in z (here z=0 is defined as centre of the tracker) within 1m long tracker prototype, along with 3HF concentrations of the fibre planes (views).

### 6.2.2 KEK Solenoid Magnet

The four tracking stations were held in position and supported by carbon fibre rods as shown in figure 6.1 and installed inside an aluminium light-tight box. With the clear fibre waveguides attached, the complete prototype assembly was positioned inside a superconducting solenoid magnet developed in KEK (the JACEE magnet) which had an inner bore of 0.85m diameter, a 1.4m depth and a magnetic field of 1 Tesla in the bore. The tracker was positioned and locked in z and azimuthal positions within the solenoid bore. Figure 6.2 shows the downstream set up at KEK with the solenoid magnet, tracker, time of flight counter (TOF) and one of the trigger counters used, D1. Data were taken with the tracker/solenoid axis parallel to the beam axis (z) when using a high momentum beam and at 3° and 6° rotations when using a low momentum beam in order to increase transverse momentum for tracking purposes.

### 6.2.3 Beam Counters

Scintillation beam counters were used at the beam test beam primarily for event triggering and particle identification but were also used to measure the momentum of the extracted beam. The time of flight measurement at KEK was found by measuring the time difference between the time of flight (TOF) hodoscope which is

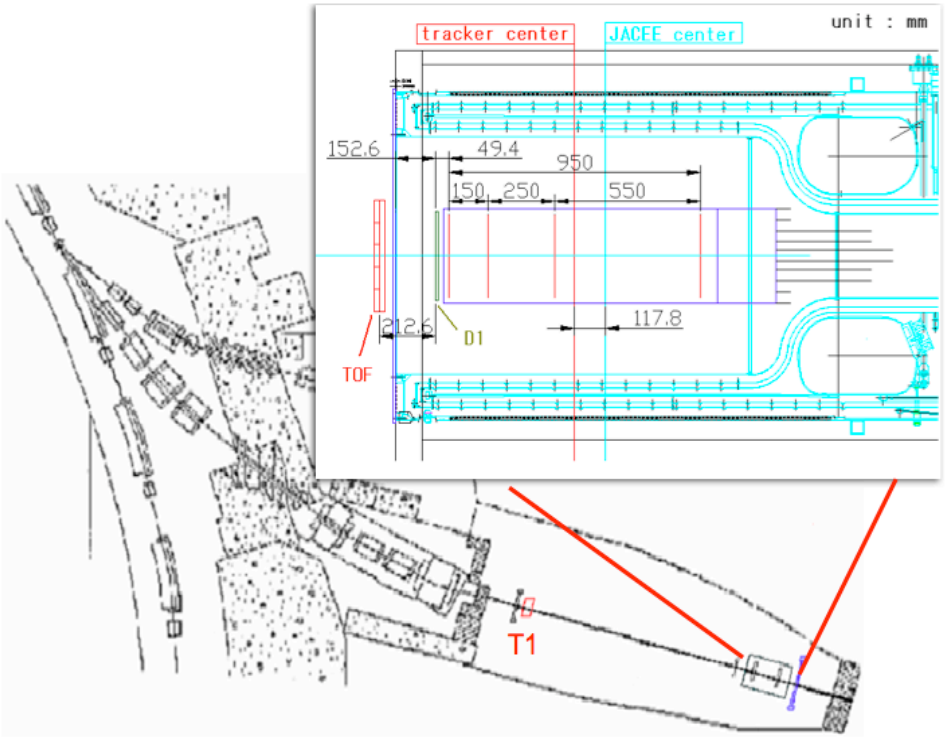


**Figure 6.2:** Hall layout at KEK showing the $\pi 2$ beamline coming from the KEK-PS and leading to the beam test area with the most upstream counter (T1), the downstream setup (magnified) to show the tracker and D1 counter positions within the solnoid magnet and also the TOF counter position.

positioned on the upstream end of the solenoid as shown in figure 6.3 and a trigger counter (T1) which is just over 8m upstream of the TOF.

The T1 counter is a plastic scintillator with dimensions of 5cm height, 10cm width and 4cm thickness and readout via 2 photomultiplier tubes, PMTs. The TOF hodoscope used at KEK, shown in figure 6.3, is of similar design to the MICE TOF, in that it consists of two plastic scintillating planes, but has five horizontal slabs and five vertical slabs. Each scintillator slab has dimensions 8cm x 40cm and 4cm thickness arranged such that the 5x5-slab hodoscope covers a 40cm x 40cm area. The TOF slabs are readout by PMTs at each end via long light guides, which were used in order to limit the magnetic field near the PMTs. The resolution of the TOF was calibrated to be ∼60ps [79], even in the presence of a fringe field from the magnet.

Two plastic scintillating discs called 'defining counters' (D1 and D2) were placed upstream and downstream of the prototype to select particles passing all the way through the tracker volume. D1 and D2 were identical, with a thickness of 1cm, a

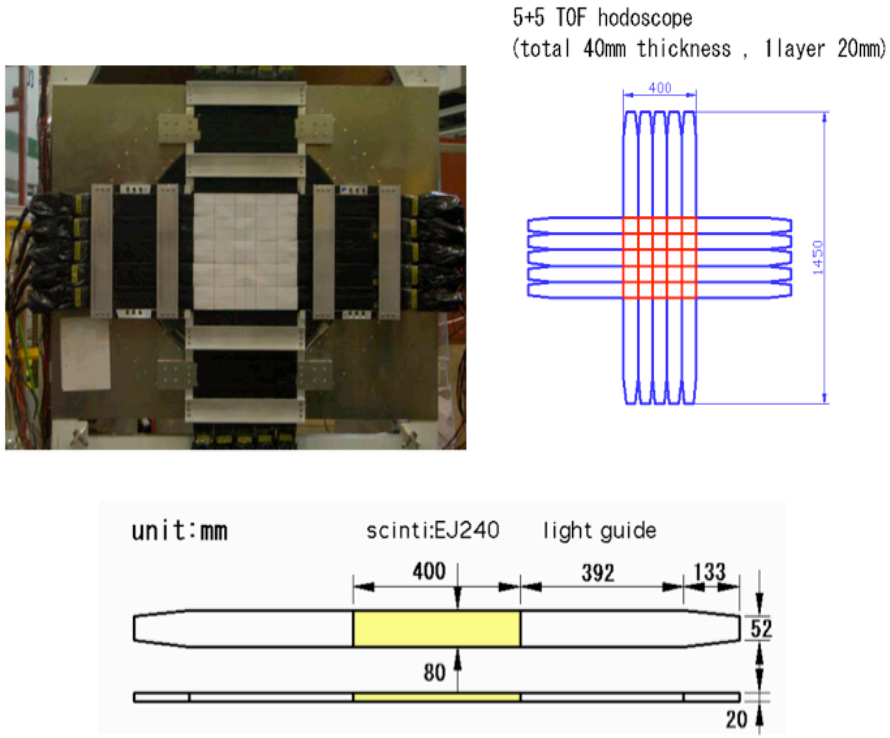


**Figure 6.3:** KEK TOF hodoscope shown attached to JACEE solenoid magnet at KEK beam test. Also, 5x5 design visuliased with the dimensions of each individual slab shown.

radius of 15cm to match that of the tracker stations and were each readout by a single PMT. D1 is shown in figure 6.2, just upstream of the tracker, while D2 (not shown in figure 6.2) is at a distance of ∼2.4m downstream of D1.

### 6.2.4 Data Acquisition

All the scintillation counters used at KEK were readout using a CAMAC ADC/TDC system. The TDCs used were CAEN V1290 modules with a 25ps resolution and the ADCs were CAEN V792 with 12 bit resolution. For the tracker, the optical readout and electronics system described in section 4.4 was used.

A newly developed prototype cryostat was used, with two VLPC cassettes, one high gain cassette (serial no. 111) and one low gain cassette (serial no. 105), which each readout two AFEII electronic readout boards (serial numbers 104, 107) and (105, 106) respectively. An overview of the DAQ system used at KEK is shown in figure 6.4. The readout of the AFEII boards was achieved using a VME crate with a Bit3 interface, a MIL-STD 1553 interface and four VLSB modules. As the AFEII boards

used were made for DØ they are designed for synchronisation with the Tevatron beam structure, therefore we could only readout events within a 100ns time period. The Level 1 Accept clock signal that provides this window of time, was integrated into the trigger logic used at KEK.

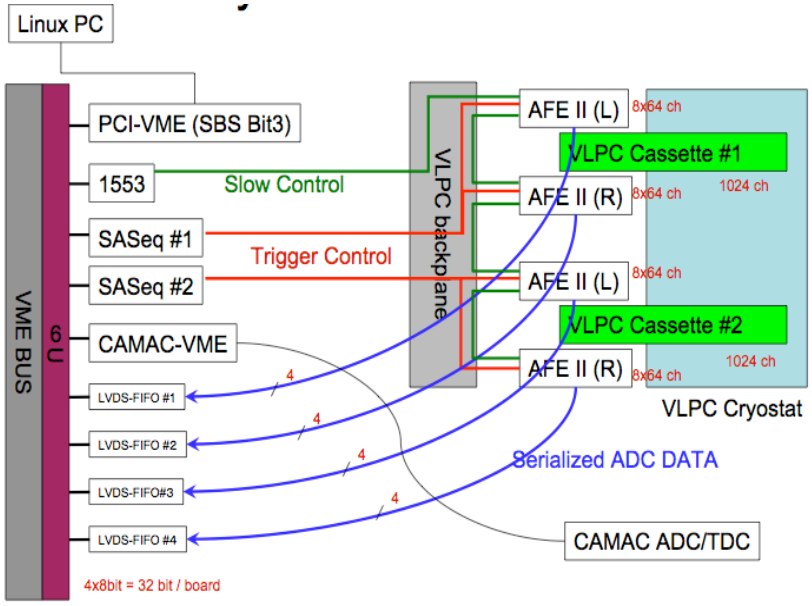


**Figure 6.4:** An overview of the beam test DAQ system used at KEK

### 6.2.5 Beamline

Protons from the KEK-PS incident on a target, produce a secondary beam of negatively charged particles. From this secondary beam, the KEK-PS $\pi 2$ beamline provided pions with momentum up to 3GeV/c and muons with momentum around $\sim$0.3GeV/c.

## 6.3 Data

### 6.3.1 Monte Carlo

The prototype tracker along with the other key components of the KEK beam test was implemented in detail in the geometry files within the G4MICE software using the GEANT 4 description of the detector. The KEK downstream mother volume

for example was the KEK solenoid, which had many volumes within volumes all the way down to the two cylinders (core and cladding) of the individual scintillating fibres. All components had individual files with material descriptions, dimensions and other specific information required as well as the positions and rotations of all of its daughter volumes. Therefore, all individual elements are placed relative to each other in the software according to measurements taken at the beam test. The position of the tracker including its individual fibre planes have had all positions and rotations implemented through alignment procedures described in section 6.4 as this intrinsic information was not obtained at the beam test when setting up the instrumentation.

The KEK beam was simulated using an application written in G4MICE which builds a KEK test beam configuration and uses the positions of the T1 and the D1 scintillators to generate a set of random particles starting upstream of T1 and travelling towards D1. For this analysis, only the beam composition and momentum of the simulated particle beam has been matched to the real KEK beam. The simulated beam has not been adjusted to have a similar beam profile, a"pencil beam" has been considered with a gaussian distribution of width 1mm in x and y, centred on the z axis, as this is assumed to be similar to that coming from the $\pi 2$ beamline. The average beam momentum was found to be $\sim$239MeV/c and the particle concentration of the beam to be around 80% $e^-$, 10% $\mu^-$ and 10% $\pi^-$. The output from the application providing the simulated beam is given in an ICOOL [60] format such that, it can then be read in by the G4MICE simulation.

The G4MICE simulation reads in the ICOOL beam file and records hit information as previously described in section 5.3. A trigger simulation is then run to select those events in which a coincidence of T1, TOF and D1 is present. After this the detector response is simulated using the G4MICE Digitisation application which stores digitised hit information for reconstruction. As described in section 5.4, the digitisation uses parameterisations to simulate the exact VLPC response for the prototype. This is important because the prototype has a number of different 3HF concentrations and hence different light production. The majority of the parameters used are based on experience gained by DØ but were also tuned to match the data from KEK. The coil positions and currents for the JACEE magnet have been implemented in G4MICE and used to simulate the real field map.

The number of Monte Carlo (MC) events were determined such that when looking at the final track fit results we have 10 times as much MC as real data. This

required 1.3 million simulated events to be generated for the 3° setup and 1.42 million simulated events for the 6° setup. For all analysis plots shown, where MC and data are compared, the data points are overlaid on the MC histograms, where the MC histograms have been normalised to the data.

### 6.3.2 Data acquired

Data for the prototype test at KEK was taken in a short, one-week period. The individual physics runs were set to a maximum of 20k triggered events. For the 250MeV/c beam data which is analysed in this thesis, the total data set consisted of 169,532 events for the 3° magnet-tilt setup and 159,250 events for the 6° magnet-tilt setup. Also, 192,300 events of 3GeV/c no magnetic field data (no magnetic tilt) was obtained for alignment purposes, the data runs used are listed in table 6.2.

| | $250 MeV/c$ ($3° setup$) | $250 MeV/c$ ($6° setup$) | $3 GeV/c$ ($0° setup$) |
|---|---|---|---|
| Run ID | 1356, 1358, 1360, 1361, 1363, 1365, 1367, 1368, 1370, 1372 | 1318, 1320, 1322, 1324, 1326, 1328, 1330, 1332 | 1257, 1258, 1259, 1272, 1273 |
| Total Triggered Events | 169,532 | 159,250 | 192,300 |

**Table 6.2:** Summary of data runs used for KEK analysis.

#### Trigger

The trigger was generated from a coincidence of the most upstream scintillator T1, the TOF hodoscope, the AFEII boards sampling clock (L1A) and the D1 scintillator immediately upstream of the prototype tracker. The AFEII sampling clock has an integration window built for synchronisation with the Tevatron for collisions at DØ . At KEK, where we have effectively a constant beam, a fake 'Tevatron signal' was produced by a purpose built electronics board and synchronised with the AFEII boards. This 'AVNET' board also passed the L1A signal from the trigger electronics to the AFEII boards.

### Cabling

Cabling and decoding files for the tracker were produced such that exact mapping of electronic channel (AFEII board, MCM, channel number) to physical channel (station, plane, fibre) including all the interfaces in between were well known. This mapping turned out to be quite a difficult task due to construction issues already mentioned (symmetrical old station connectors, see section 4.3.3) and also a non-logical channel mapping from waveguides to the (DØ designed) electronics boards. Cabling and decoding files were also written for the much simpler beam counters.

### Calibration and Noise

Characterisation of each of the 2048 channels was achieved through calibration runs of 10k events. This involved using an LED pulser to illuminate the VLPC readout system. To characterise the VLPC readout channel two spectra were obtained for each individual channel. The first determines the pedestal position and width, which gives the average value of the channel when there is no signal, this was typically of the order of 80-120 ADC counts. The second illuminated each channel with a pulsed LED, which determined the channel-by-channel gain required to calculate the mean number of photoelectrons.

Calibration spectra for both LED on and off for typical high gain and low gain cassette channels obtained at KEK, are shown in figure 6.5 and figure 6.6 respectively. The high gain cassette clearly shows the single photon counting capability of the VLPC, as does the low gain cassette, but to a lesser extent. A fit was performed allowing the pedestal and gain to be determined. The pedestal data is stored for each channel such that the pedestals can be subtracted from all signals, therefore, in the absence of a signal the pedestal-subtracted data for each channel is centred around zero. In total, only 12 out of 2048 VLPC channels were not analysed due to dead VLPCs or break down due to high voltage.

The common mode noise (CMN), is the average (common) fluctuation in the signal level for all 64 channels on a Trip chip for an event due to common background noise. The event-by-event calculation is performed as the first part of the reconstruction process in the G4MICE software. The CMN subtraction procedure is performed on all VLPC hits and calculates the average pedestal-subtracted signal.

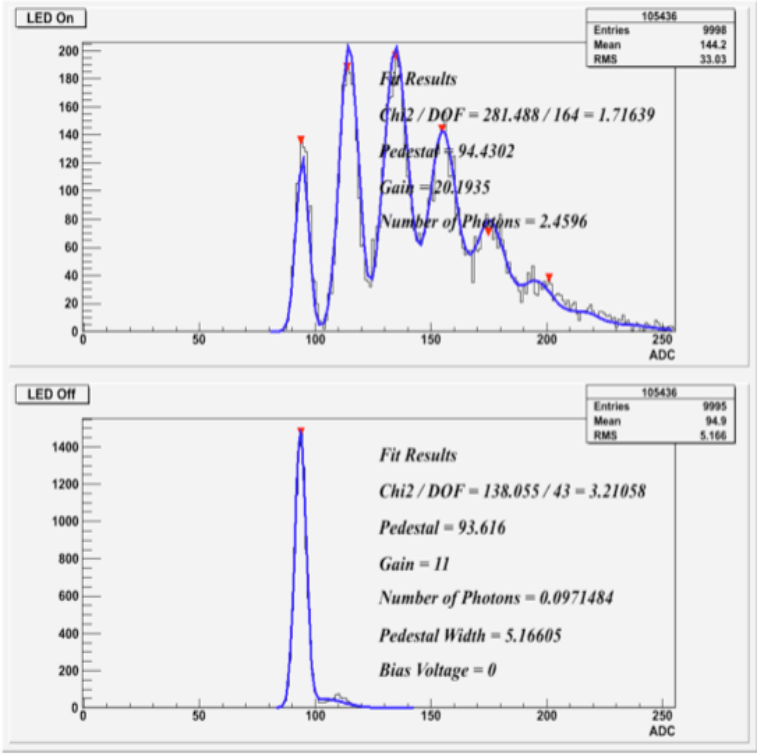


**Figure 6.5:** Calibration spectra for a typical high gain cassette channel. Top plot shows LED on and bottom plots shows LED off.

After the characterisation of the individual VLPCs, a hit is defined in the software to be a signal above 1PE, which is then associated to a fibre channel (bundle of seven fibres) using the decoding files. Also, as before, possible clusters (groups of neighbouring hits) are searched for and then considered, when the sum of individual pulse heights is greater then 2PE.

## 6.4 Alignment

The geometry of the SciFi and its support structure shown in figure 6.1 wasn't surveyed by mechanical means after installation in the magnet at KEK. The station spacings ($\Delta z$) were known (see table 6.1) due to the rigid supports that held them in place, also all stations had 'X views', therefore these were aligned for all four stations.

The alignment of the tracker stations was achieved using straight tracks from the 3 GeV/c, no magnetic field data. The first step loops over all spacepoints in the

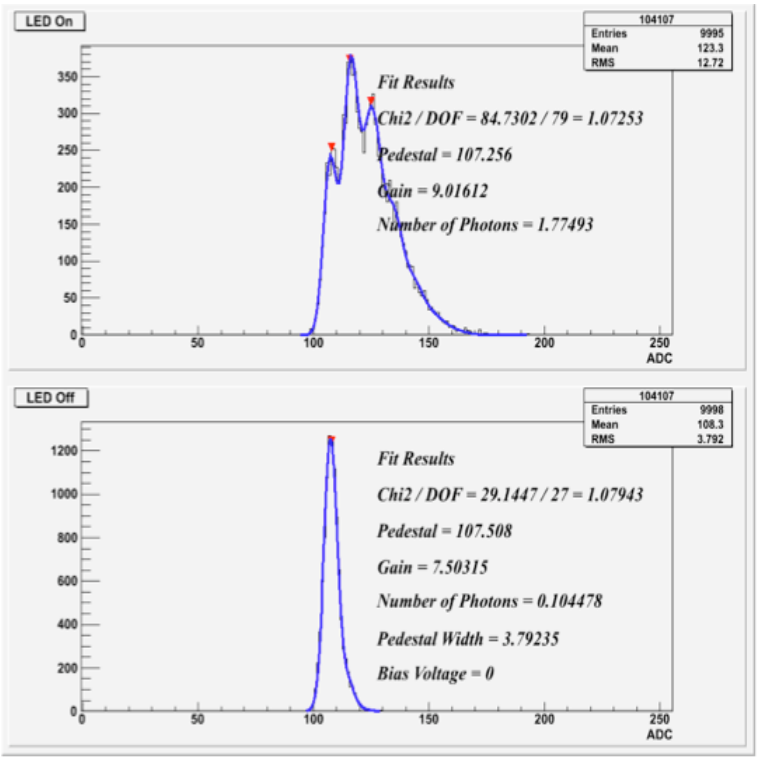


**Figure 6.6:** Calibration spectra for a typical low gain cassette channel. Top plot shows LED on and bottom plots shows LED off.

two outermost stations D and B, which are the two 3 'view' stations, such that we have "triplets", where a check of the internal residuals in station D and B are found. These two space points in stations D and B are then connected to a straight line fit. From this straight track, space points in station A are searched for, giving a predicted point. Residuals in x and y positions are then found by finding the difference between the predicted and reconstructed points in station A. This process is then repeated for station C.

Figure 6.7 shows the distributions of the difference between the predicted and reconstructed space point positions in stations A and C for both transverse spatial coordinates (x and y), where a gaussian fit to all the distributions yields the residuals.

| Alignment | $\sigma_{\text{xresidual}}$ (mm) | $\sigma_{\text{yresidual}}$ (mm) |
|---|---|---|
| A | $0.718 \pm 0.009$ | $0.623 \pm 0.005$ |
| C | $0.717 \pm 0.008$ | $0.618 \pm 0.006$ |

**Table 6.3:** Residuals found for stations A and C with statistical errors.

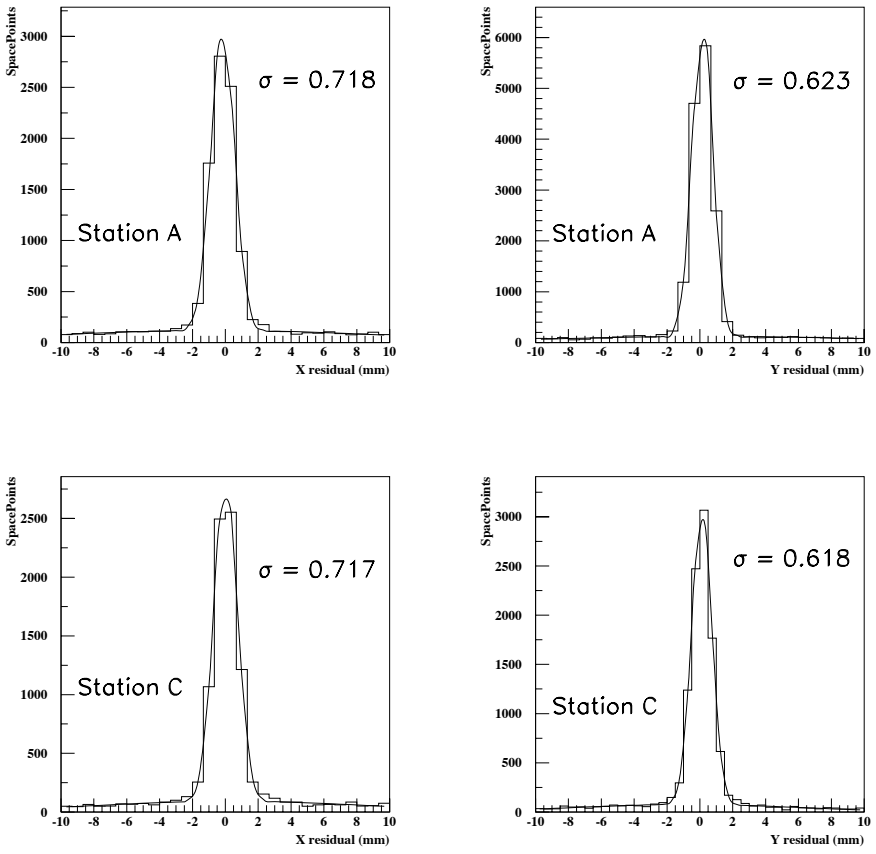


**Figure 6.7:** Distributions of x and y residuals for both station A and C

The expected residuals in x and y are calculated in equations 6.1 and 6.2 respectively, such that:

$$\sigma_x(residual) = k\,(\sigma_x/cos30^\circ) = 0.72mm \tag{6.1}$$

$$\sigma_y(residual) = k\sigma_y = 0.62mm \tag{6.2}$$

where k is a constant for any given track and $\sigma_x$ and $\sigma_y$ are the intrinsic resolutions in x and y found from the channel pitch. The x-view of both stations (A and C) lies along the y-axis and the other views V and W for stations A and C respectively are aligned at 30° from the x-axis. The residuals shown in figure 6.7 are given in table 6.3 and shown to be very close to the expected values. Figure 6.8 gives profile plots

showing the variation of space point residuals found along the respective position coordinates of both stations (A and C) to be within the channel pitch.

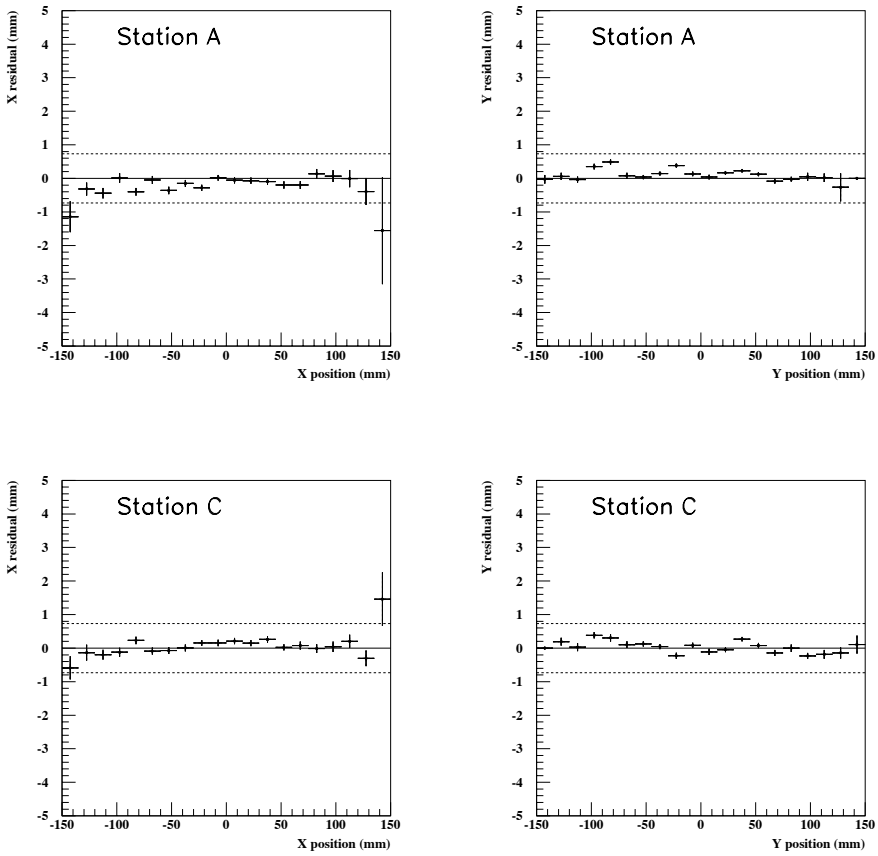


**Figure 6.8:** Profile plots showing the variation of space point residuals in x and y found along the respective position coordinate of both stations (A and C). The dotted lines indicate the channel pitch.

## 6.5 Particle Identification

The particle identification at KEK was obtained simply through the difference in time measured between the upstream trigger counter T1 and the vertical slabs of the TOF hodoscope. The TOF horizontal slabs were read out on a different TDC board to the T1 counter and TOF vertical slabs. These two different TDC boards were not synchronised, therefore the horizontal slabs were not used for the time of flight measurement from T1. Delays due to cable lengths and PMT transit times were not known exactly so the MC has been tuned to match the delay times of that

found from the data. The particle identification at KEK for a 250MeV/c beam is shown in figure 6.9 where three clearly separated peaks show electron, muon and pions for both MC and data. Due to the MC not having a complete description of the momentum spectrum for the muons and pions as a result of the real beam not being characterised, the PID cuts chosen are in the range where the MC and data match.

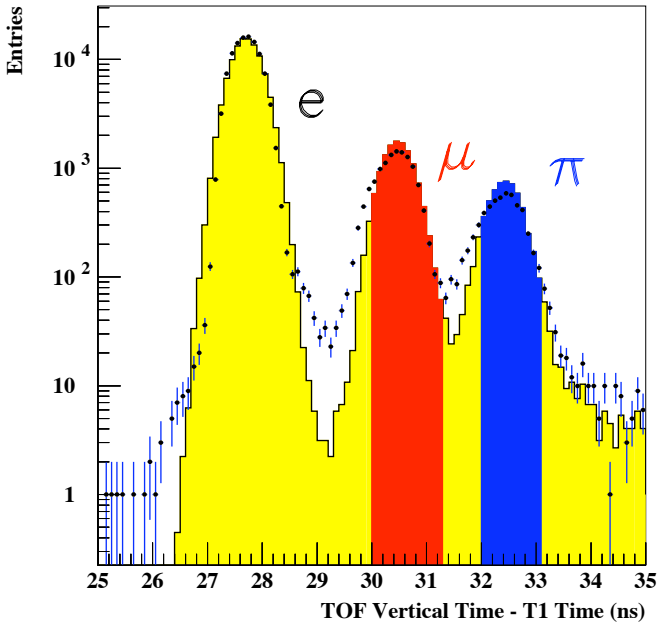


**Figure 6.9:** Particle Identification from time of measurement. The red (muon) and blue (pion) shaded areas indicate the selected areas used for the event selection in the analysis.

## 6.6 Event Selection

The event selection used for the analysis is achieved by requiring a number of selection criteria be passed. Firstly, all events must have recorded a hit in each of the scintillation counters, T1, TOF, D1 and D2, where a hit is defined as having a number of photo electrons (PE) $> 0$. Also, all events are required to pass tracking acceptance cuts in addition to those already required by the pattern recognition described in section 5.5.3, these tracking cuts are shown in figure 6.10 for MC and data for the 6° setup and are as follows:

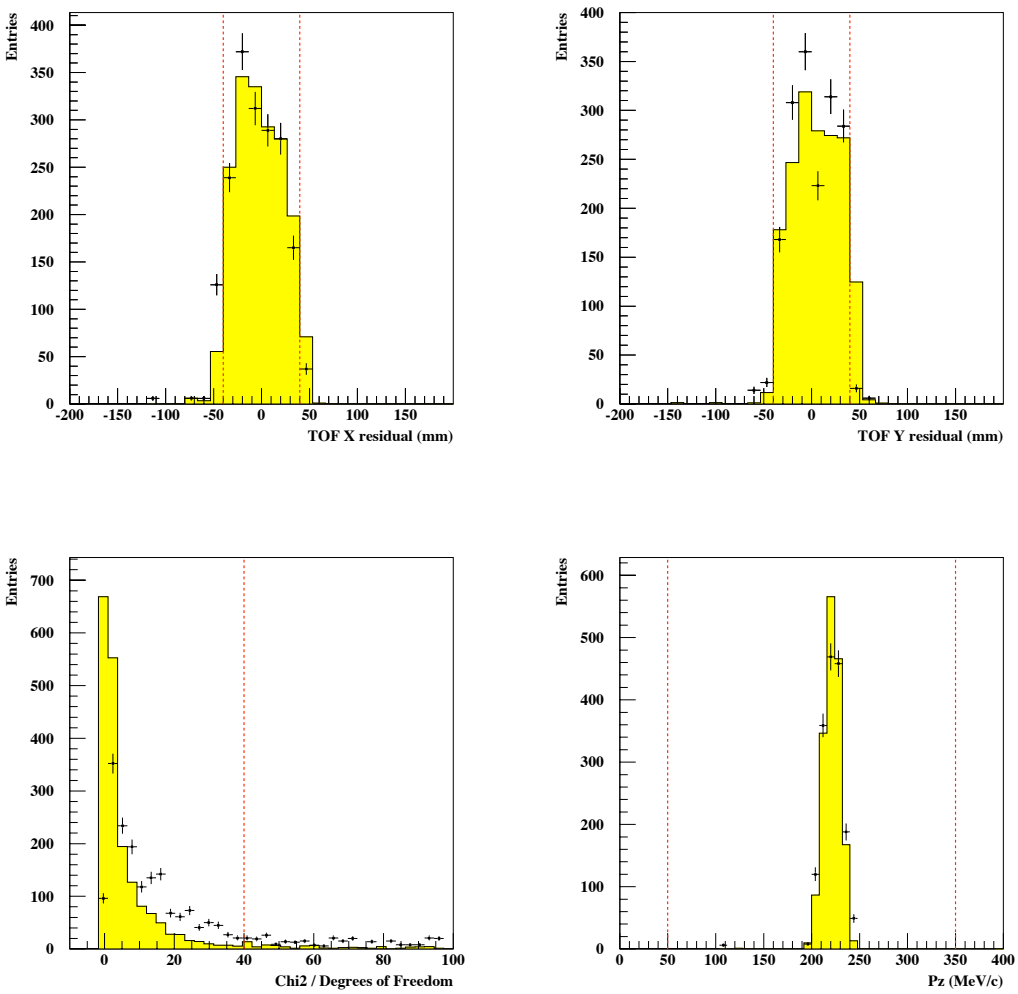


**Figure 6.10:** Event selection cuts for both MC (histogram) and real data (data points), where for each distribution all other cuts are used except its own. The dotted lines show the values where the cuts will be made. The Pz distribution is coming from TOF (see section 6.7)

- A cut is made from the residual from the TOF such that the residual is found to be within the dimensions of a single TOF slab (80mm). The residual is defined as the difference between the predicted position of a hit in the TOF and the measured position in the TOF. The predicted position of the hit is the extrapolation of the track coming from the Kalman filter to the z position of the TOF and the measured position comes from the TOF counter itself.

- A cut on the $\chi^2$ per degree of freedom coming from the Kalman fit allows the quality of the tracks used in the analysis to be of a reasonable standard, a cut of $0 < \chi^2 < 40$ has been used. There is a slight discrepancy in the $\chi^2$ per

degree of freedom between MC and data, this was not investigated in depth as by making the cut $< 40$ is considered sufficient for this analysis, but a possible cause of the difference could be due to the fact that $p_z$ is coming from the TOF and we have a very small $\sigma_{pz}$ from the error estimation, which leads to little variation in the track fit which effects the $\chi^2$ per degree of freedom calculation.

- The longitudinal momentum $p_z$ is required to be within the range of 50MeV/c and 350MeV/c.
- Only events which are found to come from either muons or pions are used in the analysis as shown in figure 6.9.
- Finally, for the real data only, a cut is made from plotting the mean number of photo electrons $\langle N_{PE} \rangle$ versus the time difference between the Level 1 Accept trigger (integration window in Trip chip) and the upstream T1 counter as this provides a time period ("flat-top") where the light yield is greatest as shown in figure 6.11 and rejects events in which beam particles are not synchronised to the Trip chip.

## 6.7 Tracker Performance

For MICE, the track fit is a major part of the experiment, as it provides the four-dimensional parameters to produce the transverse emittance measurement, therefore it was seen as a useful test at KEK to check the performance of the tracker by measuring the momentum and spatial resolutions from fitted tracks. There were limiting factors with the prototype tracker test which will not be the same for the final trackers in MICE, such as fewer tracking planes (10 instead of 15) and a quarter of the magnetic field that will be used in the MICE solenoids. The track fit analysis has been performed using both the 3° and 6° setups, but the figures showing the distributions and resolution results are only shown for the 6° setup as this is considered slightly more interesting as it produces more transverse momentum.

The track fit was achieved using the G4MICE tracker reconstruction, which was described in detail in section 5.5. The only difference in the reconstruction comes from only having a 1-tesla field at KEK, which leads to a small value of the azimuthal angle from the beam axis. This led to problems when reconstructing the longitudinal momentum ($p_z$) at KEK. Therefore, the seed value for $p_z$ used for the

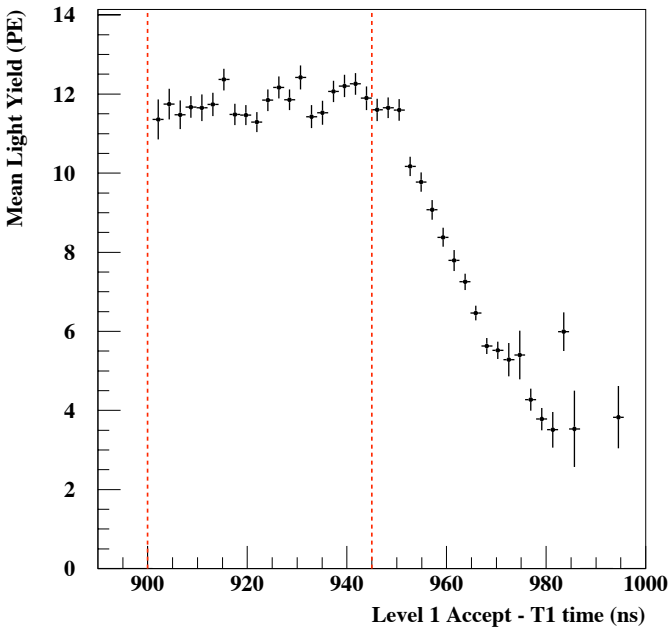


**Figure 6.11:** Event selection cut used for real data only, showing the "flat-top" time period (the time difference of L1A and T1) at which the light yield performance is greatest.

track parameters passed to the Kalman fit from the pattern recognition now comes from the time of flight instead of the helix (see section 5.5.3).

The following analysis has checked the comparison of data and MC for the distributions of the two spatial coordinates transverse to the tracker's axis (x and y). The simulation gives a reasonable description of the data as shown in figure 6.12. A small offset in the MC is found in the y position distribution, this is due to the simulated beam not exactly matching the beam used at KEK.

The spatial resolution of fitted tracks are shown in figure 6.13, where the distributions shown come from the difference between the fitted position of the reconstructed track and the MC true position. A single gaussian fit is applied, giving the standard deviations of the distributions to be $\sigma_x = 473\mu$m and $\sigma_y = 412\mu$m for x and y respectively. The expected resolution determined from the fibre pitch and seven fibre bundling scheme is $472\mu$m when including multiple scattering effects, which is in close agreement with the results found for $\sigma_x$ and $\sigma_y$.

The momentum distributions ($\mathrm{p_x}, \mathrm{p_y}, \mathrm{p_t}, \mathrm{p_z}$) comparing MC and data are shown in figure 6.14. A small offset in the MC ($\mathrm{p_y}$) distribution is found, again this is a result

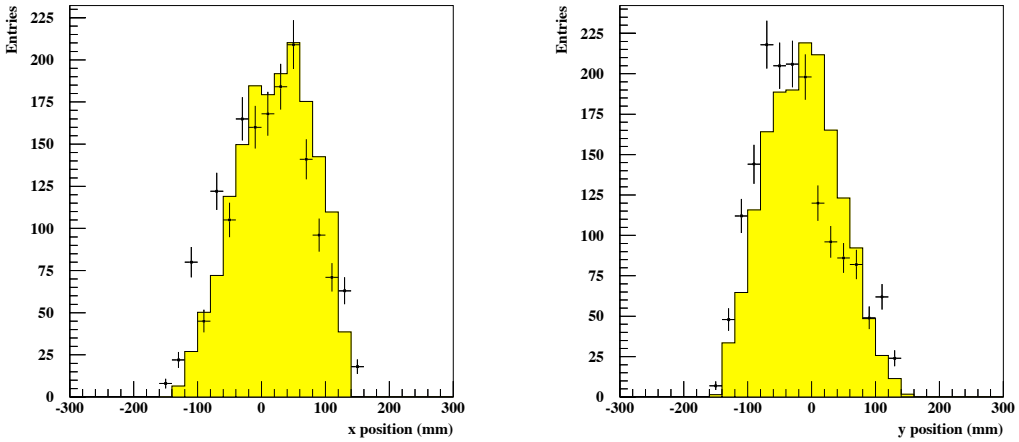


**Figure 6.12:** Reconstructed transverse spatial coordinates coming from the Kalman track fit. The histogram shows MC and the points overlaid are showing the real data.

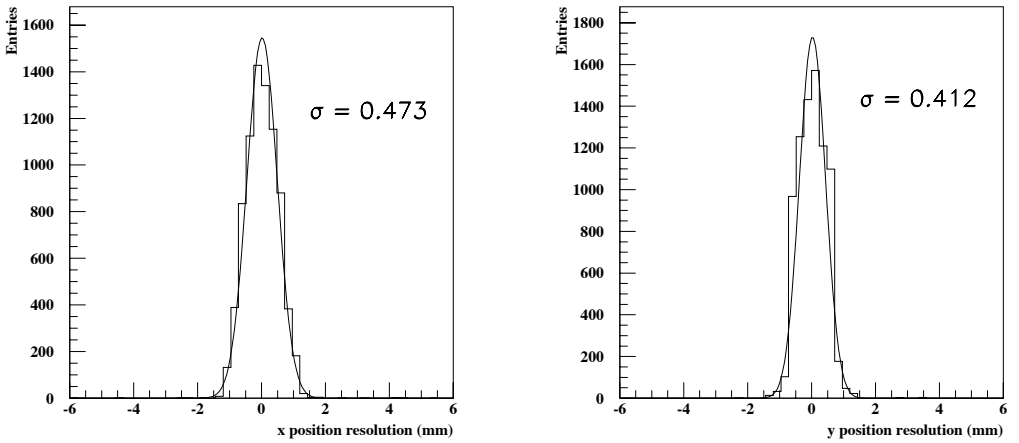


**Figure 6.13:** Resolutions (reconstructed - MC truth) of transverse spatial coordinates x and y.

of the difference between the simulated beam and the real KEK beam, which also resulted in a slightly greater $p_t$ coming from the MC. A systematic test has been evaluated and described in section 6.7.2 showing that the difference in the input beams has not affected the final track fit resolution results obtained.

The momentum resolution distributions are shown in figure 6.15 and are found using the same method as for the spatial resolutions. A summary table 6.4 gives the resolutions for all track fit parameters studied along with their respective statistical

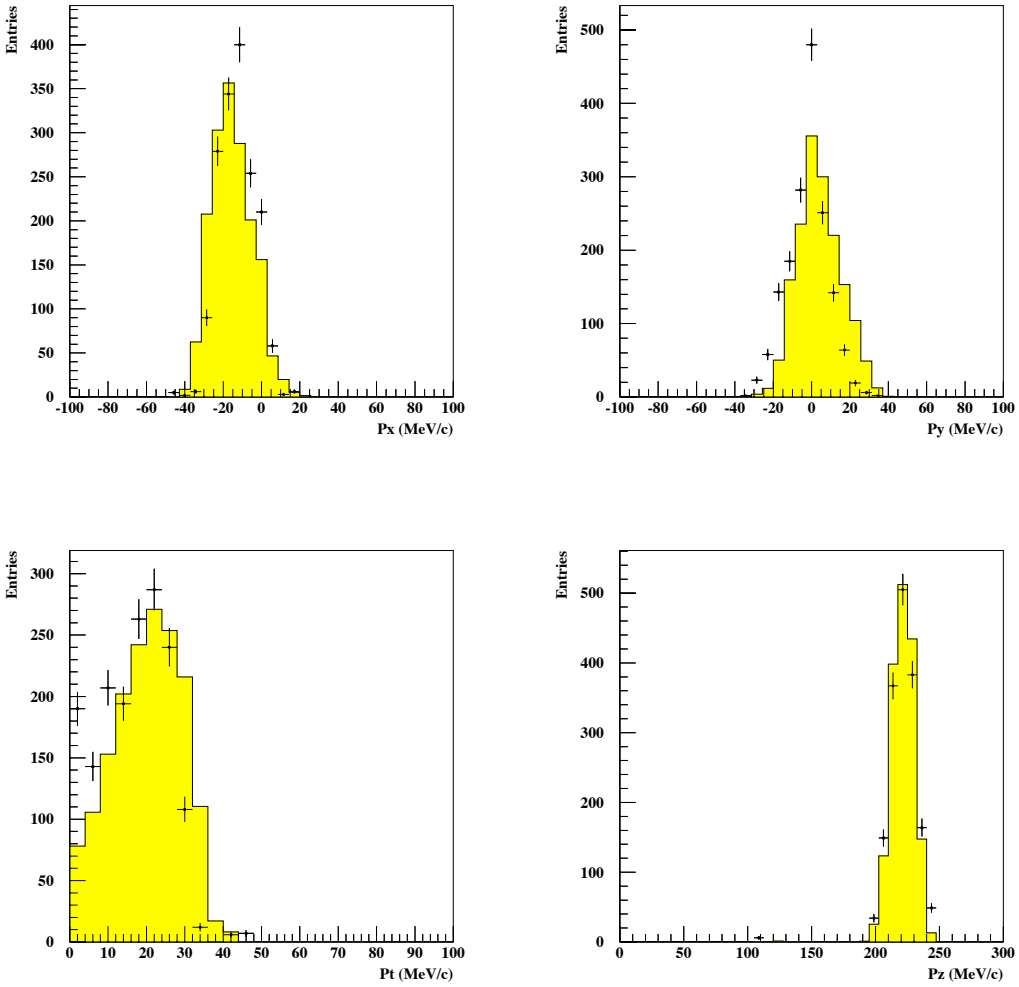


**Figure 6.14:** Reconstructed momentum ($p_x$, $p_y$, $p_t$ and $p_z$) coming from the Kalman track fit. The histogram shows MC and the points overlaid show the data. Again, the $p_z$ is from TOF.

and systematic errors, for both the 3° and 6° configurations.

| | 3°setup | 6°setup |
|---|---|---|
| $\sigma_x$ | $0.471 \pm 0.001 \pm 0.001$ | $0.473 \pm 0.003 \pm 0.004$ |
| $\sigma_y$ | $0.413 \pm 0.001 \pm 0.001$ | $0.412 \pm 0.003 \pm 0.004$ |
| $\sigma_{px}$ | $2.516 \pm 0.012 \pm 0.086$ | $2.877 \pm 0.031 \pm 0.135$ |
| $\sigma_{py}$ | $2.401 \pm 0.012 \pm 0.105$ | $2.614 \pm 0.029 \pm 0.142$ |
| $\sigma_{pt}$ | $3.215 \pm 0.014 \pm 0.140$ | $3.403 \pm 0.034 \pm 0.158$ |
| $\sigma_{pz}$ | $9.507 \pm 0.029 \pm 0.009$ | $9.417 \pm 0.069 \pm 0.108$ |

**Table 6.4:** Track fit Performance Summary.

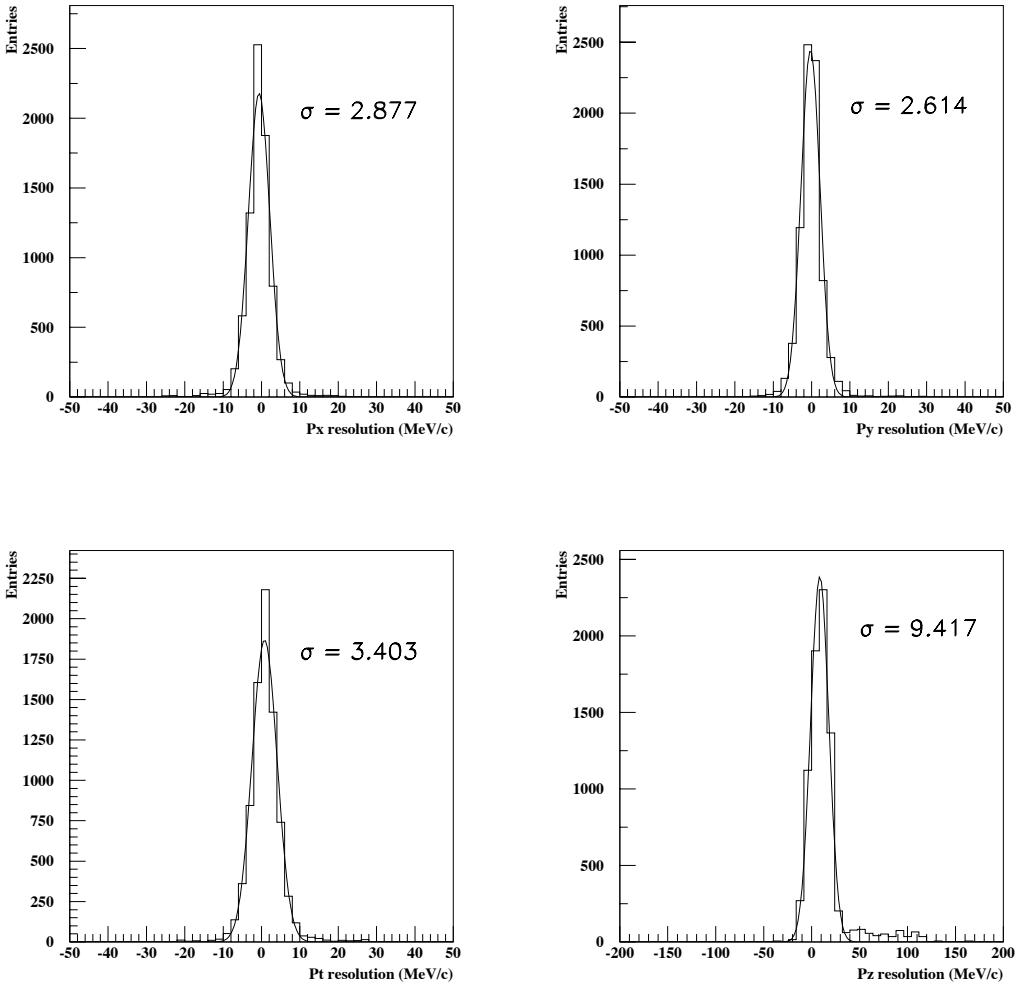


**Figure 6.15:** Momentum resolutions (reconstructed - MC truth) coming from the track fit.

### 6.7.1 Light Yield

A key element in determining the performance of the MICE trackers along with the spatial measurement from the fibre pitch is the amount of light produced, therefore a check of the light yield performance of the prototype tracker at KEK was important. The light yield is determined by plotting the pulse height distributions using only events that contained a reconstructed track. From previous experience (see section 4.3.1) from DØ and also an initial cosmic ray test using the three station prototype, the mean light yield expected from the tracker is $\sim 10$ PE. The pulse height (mean number of photoelectrons) $\langle N_{PE} \rangle$ is determined for the real data for every individual hit, by finding the pedestal-subtracted ADC count of a 'VLPC hit' and dividing

this by the gain obtained from the individual VLPC characterisations described in section 6.3.2. The simulated pulse height distributions are found using G4MICE as follows [64]:

- G4MICE calculates the distribution of energy lost in a doublet layer;
- A multiplicative factor, to be used to convert the energy deposited in the fibre into an expected number of photoelectrons, is then determined by comparing the mean of the generated energy-loss distribution to the mean of the measured pulse-height distribution;
- G4MICE then convolutes the energy loss distribution with the Poisson photo-statistics distribution. Event-by-event the energy deposited in a doublet layer is converted to an expected mean number of photo electrons $\langle N_{exp} \rangle$ using the multiplicative factor determined in the previous step. The simulated number of photo electrons is then obtained by sampling the Poisson distribution with a mean of $\langle N_{exp} \rangle$.

The simulated light yield distribution is compared to the data for both the 3° and 6° setups for all stations and views at KEK, both give a reasonable comparison as shown in figure 6.16. They aren't identical, due to the VLPC energy resolution being slightly more conservative in the MC resulting in a broadening of the distribution, but we are only interested in the mean number of photoelectrons which is shown to be $\sim$ 10 PE for both and this is all that is required for this analysis.

A study of the light yield per view for all four tracker stations is given in table 6.5 with statistical and systematic errors. These results were produced using just the 3° setup due to the higher statistics obtained. The light yield is given by the most probable value, which is obtained using a gaussian fit to the peak of the pulse height distribution as shown in figure 6.17, where a typical view from an old station (station A, view V) and a view of from the new station (station D, view V) are given. The fitted mean light yield for the three old stations (A, B and C) shows values between 9.8 - 11.6 PE as expected, but a significant amount of light loss is found in the new fourth station (D) with a fitted mean light yield of $\sim$ 6.9 PE.

This loss of light was not understood at the time, as the new fourth station was constructed after experience gained from the old stations and expected to be an example of the final stations for the MICE trackers.

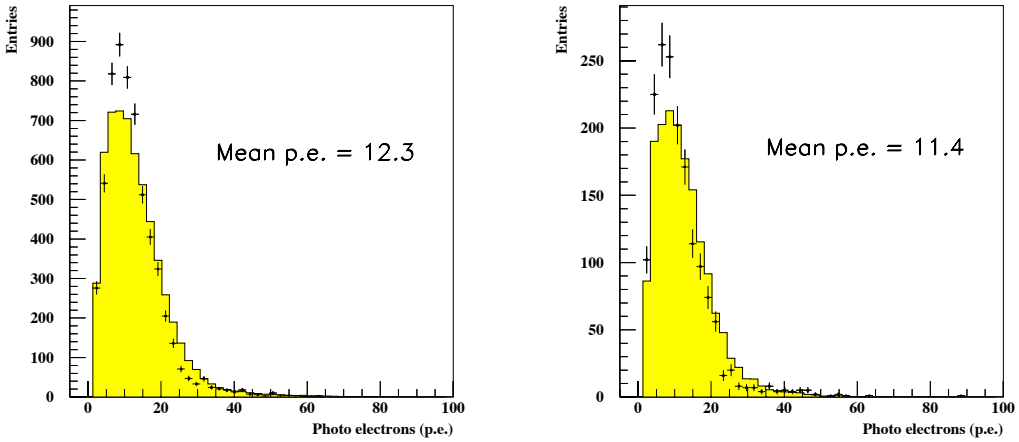


**Figure 6.16:** Light yield distributions for 3° (left) and 6° (right) setups. The histogram shows MC and the points overlaid, show the data. The mean PE quoted is from real data.

| Station | View | Light Yield (Most Probable, PE) |
|---|---|---|
| A | V | $11.10 \pm 0.32 \pm 0.19$ |
| A | X | $10.88 \pm 0.43 \pm 0.18$ |
| B | V | $9.90 \pm 0.62 \pm 0.46$ |
| B | X | $9.83 \pm 0.31 \pm 0.20$ |
| B | W | $11.26 \pm 0.46 \pm 0.21$ |
| C | X | $11.61 \pm 0.46 \pm 0.23$ |
| C | W | $9.97 \pm 0.62 \pm 0.30$ |
| D | V | $6.85 \pm 0.32 \pm 0.17$ |
| D | X | $6.94 \pm 0.23 \pm 0.24$ |
| D | W | $6.90 \pm 0.26 \pm 0.15$ |

**Table 6.5:** Summary of light yield performance per plane at KEK with statistical and systematic errors shown (see section 6.7.2).

### Light Loss investigation and new stations since KEK

Once the KEK test was complete, the tracker prototype was disassembled and possible reasons for the loss of light in the fourth station were studied. The reason was eventually found to come from the new patch panel connectors which were only used on the new station. The patch panel connectors as shown in figure 4.7 were found to have a drilling mis-alignment of the holes that are interfaced between the two halves of the patch panel connectors. A few slightly offset channel holes were initially found by eye which led to the possibility of a mis-alignment between the

interfaces.

To check this possible mis-alignment of the fibre areas, the hole centres of every channel were measured using a microscope attachment on a jig boring machine with digital X-Y readout. Once all channels were measured, the coordinates were put into AutoCad where an overlapping area was found and averaged for each connector, where the overall percentage loss due to misalignment is given as a percentage [80]. These measurements found a misalignment between $15.6\% - 25.5\%$ on each of the 5 patch connectors used for station D after taking the fibre cladding (approximately $\sim 12\%$ of diameter) into consideration. One of the patch panel connector measurements is shown in figure 6.18, showing the overlapping of the two interfaces. After finding this result, it was realised that the reason for the drilling misalignment was understood to be from issues with the drilling machinery, where the holes were not center drilled.

The new station connectors used only on station D, were drilled using the same method and equipment as the patch panel connectors. The old station connectors for stations (A, B and C) were known to have been centre drilled and therefore considered to be satisfactory. Identical measurements of a new station connector and all its channel holes were found using an unused test piece as shown in figure 6.19, where an overall misalignment loss between the interfaces was found to be 15.8%. Combining this with the misalignment found from the patch panel connectors gives an overall misalignment averaging between roughly $31\% - 41\%$ for station D, which is in the range of the percentage of light lost in Station D when compared to the three old stations.

### 6.7.2 Systematic Errors

The systematic errors given in the tracker performance results, are shown in tables 6.6, 6.7 and 6.8 have been evaluated by performing the full analysis using varying different treatments of the data. The estimate of the systematic error is then taken to be the difference with the main results. Once all the systematic errors for each different treatment has been obtained, all the errors are combined in quadrature giving the total shown. Five different techniques were studied to examine the systematic errors on the track fit resolutions and light yield analysis.

- $\chi^2$: The $\chi^2$ cut which describes the quality of the track fit coming from the Kalman fitting algorithm is normally set to $0 < \chi^2 < 40$. To test the effect of the cut, it has been increased by 50% to be $0 < \chi^2 < 60$.

- **Extrapolation to TOF**: This cut required an extrapolation of the track to the TOF hodoscope. The cut used was set at $0 < |\mathrm{TOF}_{\mathrm{residual}}| < 40$ in both x and y transverse position coordinates, so this was randomly chosen to be increased to $0 < |\mathrm{TOF}_{\mathrm{residual}}| < 60$ for both x and y dimensions to test the systematic effect.

- **PID**: The analysis performed used only muons and pions with cuts performed on the edge of the muon and pion peaks shown in figure 6.9, these boundaries were expanded by $\sim 30\%$ to see what effect this might have.

- **Transverse Momentum**: Due to the simulated beam not matching the real KEK beam exactly, the $p_t$ in the Monte Carlo was found to be slightly greater than the real data, as shown in figure 6.14, therefore to test that the difference in the simulated beam had no significant effect on the track fit results, a cut of MC $p_t < 30$ was studied.

- **Trigger cut**: The time difference cut between Level 1 Accept and the T1 counter (L1A - T1TIME) is important to the light yield analysis as shown in figure 6.11 showing PE vs L1A-T1TIME, which shows the "flat-top" where light yield is greatest. An increase of 10% on the bounds of the cut was studied.

| 3°setup | $\chi^2$ | Extrapolation to TOF | PID | $p_t$ | Total |
|---|---|---|---|---|---|
| x | 0 | 0 | 0 | 0.001 | 0.001 |
| y | 0 | 0.001 | 0 | 0 | 0.001 |
| $p_x$ | 0.021 | 0.071 | 0 | 0.043 | 0.086 |
| $p_y$ | 0.024 | 0.092 | 0 | 0.045 | 0.105 |
| $p_t$ | 0.036 | 0.114 | 0 | 0.073 | 0.140 |
| $p_z$ | 0.007 | 0.004 | 0 | 0.003 | 0.009 |

**Table 6.6:** Contributions from systematic errors for 3° setup track fit parameters.

## 6.8 Summary

The results shown from the KEK beam test have tested all the basic aims of the experiment along with allowing valuable experience to be gained in setting up and

| 6°setup | $\chi^2$ | Extrapolation to TOF | PID | $p_t$ | Total |
|---|---|---|---|---|---|
| x | 0 | 0.002 | 0 | 0.003 | 0.004 |
| y | 0 | 0.002 | 0 | 0.003 | 0.004 |
| $p_x$ | 0.030 | 0.085 | 0 | 0.100 | 0.135 |
| $p_y$ | 0.028 | 0.032 | 0 | 0.136 | 0.142 |
| $p_t$ | 0.066 | 0.066 | 0 | 0.128 | 0.158 |
| $p_z$ | 0.007 | 0.054 | 0 | 0.093 | 0.108 |

**Table 6.7:** Contributions from systematic errors for 6° setup track fit parameters.

| Station | View | $\chi^2$ | Extrapolation to TOF | PID | Trigger Cut | Total |
|---|---|---|---|---|---|---|
| A | V | 0.02 | 0.13 | 0 | 0.14 | 0.19 |
| A | X | 0.12 | 0.09 | 0 | 0.10 | 0.18 |
| B | V | 0.24 | 0.37 | 0 | 0.14 | 0.46 |
| B | X | 0.14 | 0.13 | 0 | 0.05 | 0.20 |
| B | W | 0.17 | 0.07 | 0 | 0.11 | 0.21 |
| C | X | 0.20 | 0.11 | 0 | 0.04 | 0.23 |
| C | W | 0.21 | 0.08 | 0 | 0.20 | 0.30 |
| D | V | 0.14 | 0.02 | 0 | 0.10 | 0.17 |
| D | X | 0.06 | 0.23 | 0 | 0.05 | 0.24 |
| D | W | 0.07 | 0.08 | 0 | 0.11 | 0.15 |

**Table 6.8:** Contribtuions from systematic errors for light yield results in the 3°setup for all 10 tracker views.

using the tracking device in a real experimental environment. Also, valuable experience has been gained in using the optical readout, electronics and cryostat systems.

The test has shown to be very useful in terms of confirming the construction of the tracker stations, in terms of alignment, as well as exposing problems with the connectors during construction that had a significant effect on the light yield produced, which is key to the MICE trackers performance.

The drilling issue has now been rectified and solved during construction of the final patch panel and station connectors used for MICE. This, along with every key step in the construction process for the final tracker stations, has since gone through detailed quality assurance procedures, described in detail in [9]. Newly developed tracker stations used in the 'real' MICE tracker(s), have now been built and tested recently in a cosmic ray test stand at Rutherford Appleton laboratory, using the new station connectors and patch panel connectors. These results are shown in the following chapter.

The track fit performance of the prototype has also been shown and the resolution results of the track parameters are close to those expected, which is good when considering the limited tracking planes used in the prototype. It also allowed, a successful test of the G4MICE software package, including the tracker reconstruction algorithms on real data.

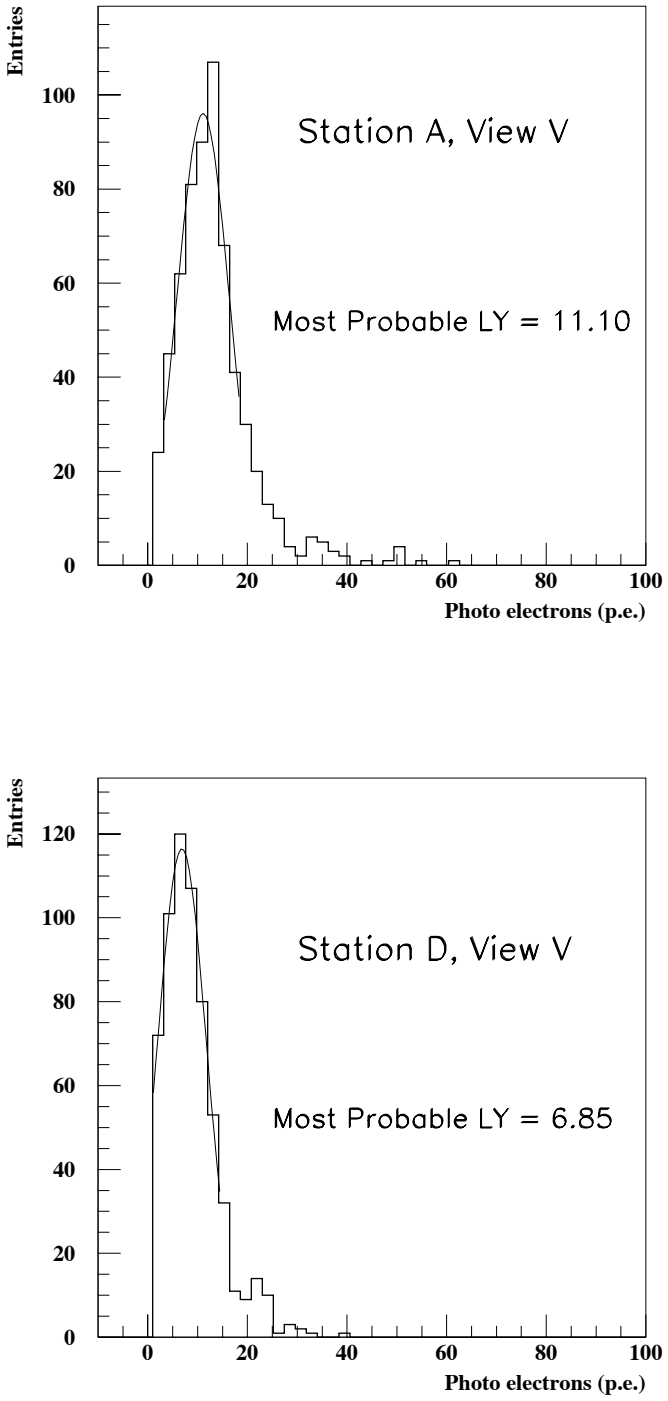


**Figure 6.17:** Light yield distributions of a typical view from an old (station A, view V) and new station (station D, view V). A gaussian fit to the distribution peaks gives the most probable PE. which shows a significant loss of light in the new station (D).

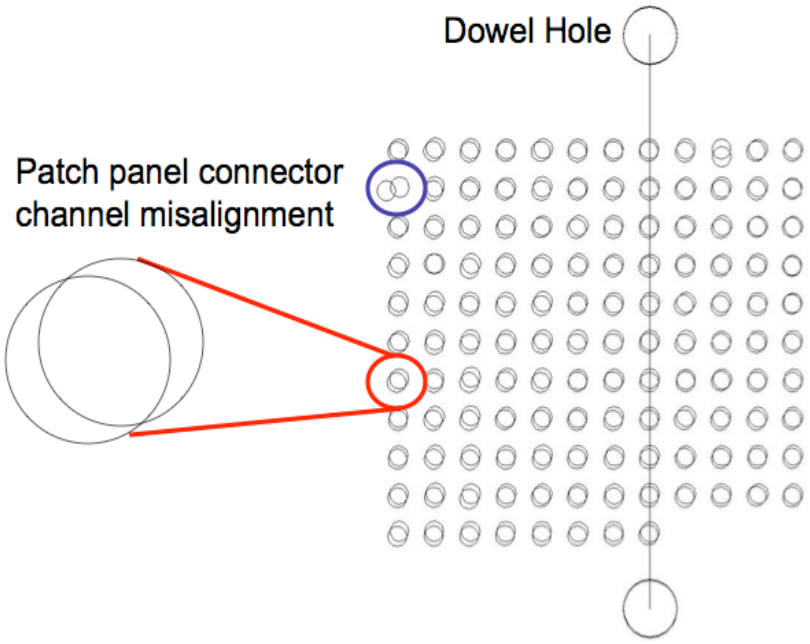


**Figure 6.18:** Patch panel connector misalignment. AutoCad plot of one patch panel connector (number 104) showing the fibre/area misalignment between the two interfaces found from the x-y coordinate measurements.

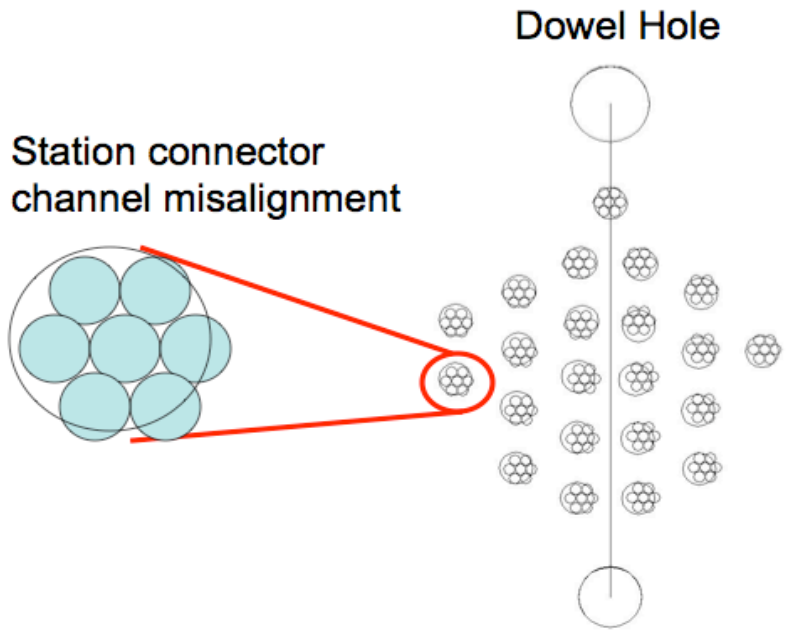


**Figure 6.19:** New station connector misalignment. AutoCad plot of a new station connector showing the fibre/area misalignment between the two interfaces found from the x-y coordinate measurements.

# Chapter 7

# Cosmic Ray Test

## 7.1 Introduction

After the two trackers which are to be used in MICE had been constructed using quality assurance procedures [9], they were both examined in a cosmic ray test stand at Rutherford Laboratory in late 2008 for 'tracker 1' and in the summer of 2009 for 'tracker 2'. The aim of the cosmic ray test was primarily to check that the light yield produced is sufficient for the tracking performance required for MICE, whilst in the process confirming that the light loss issue, found with the tracker prototype used at the KEK test (chapter 6) had been resolved. Also, checks were made on the space point finding effcicency and alignment of the trackers. This chapter presents the analysis of the cosmic ray test, again using the G4MICE software, including the tracker reconstruction algorithms described in the previous chapters.

## 7.2 Cosmic Ray Setup

Tracker 1 and tracker 2 are the trackers to be used in MICE, they have been constructed to the exact design described in chapter 4. For the cosmic ray test, each tracker was placed inside a black carbon fibre cylinder with an internal diameter matching that of the warm bore of the spectrometer solenoid which will be used for MICE. The patch panel was attached to the tracker cylinder via an aluminium flange and the whole tracker cylinder/patch panel set up was supported on an aluminium space frame in such a way that the principal axis of the tracker was vertical as shown

in figure 7.1. The optical readout and electronics system used for the cosmic ray test is that described in detail in section 4.4, this time using the AFEII-t readout boards as opposed to the old AFEII boards used at the KEK test.

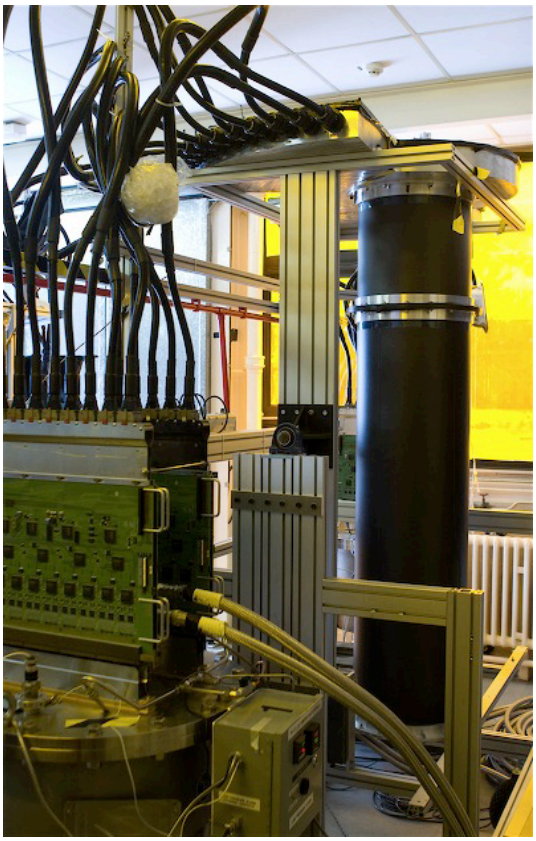

**Figure 7.1:** Cosmic-ray test stand set-up of one of the trackers at RAL, with patch panel, waveguides and optical readout system all shown.

### 7.2.1 Trigger description

Two trigger scintillators were used in the cosmic ray test stand, placed above and below the tracker cylinder. A four-inch layer of lead bricks was placed between the bottom of the tracker and the lower trigger scintillator in order to filter out any muons with kinetic energy less than $\sim$ 130 MeV. For purposes of event selection, various trigger delays were used in order to find the integration window of the Level 1 Accept trigger signal of the Trip-t chips in order to get the best performance. To achieve this, there are two time delays that need to be matched, the time it takes the light to get from the fibre to the VLPCs and the time it takes the trigger signal to be formed and sent to the AFEII-t boards as a L1A signal. The L1A signal needs

to arrive a fixed, well defined, amount of time after the light reached the VLPCs so that the charge from the VLPC that has been collected by the TRIP-t will be fully digitsed when the AFEII-t board receives the L1A signal. The overall trigger delay was estimated to be around 720 ns therefore, data were taken with various delay times around this estimate, chosen to be between 670 ns - 770 ns.

### 7.2.2 Calibration and cabling discussion

The electronics response was calibrated in the same way as at KEK (section 6.3.2), with characterisation of each individual VLPC readout channel achieved using the same LED pulser (light-injection) system. Through this process the channel-by-channel pedestal is found and clearly separated from the one photo-electron peak. Also, the one, two, three and four photo-electron peaks are found to be clearly separated from one another, allowing the gain per channel to be found. This then allows the light yield per channel to be determined using: $\text{LightYield} = \frac{[\text{ADC}-\text{pedestal}]}{\text{gain}}$, when the ADC count is below the maximum 255 counts. When a channel is found to have ADC = 255, it is considered to be a 'saturated channel' and subsequently removed from the light yield evaluation. Also, any possible clusters which may have a saturated channel are also not used.

Cabling and decoding files have again been produced such that exact mapping of electronic channel (AFE-IIt board, MCM, channel number) to physical channel (station, plane, fibre), including all interfaces inbetween, is well known with tests carried out to confirm they are correct.

## 7.3 Light Yield Performance

The performance of the MICE tracker(s) is determined mainly by the spatial measurement of the detector and the light yield produced in the detector. Therefore, a study of the final trackers light yield performance is important especially regarding the loss of light found at KEK (see chapter 6). Initial analysis of tracker 1 has already taken place elsewhere (paper to be published in coming months) and found a most probable light yield of $9.34 \pm 0.05$ PE for the full tracker 1. The tracker 1 data is analysed again here along with the new tracker 2 data. The reconstruction was performed using the G4MICE algorithms described in detail in chapter 5 with the light yield determined exactly as it was for the KEK data in section 6.7.1, using

only events that contained a reconstructed track. A cut on the reconstructed clusters of 2.5 PE is used in this analysis of tracker 1 and tracker 2, as opposed to the previous 2 PE cut used (section 5.5.1). This cut was choosen as the reconstruction process of certain events was extremely time cosuming using a 2 PE cut, probably due to particle showers, therefore a slightly safer cut of 2.5 PE was found to solve this problem whilst also not affecting the final track finding efficiency.

The tracker 1 light yield distributions obtained on a station by station basis are shown in figure 7.2, with the full tracker 1 light yield distribution shown in figure 7.3. A gaussian fit was made to the peak of the distributions to determine the most probable yield. The results are summarised in table 7.1 and show a most probable light yield of $9.52 \pm 0.02$ PE for tracker 1.

For tracker 2, the initial data taken so far has used various estimated trigger delays as described in section 7.2.1. The tracker 2 event selection was achieved by having a preminary look at the data which was taken for each of the delay times and the delays that showed the best (light yield) performance were found to be in the range of 690ns -720ns for the delay time, therefore, this is the data used for this analysis. At present the tracker 2 data has limited statistics so a station by station light yield analysis is not given, but the light yield performance of the full tracker 2 has been found and shown in figure 7.3 to produce a most probable light yield of $8.89 \pm 0.05$ PE.

## 7.4 Efficiency

To study the space point finding efficiency, tracks have been reconstructed using space points from four out of the five tracker stations, then extrapolating the track to the fifth (unused) station. If the extrapolated position was found to be within the active area of the tested station, a search was made for measured space points within a 100 mm roadwidth of the extrapolated position. For tracker 1, the space point efficiency determined for each station is given in table 7.1. Using the most probable light yield results reported for each station of tracker 1 (using a 2.5 PE cut) in section 7.3, the expected efficiencies (also given in table 7.1) are found from Poisson statistics, where the expected efficiency of the 2.5 PE cut was taken to be the median of the expected efficiencies of a 2 PE and 3 PE cut and found to be consistent with those measured. The error on the expected efficiency, for the 2.5 PE

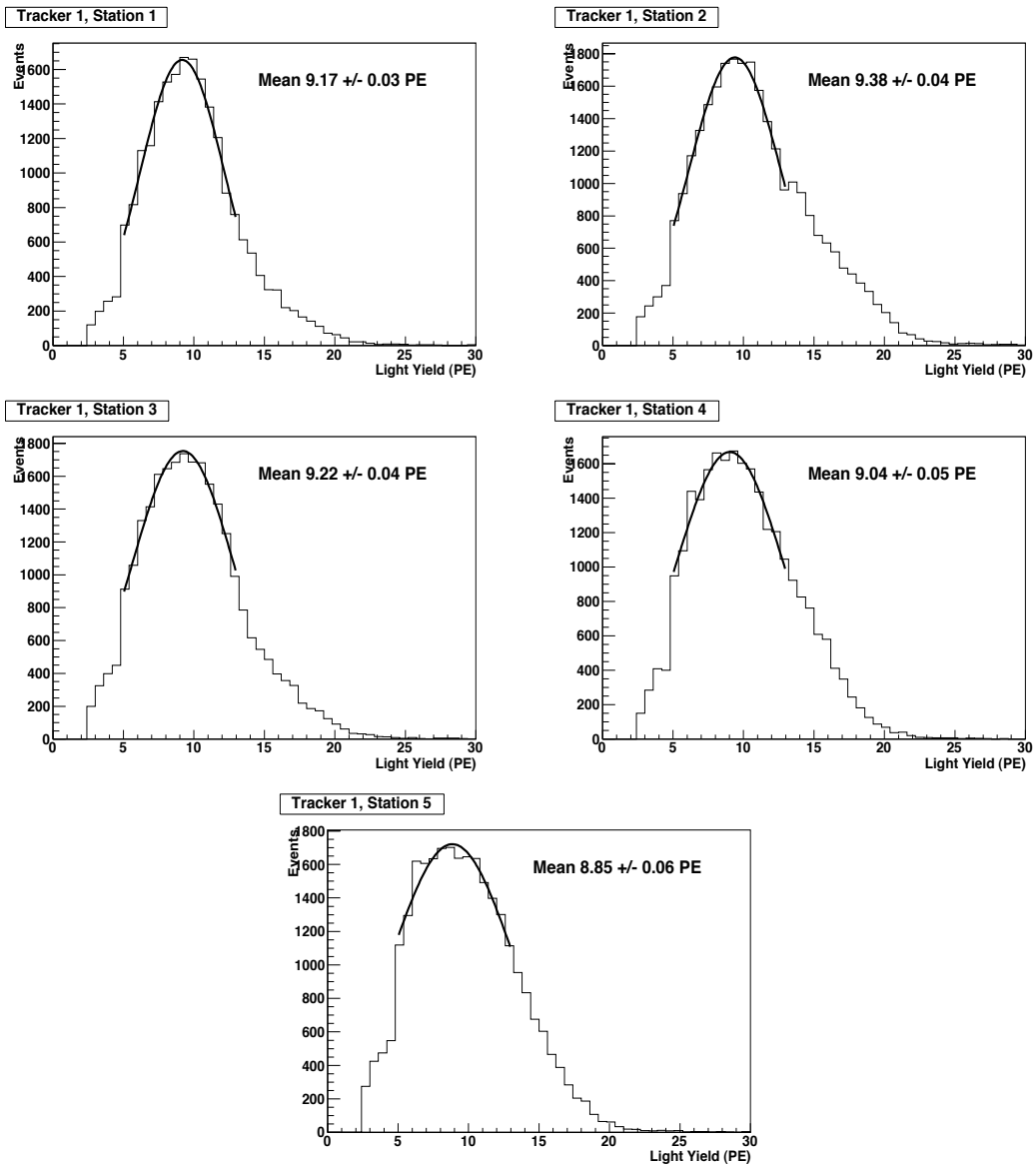


**Figure 7.2:** Light yield distributions for all stations of tracker 1.

| Station | Measured Efficiency (%) | Expected Efficiency (%) |
|---|---|---|
| 1 | $99.81 \pm 0.04$ | $99.77 \pm 0.20$ |
| 2 | $99.86 \pm 0.03$ | $99.79 \pm 0.19$ |
| 3 | $99.77 \pm 0.05$ | $99.78 \pm 0.20$ |
| 4 | $99.87 \pm 0.03$ | $99.77 \pm 0.19$ |
| 5 | $99.74 \pm 0.05$ | $99.77 \pm 0.18$ |

**Table 7.1:** Summary of space point finding efficiency per station for tracker 1 with errors (as described in the text).

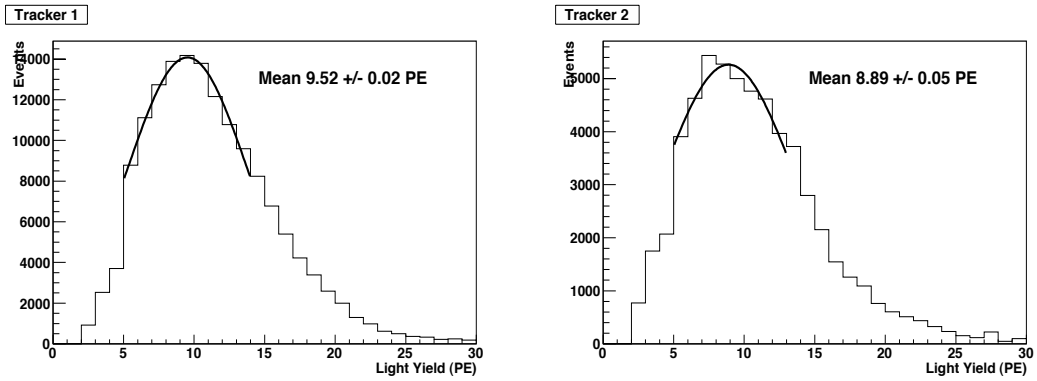


**Figure 7.3:** Light yield distributions for tracker 1 (left) and tracker 2 (right).

cut, was found by looking at the variance of the efficiencies between the 2 PE and 3 PE cuts.

As mentioned, due to limited statistics for tracker 2, an accurate measurement of the light yield on a station by station basis was not possible, therefore the space point finding efficiency study for tracker 2 is given for the tracker as a whole. The measured efficiency for the full tracker 2 is found by determining the weighted mean of the five station efficiencies measured along with their respective errors, as shown in table 7.2. As before, the expected efficiency is found on the basis of Poisson distributions using the reported most probable light yield result for tracker 2 (section 7.3), these are also given in table 7.2 and again found to be consistent with the measured result. To verify this technique, the tracker 1 efficiencies have been determined again in table 7.2 using this same method.

| Tracker | Measured Efficiency (%) | Expected Efficiency (%) |
|---|---|---|
| 1 | $99.81 \pm 0.04$ | $99.80 \pm 0.18$ |
| 2 | $99.53 \pm 0.11$ | $99.77 \pm 0.18$ |

**Table 7.2:** Summary of space point finding efficiency for tracker 1 and tracker 2 with statistical errors.

To find the track finding efficiency, from probability [81], we can say for each event the probability 'P′ of obtaining 'r′ space points $(0, 1, ...5)$ in 'n′ stations $(1, 2, ...5)$ is:

$$P = \frac{n!}{(n-r)!r!} \left(1 - p_{(point)}\right)^{n-r} p_{(point)}^{r} \tag{7.1}$$

where $p_{(point)}$ is the space point finding efficiency.

A track is made with either 5, 4 or 3 points, which gives the track finding efficiency as a function of space point efficiency to be:

$$p_{(track)} = 6p^5_{(point)} - 15p^4_{(point)} + 10p^3_{(point)} \tag{7.2}$$

therefore, using the space point finding efficiencies reported for trackers 1 and 2 in table 7.2, using equation 7.2, a track finding efficiency of $> 99.9\%$ is found for both trackers.

## 7.5 Alignment

The MICE tracker stations are constructed in such a way that the three fibre doublet-layers (views) are all aligned at 120° to one another, therefore to check the intrinsic position resolution of the fibre views we can use triplet space points. If $u$, $v$ and $w$ are the positions of the clusters in a triplet from their respective views* U, V and W, for every triplet in question, taking the origin of the $u$, $v$ and $w$ to be the centre of the respective view, it is expected that $u+v+w=0$. This means that, when plotting all triplet residuals found from cosmic rays, a measure of the intrinsic position resolution can be determined. Figure 7.4 shows the triplet residual distributions for tracker 1 and tracker 2, with the width of the distribution as expected from the station construction, confirming all three views have been aligned correctly across the full active area of each tracking station.

## 7.6 Conclusions

Analysis of the performance of tracker 1 and the preliminary results of the performance of tracker 2 using cosmic rays have been shown in this chapter, where light yield results for both trackers is found to be close to that expected. Light loss is expected at various points along the readout chain, but the significant loss of light found with station D at KEK (chapter 6) is now considered to be resolved and this effect removed from the constructed connectors that will be used for MICE. Further analysis of both trackers is currently in progress using cosmic rays, before they are both eventually installed in the MICE Hall.

*View 'U' is what was previously called view 'X' in this thesis, the re-naming of this view has been chosen such that it is not confused with the 'X'-axis of the MICE coordinate system.

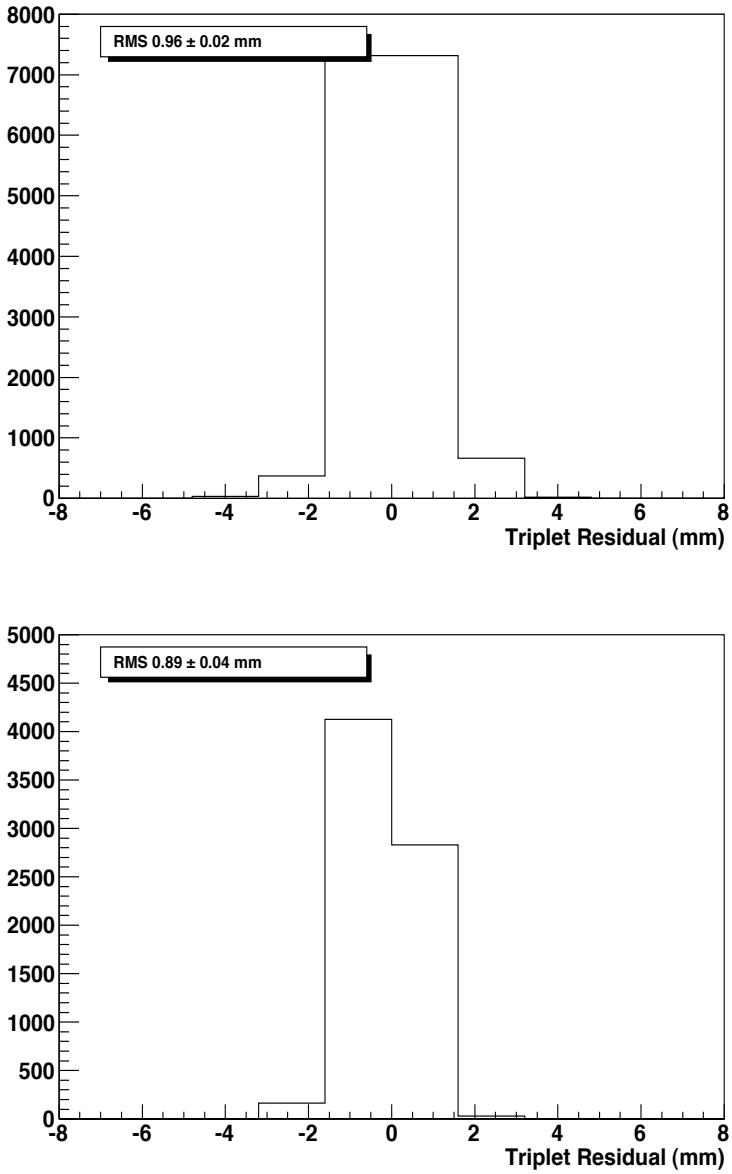


**Figure 7.4:** Triplet residual distributions for tracker 1 (left) and tracker 2 (right) using cosmic rays as described in the text.

# Chapter 8

# Summary and Conclusions

The recent discovery of neutrino oscillations and the subsequent conclusion that neutrinos have mass, indicates that the Standard Model of particle physics as we know it today, is incomplete and needs extending. This important discovery has shown how much our understanding of neutrinos, as shown in chapter 1, has evolved since Pauli first proposed the particles existence back in 1930.

To further our understanding of neutrinos and the role they play in our universe and its creation, requires unprecedented precision measurements of the oscillation parameters. This has led to the proposals of a number of new, next generation neutrino experiments. The Neutrino Factory is considered to be the best facility to achieve these goals, as it plans to produce a large neutrino flux required for precision measurements. To do this, the Neutrino Factory plans to use some untried and extremely challenging accelerator techniques, as elaborated in chapter 2.

One of these novel techniques, in the baseline design of Neutrino Factory, is muon ionisation cooling in a solenoidal focussing channel. This is required, as the muons needed for decay to produce the neutrino beam, are produced as tertiary particles, therefore they have a large beam emittance (phase space volume). Ionisation cooling, even though theoretically sound, has never been realised in practice, therefore a Proof-of-Principle experiment MICE, has been proposed to demonstrate ionisation cooling of a muon beam, through constructing a section of a Neutrino Factory cooling channel. MICE, as described in chapter 3 of this thesis, plans to make single-particle, phase space measurements before and after the cooling channel, to measure beam emittance and compare these measurements with simulation.

A magnetic spectrometer is required upstream and downstream of the cooling channel, to provide the measurements of the phase space coordinates of each particle entering and exiting the cooling channel, so an emittance measurement can be made. The tracking device chosen for MICE is a scintillating-fibre tracker. Chapter 4 of this thesis, describes the construction and development of the tracker device and its readout system, where the author played a role, as a member of the MICE tracker team.

The MICE tracker is required to measure, at given positions along the beam axis, the transverse spatial coordinates of every incident particle, which along with magnetic field information is then used to reconstruct the momentum and angles of each particle, using three or more tracking planes. The software to provide the reconstruction of the particle trajectories was discussed in chapter 5. The reconstruction algorithms from space points to fitted tracks have been described in detail, along with results showing the tracker performance and how it compares to the specification required of the tracker in order to produce the level of precision expected from MICE.

The specification requirements for the tracker, come from the ability to measure emittance with precision being highly dependent upon having a well calibrated detector system. If the systematic errors on each of the phase space measurements coming from the tracker can be kept within certain tolerances, then the bias that they introduce to the emittance measurement can be removed. For the experimental resolution not to affect the measurement of the emittance by a significant factor, the RMS resolution of the measurements must be better than about 10% of the RMS beam size at the equilibrium emittance in each of the phase space coordinates.

Through simulation of the full MICE cooling channel, a study of the tracker performance has been shown, using the new tracker reconstruction algorithms. The results have been compared to specification and also to previous results used from a tracker validation report, which used different reconstruction algorithms. The performance of the new software has shown that all transverse phase space variables can be measured well within specification, with the longitudinal momentum only just falling outside of the specification. When compared to the previous performance results, it has been shown that all measurement resolutions have improved since the tracker validation report and in the case of the transverse momentum resolution measurements, dramatic improvements have been found. The reason for this significant improvement, is due to the new reconstruction algorithms providing a more

detailed and thorough approach. It is also worth noting, that other areas of the software have changed since the tracker validation, including an improved field map description in G4MICE and also a newer version of the Kalman filtering package has been used.

The performance of the tracker is determined primarily, by the light yield and fibre pitch, therefore a number of steps have been taken during the development of the tracker. This included the construction, commissioning and successful operation of two full-scale prototypes, in order to demonstrate that the tracker can provide the reliable and efficient operation required. The second (and latter) prototype was operated and studied in a beam test at KEK, Japan. The purpose of the beam test was to analyse the operation of the device in a realistic experimental environment (as opposed to the cosmic ray test for the initial prototype) with additional upgrades. The main aims of the beam test were to investigate the light yield performance, the construction and alignment and to also demonstrate tracking in a magnetic field.

In chapter 6, a full analysis of the beam test has been described, with all aims of the experiment achieved. The G4MICE software, including the new reconstruction software described in chapter 5, was used to analyse the beam data and compare the results with simulation. A successful demonstration of tracking in a solenoidal magnetic field has been achieved as well as an investigation of the light yield performance. A significantly lower light yield was observed in the newest tracking station, which was supposed to demonstrate the construction technique to be used on the final MICE trackers. After a thorough hardware investigation, the reason behind this loss of light was found to come from issues during the construction process of a new set of connectors, required for readout of the trackers in MICE, which were only used on this particular station.

In the time since the beam test, quality assurance procedures have been developed and used for the construction of the final trackers for MICE, including the new connectors, in order to remove any errors in the construction process. The full MICE trackers, have now been constructed and have recently been studied in a cosmic ray test, with initial results showing that the light yield performance for all tracker stations, is as expected and required. The initial analysis of this recent cosmic ray test used the reconstruction software described in chapter 5, and was shown in chapter 7.

To conclude, it is useful to comment on future extensions to the work shown in this thesis. The tracker reconstruction has been shown through simulation of the full

MICE channel to provide the tracking performance required to enable the precision emittance measurements MICE aims to achieve. Previous studies, have examined the effect of the detector resolution on the emittance measurement, therefore as measurements have improved significantly since, it would be interesting to reproduce this study, with the new more detailed reconstruction. In regards to the reconstruction software, a further study of the longitudinal momentum resolution would be desirable, as possible improvements could be made, especially the estimation of the error in the longitudinal momentum passed to the track fit, which has been over simplified. Finally, further simulations of the tracker performance, using the new reconstruction, under various operational modes and beam conditions, would also be of great interest, as MICE plans to measure emittance in these different modes and conditions, in order to investigate the limits and practicality of ionisation cooling for a Neutrino Factory.

# References

[1] E. Kearns, "The emerging picture of neutrino oscillation," in *11th International Workshop on Neutrino Factories, Superbeams and Beta Beams, NuFact09*. See the web site `http://nufact09.iit.edu/`.

[2] **Super-Kamiokande** Collaboration, Y. Ashie *et al.*, "A measurement of atmospheric neutrino oscillation parameters by Super-Kamiokande I," *Phys. Rev.* **D71** (2005) 112005, `hep-ex/0501064`.

[3] O. Mena, "Unveiling Neutrino Mixing and Leptonic CP Violation," *MOD.PHYS.LETT.A* **20** (2005).

[4] M. Zisman, et al., "Neutrino factory and beta beam experiments and development," *LBNL-55478* (2004).

[5] "An international design study of a neutrino factory," 2008. See the web site `https://www.ids-nf.org/wiki/FrontPage/Documentation` for draft report (work in progress).

[6] P. Gruber, *Ionisation Cooling for a Neutrino Factory*. PhD thesis, 2001. CERN-THESIS-2001-029.

[7] **ISS Accelerator Working Group** Collaboration, J. S. Berg *et al.*, "Accelerator design concept for future neutrino facilities," *JINST* **4** (2009) P07001, `0802.4023`.

[8] R. Sandstrom, *Background and Instrumentation in MICE*. PhD thesis, University of Geneva, 2007.

[9] **MICE** Collaboration, A. Blondel, et al., "Muon Ionisation Cooling Experiment, Technical Reference Document." See the web site `http://www.mice.iit.edu/`.

[10] E. Wilson, *An introduction to Particle Accelerators*. Oxford University Press, 2001.

[11] B. Kayser, et al., "Particle Data Group," *Phys. Lett.* **B592** (2004).

[12] A. Khan, et al., "Mice scintillating-fibre tracker, first progress report," tech. rep., MICE Note 90, 2005. See: `http://mice.iit.edu/mnp/MICE0090.pdf`.

[13] W. Pauli, "Letter proposing the neutrino (1930)," *Physics Today, Letter published* (September 1978).

[14] F. Reines and C. L. Cowan, "Detection of the free neutrino," *Phys. Rev.* **92** (1953) 830–831.

[15] **LEP** Collaboration, "A combination of preliminary electroweak measurements and constraints on the Standard Model," *CERN/EP* **2001-021** (2001), no. 61,.

[16] T. D. Lee and C. N. Yang, "Question of Parity Conservation in Weak Interactions," *Phys. Rev.* **104** (1956) 254–258.

[17] C. S. Wu, E. Ambler, R. W. Hayward, D. D. Hoppes, and R. P. Hudson, "Experimental Test of Parity Conservation in Beta Decay," *Phys. Rev.* **105** (1957), no. 4, 1413–1415.

[18] L. Grodzins and A. W. Sunyar, "Evidence Concerning the Spin and Parity of $Eu152m$," *Phys. Rev. Lett.* **2** (1959), no. 7, 307–309.

[19] L. Wolfenstein, *CP violation*. NorthHolland Publishing, 1989. ISBN 0444-88081X.

[20] B. Pontecorvo, "Neutrino experiments and the question of leptonic-charge conservation," *Sov. Phys. JETP* **26** (1968) 984–988.

[21] Z. Maki, M. Nakagawa, and S. Sakata, "Remarks on the unified model of elementary particles," *Progress of Theoretical Physics* **28** (1962), no. 5, 870–880.

[22] B. T. Cleveland *et al.*, "Measurement of the solar electron neutrino flux with the homestake chlorine detector," *Astrophys. J.* **496** (1998) 505–526.

[23] **Super-Kamiokande** Collaboration, Y. Fukuda *et al.*, "Evidence for oscillation of atmospheric neutrinos," *Phys. Rev. Lett.* **81** (1998) 1562–1567, hep-ex/9807003.

[24] **SNO** Collaboration, Q. R. Ahmad *et al.*, "Measurement of the charged current interactions produced by b-8 solar neutrinos at the sudbury neutrino observatory," *Phys. Rev. Lett.* **87** (2001) 071301, nucl-ex/0106015.

[25] **KamLAND** Collaboration, T. Araki *et al.*, "Measurement of neutrino oscillation with kamland: Evidence of spectral distortion," *Phys. Rev. Lett.* **94** (2005) 081801, hep-ex/0406035.

[26] **K2K** Collaboration, M. H. Ahn *et al.*, "Measurement of neutrino oscillation by the k2k experiment," hep-ex/0606032.

[27] **MINOS** Collaboration, D. G. Michael *et al.*, "Observation of muon neutrino disappearance with the minos detectors and the numi neutrino beam," *Phys. Rev. Lett.* **97** (2006) 191801, hep-ex/0607088.

[28] Ch. Kraus, et al. *Nucl. Phys. B (Proc. Suppl.)* **118** (2003).

[29] **CHOOZ** Collaboration, M. Apollonio *et al.*, "Limits on neutrino oscillations from the chooz experiment," *Phys. Lett.* **B466** (1999) 415–430, hep-ex/9907037.

[30] **ISS Physics Working Group** Collaboration, A. Bandyopadhyay *et al.*, "Physics at a future Neutrino Factory and super-beam facility," 0710.4947.

[31] S. Geer, "Neutrino beams from muon storage rings: Characteristics and physics potential," *Phys. Rev.* **D57** (1998) 6989–6997, hep-ph/9712290.

[32] A. Blondel (Ed. ) *et al.*, "Ecfa/cern studies of a european neutrino factory complex." CERN-2004-002.

[33] D. Finley and N. Holtkamp, "A feasibility study of a neutrino source based on a muon storage ring," *Nucl. Instrum. Meth.* **A472** (2000) 388–394.

[34] S. Ozaki, R. Palmer, and M. Zisman, "2nd Feasibility Study of a Muon Storage Ring nu Factory (Invited),". Presented at IEEE Particle Accelerator Conference (PAC2001), Chicago, Illinois, 18-22 Jun 2001.

[35] **NuFactJ Group** Collaboration, "A Feasibility Study of a Neutrino Factory in Japan," 2001. See the web site `http://www-prism.kek.jp/nufactj/index.html`.

[36] **ISS Detector Working Group** Collaboration, T. Abe *et al.*, "Detectors and flux instrumentation for future neutrino facilities," *JINST* **4** (2009) T05001, `0712.4129`.

[37] A. P. Letchford, et al., "The RAL Front End Test Stand," in *Proceedings of EPAC 2006*, pp. 303–305.

[38] K. T. McDonald, H. G. Kirk, H. Haseroth, J. R. J. Bennett, L. Bruno, C. J. Densham, P. V. Drumm, T. R. Edgecock, A. Fabich, T. A. Gabriel, J. R. Haines, Y. Hayato, S. J. Kahn, J. Lettry, H. Ludewig, C. L, R. B. Palmer, Y. Prykarpatskyy, R. V. Samulyak, N. Simos, P. Thieberger, and K. Yoshimura, "Studies of a target system for a 4-mw, 24-gev proton beam," Tech. Rep. INTC-P-186. CERN-INTC-2004-016, CERN, Geneva, 2004. revised version submitted on 2004-04-27 15:47:43.

[39] Roger Bennett, et al., "A neutrino factory target station design based on solid targets." Third High-Power Target Workshop, Bad Zurzach, Switzerland, September 10-14, 2007.

[40] R. C. Fernow, "Muon front end for the neutrino factory," *Nucl. Phys. B (Proc. Suppl.)* **155** (2006) 74–78.

[41] A. Bogacz and V. Lebedev, "Recirculating linac muon acceleration for neutrino factory," *NIM A* **503** (2003) 306–308.

[42] E. Keil and A. Sessler, "Muon acceleration in ffag rings," *NIM A* **538** (2005) 159–177.

[43] M. Aiba, et al., "Development of a FFAG proton synchrotron," in *Proceedings of EPAC 2000*, pp. 581–583. 2000.

[44] R. Edgecock, et al., "EMMA - The World's First Non-Scaling FFAG," in *Proceedings of EPAC08*, pp. 3380–3382. 2008.

[45] **The $\mu^+$ $\mu^-$ Collider** Collaboration, "$\mu^+$ $\mu^-$ collider: A feasibility study," 1997. LBNL-38946.

[46] **The Muon Collider and Neutrino Factory** Collaboration. See the web site `http://www.cap.bnl.gov/mumu/` which contains references.

[47] **MICE** Collaboration, "Muon Ionisation Cooling Experiment Proposal," 2003. See the web site `http://mice.iit.edu/mnp/MICE0021.pdf`.

[48] S. Y. Lee, *Accelerator Physics*. World Scientific, 2004.

[49] M. Conte and W. W. MacKay, *An Introduction to the Physics of Particle Accelerators*. World Scientific, 1991.

[50] C. Rogers, *Beam Dynamics in an Ionisation Cooling Channel*. PhD thesis, University of London, 2008.

[51] H. Wiedemann, *Particle Accelerator Physics I: Basic Principles and Linear Beam Dynamics*. Springer-Verlag, 1999.

[52] H. Goldstein, *Classical Mechanics*. Addison Wesley, 2001.

[53] G. Penn and J. S. Wurtele, "Beam envelope equations for cooling of muons in solenoid fields," *Phys. Rev. Lett.* **85** (Jul, 2000) 764–767.

[54] D. Neuffer, "Principles and applications of muon cooling." Fermilab note, FN-378, 1983.

[55] C. Rogers and M. Ellis, "High precision measurement of muon beam emittance reduction in MICE," in *Particle Accelerator Conference (PAC05), Knoxville, Tennessee*. 2005.

[56] **Kloe** Collaboration, "The kloe detector technical proposal," 1992.

[57] M. Ellis, "MICE Software Design and Physics Performance, 11th ICATPP Conference, Villa Olmo, Como," 2009.

[58] **GEANT4** Collaboration, S. Agostinelli *et al.*, "GEANT4: A simulation toolkit," *Nucl. Instrum. Meth.* **A506** (2003) 250–303.

[59] T. Roberts et al., "G4beamline (ongoing development)." See the web site `http://www.muonsinc.com/tiki-index.php?page=G4beamline`.

[60] R. C. Fernow, "ICOOL: A simulation code for ionization cooling of muon beams, Proc. PAC1999, 3020," 1999.

[61] **D0** Collaboration, V. M. Abazov *et al.*, "The Upgraded D0 Detector," *Nucl. Instrum. Meth.* **A565** (2006) 463–537, physics/0507191.

[62] A. Bross, E. Flattum, D. Lincoln, S. Grnendahl, J. Warchol, M. Wayne, and P. Padley, "Characterization and performance of visible light photon counters (vlpcs) for the upgraded d detector at the fermilab tevatron," *Nuclear Instruments and Methods in Physics Research Section A: Accelerators, Spectrometers, Detectors and Associated Equipment* **477** (2002), no. 1-3, 172 – 178.

[63] R. C. Ruchti, "The use of scintillating fibers for charged-particle tracking," *Annual Review of Nuclear and Particle Science* **46** (1996), no. 1, 281–319, http://arjournals.annualreviews.org/doi/pdf/10.1146/annurev.nucl.46.1.281.

[64] The MICE Tracker Group, "Specification of the scintillating and clear fibre for the mice scintillating fibre trackers," (2006) http://mice.iit.edu/micenotes/public/pdf/MICE0135/MICE0135.pdf.

[65] T. R. Sashalmi, "Station spacing study," http://mice.iit.edu/micenotes/public/pdf/MICE0191/MICE0191.pdf.

[66] P. Rubinov, *AFEIIt Readout Format*, November 2007. DØ Note 5520.

[67] T. Hart, "MICE Tracker Data Acquisition Using DØ Analog Front End IIt Boards," (2007) http://mice.iit.edu/micenotes/public/doc/MICE0139/MICE0139.doc.

[68] A. Lombodenko, *MIL-1553B control and monitor*, July 2001. DØ Note 3886.

[69] S. Rapisarda, et al., *VME LVDS SERDES Buffer (VLSB) Module Specification*, February 2005. ESE-D0-041101.

[70] A. Cervera-Villanueva, J. J. Gomez-Cadenas, and J. A. Hernando, "'recpack' a reconstruction toolkit," *Nucl. Instrum. Meth.* **A534** (2004) 180–183.

[71] R. Mankel, "Pattern recognition and event reconstruction in particle physics experiments," *Reports on Progress in Physics* **67** (2004), no. 4, 553–622.

[72] R. K. Bock, et. al., *Data Analysis Techniques for High-Energy Physics*. Cambridge University Press, second edition ed., 2000.

[73] E. W. Weisstein, "Circle. From MathWorld–A Wolfram Web Resource.." See the web site http://mathworld.wolfram.com/Circle.html.

[74] D. Pedoe, *Circles: A Mathematical View*. The Mathematical Association of America, second edition ed., 1997.

[75] E. W. Weisstein, "Quadratic Curve. From MathWorld–A Wolfram Web Resource.." See the web site `http://mathworld.wolfram.com/QuadraticCurve.html`.

[76] R. Fruhwirth, "Application of Kalman filtering to track and vertex fitting," *Nucl. Instrum. Meth.* **A262** (1987) 444–450.

[77] **CERNLIB** Collaboration, "PAW, Physics Analysis Workstation." See the web site `http://wwwasd.web.cern.ch/wwwasd/paw/`.

[78] R. Barlow, *Statistics: a guide to the use of statistical methods in the physical sciences*. J. Wiley, 1993. ISBN: 0471922951.

[79] A. Horikoshi, "Report of tof and acc performance." MICE Collaboration Meeting 13, 2005.

[80] G. Barber, "Tracker Mechanical, presentation at MICE collaboration meeting 14, Osaka."

[81] K. A. Stroud, *Engineering Mathematics*. Macmillan Press LTD., 1995. ISBN 0-333-62022-4.